

Thesis for the Degree of
Doctor

Production of the proton and light fragments
in ${}^{96}_{44}\text{Ru}+{}^{96}_{44}\text{Ru}$ collisions at SIS18 energies
and
the multigap Resistive Plate Chamber

by

Min Sang Ryu

Department of Physics

Graduate School
Korea University

June 2009



洪炳軾 教授指導
博士學位論文

Production of the proton and light fragments
in Ru+Ru collisions at SIS18 energies
and
the multigap Resistive Plate chamber

論文 理學 博士學位 論文 提出

2009年 6月 5日

高麗大學校 大學院

物理學科

柳 珉 相 (印)





柳珉相의 理學 博士學位論文
審査를 完了함.

2009年 6月 5日

委員長 홍 병식 (印)

委員 이 경세 (印)

委員 원 은안 (印)

委員 박 인규 (印)

委員 최 선호 (印)





Abstract

The formation of the hydrogen (p , d , and ${}^3\text{H}$) and helium isotopes (${}^3\text{He}$ and ${}^4\text{He}$) in ${}^{96}_{44}\text{Ru}+{}^{96}_{44}\text{Ru}$ collisions at 0.4 and 1.528 AGeV has been studied. For the most central collisions, the rapidity distributions and the production yields of the proton and light fragments were calculated from fitting the invariant spectra by the simple thermal blast model formula, and the radial flow velocity and the temperature were extracted at the mid-rapidity. In addition, for the central, semicentral, and peripheral collisions, the differential elliptic flow, v_2 , as a function of transverse momentum, p_t , of the proton and light fragments were analyzed. The scaled differential elliptic flow of light fragments, v_2/n , where n is the number of composite nucleons, as a function of the scaled transverse momentum, p_t/n , were compared to that of proton in each collision centrality. The observed scaling phenomenon of the elliptic flow for light fragments may imply the nucleon coalescence scenario in heavy-ion collisions at SIS18 energies.

As the second part of this thesis, we have designed and built prototype multigap timing resistive plate chambers which consist of four gaps, made of normal glass plates and a strip readout plane. The characteristics of the chambers have been investigated in avalanche-mode operation with the mixed gases consisting of $\text{C}_2\text{F}_4\text{H}_2$, $i\text{-C}_4\text{H}_{10}$, and SF_6 , by using cosmic ray muons. The efficiency is larger than 90 % and the time resolution is less than 95 ps in the operational high-voltage plateau region, which extends at least 400 V. The fraction of the non-Gaussian tail in the time spectra is about 2 %, which satisfies the required performance of the time-of-flight measurement. The results demonstrate that the current design of the chambers can be utilized for the charged particle identification in collision experiments.





Contents

1	Part I : Introduction	3
1.1	Nuclear matter	3
1.2	Collective flow	7
1.3	Nucleon coalescence model	10
1.3.1	Coalescence parameter B_A	10
1.3.2	Scaled differential elliptic flow	12
2	Part I : FOPI detector and the experimental condition	13
2.1	S183 experiment	16
2.2	FOPI detector	18
2.2.1	Start systems	19
2.2.2	Magnet	19
2.2.3	Central Drift Chamber (CDC)	19
2.2.4	Helitron	22
2.2.5	Barrel	22
2.2.6	Plastic Wall (PLAWA)	23
2.2.7	Zero-Degree Counter (ZDC)	24
3	Part I : Analysis	25



3.1	Event selection	25
3.1.1	Double beam interaction	25
3.1.2	Non-target event	27
3.2	Collision centrality	27
3.3	Track selection	31
3.3.1	$d0_{free}$ and $z0_{free}$ of CDC	31
3.3.2	Matching conditions between CDC and Barrel	32
3.3.3	Matching conditions between Helitron and PLAWA	34
3.4	Charge selection	34
3.5	Particle identification (PID)	37
3.6	Efficiency correction	43
3.6.1	Matching efficiency between Helitron and PLAWA	43
3.6.2	Matching efficiency between CDC and Barrel	49
3.6.3	CDC track efficiency	53
3.7	Phase space distribution	57
3.8	Reaction plane reconstruction	60
4	Part I : Results and Discussions	65
4.1	Kinematic distributions of the proton and light fragments	65
4.1.1	Invariant spectra	65
4.1.2	Rapidity spectra	71
4.1.3	Radial flow velocity and temperature	71
4.1.4	Systematic errors	74
4.2	Differential elliptic flow	78
4.3	Nucleon coalescence parameters	82
4.3.1	Coalescence coefficient B_A	82
4.3.2	Scaled differential elliptic flow	86



5	Part I : Conclusions	90
6	Part II : Introduction	95
7	Part II : Detector Configuration	100
7.1	Design and construction	100
7.2	Front-end-electronics (FEE)	101
8	Part II : Experimental setup	105
8.1	Efficiency measurement	105
8.2	Time resolution measurement	106
9	Part II : Experimental Results	109
9.1	Efficiency	109
9.2	Time resolution without correction	110
9.3	Time resolution with slewing correction	113
10	Part II : Conclusions	120



List of Figures

1.1	Phase diagram of the nuclear matter in temperature and baryon chemical potential	5
1.2	Equation-of-state of the nuclear matter with the compressibility parameter $\kappa = 380$ MeV (stiff) and $\kappa = 200$ MeV (soft)	6
1.3	Schematic diagram of in-plane bounce-off and out-of-plane squeeze-out with respect to the reaction plane	8
1.4	Sideward (v_1) and elliptic (v_2) flows of nucleons and pions in Au+Au collisions as a function of beam energy	9
1.5	Double differential cross section of light fragments as a function of the particle energy in a laboratory frame in Ne+U at 0.25 and 0.4 AGeV	11
2.1	Schematic figure of the accelerator facilities and the experimental areas at the GSI	14
2.2	Details of the SIS	15
2.3	Experimental setup for the S183 experiment	17
2.4	FOPI detector with indication of sub-detectors	18
3.1	Deposited energy and arrival time distributions of the start counter in Ru+Ru collisions at 1.528 AGeV	26
3.2	Primary vertex distributions in Ru+Ru collisions at 1.528 AGeV	28
3.3	Total multiplicity distributions of the charged particles in Ru+Ru collisions at 0.4 and 1.528 AGeV	29



3.4	Deviation between tracks and primary event vertex as a function of momentum in Ru+Ru collisions at 0.4 and 1.528 AGeV	33
3.5	Matching condition between the extrapolated CDC tracks and the Barrel hits in Ru+Ru collisions at 0.4 and 1.528 AGeV	35
3.6	Matching condition between the extrapolated Helitron tracks and the PLAWA hits in Ru+Ru collisions at 0.4 and 1.528 AGeV	36
3.7	Correlation between the energy loss of the drift chamber and the velocity measured by the scintillation detectors in Ru+Ru collisions at 0.4 and 1.528 AGeV	38
3.8	Charge distribution of the Barrel and PLAWA in Ru+Ru collisions at 0.4 and 1.528 AGeV	39
3.9	Correlation between the charge and mass of Helitron in Ru+Ru collisions at 0.4 and 1.528 AGeV	40
3.10	Correlation between the charge and mass in Ru+Ru collisions at 0.4 and 1.528 AGeV	41
3.11	Correlation between the momentum of the Helitron and the velocity of PLAWA in Ru+Ru collisions at 0.4 and 1.528 AGeV	44
3.12	Correlation between the mass and momentum of the Helitron in Ru+Ru collisions at 0.4 and 1.528 AGeV	45
3.13	Correlation between the momentum of the CDC and the velocity of Barrel in Ru+Ru collisions at 0.4 and 1.528 AGeV	46
3.14	Correlation between the mass of the Barrel and the momentum of the CDC in Ru+Ru collisions at 0.4 and 1.528 AGeV	47
3.15	Energy loss and the mass as a function of the momentum of the CDC in Ru+Ru at 0.4 and 1.528 AGeV	48
3.16	Matching efficiencies between the Helitron and the PLAWA in Ru+Ru collisions at 0.4 AGeV	50
3.17	Background estimation by using the mass distribution of the Helitron in Ru+Ru collisions at 1.528 AGeV	51
3.18	Matching efficiencies between the Helitron and PLAWA in Ru+Ru collisions at 1.528 AGeV	52



3.19	Matching efficiency between the CDC and Barrel in Ru+Ru collisions at 0.4 (left) and 1.528 (right) AGeV	54
3.20	CDC track efficiencies as a function of p_t calculated by the IQMD simulation in Ru+Ru collisions at 0.4 AGeV	55
3.21	CDC track efficiencies as a function of p_t calculated by the IQMD simulation in Ru+Ru collisions at 1.528 AGeV	56
3.22	Phase-space distributions of the hydrogen isotope in Ru+Ru collisions at 0.4 and 1.528 AGeV	58
3.23	Phase-space distributions of the helium isotope in Ru+Ru collisions at 0.4 and 1.528 AGeV	59
3.24	Azimuthal angle distributions and the resolution of the reaction plane in Ru+Ru collisions at 0.4 and 1.528 AGeV	62
3.25	Correction factors by using Ollitrault's correction method . . .	63
4.1	Invariant spectra of the hydrogen isotopes in Ru+Ru collisions at 0.4 AGeV	67
4.2	Invariant spectra of the helium isotopes in Ru+Ru collisions at 0.4 AGeV	68
4.3	Invariant spectra of the hydrogen isotopes in Ru+Ru collisions at 1.528 AGeV	69
4.4	Invariant spectra of the helium isotope in Ru+Ru collisions at 1.528 AGeV	70
4.5	Rapidity distributions of the hydrogen and helium isotopes for the most central Ru+Ru collisions at 0.4 and 1.528 AGeV . .	72
4.6	Mean kinetic energies of the light fragments for the most central Ru+Ru collisions at 1.528 AGeV	75
4.7	Mean kinetic energies of the light fragments as a function of the particle mass at the mid-rapidity for the most central Ru+Ru collisions at 0.4 and 1.528 AGeV	76
4.8	Comparison of the temperature and the mean radial flow velocity as function of the beam energy	77



4.9	Differential v_2 distributions of the light fragments as a function of p_t in comparison with that of the protons in central Ru+Ru collisions at 0.4 and 1.528 AGeV.	79
4.10	Differential v_2 distributions of the light fragments as a function of p_t in comparison with that of the protons in semicentral Ru+Ru collisions at 0.4 and 1.528 AGeV.	80
4.11	Differential v_2 distributions of the light fragments as a function of p_t in comparison with that of the protons in peripheral Ru+Ru collisions at 0.4 and 1.528 AGeV.	81
4.12	Invariant spectra of the light fragments in Ru+Ru collisions at 0.4 AGeV	83
4.13	Invariant spectra of the light fragments for most central Ru+Ru collisions at 1.528 AGeV	84
4.14	Coalescence parameter B_A estimated by the coalescence model for most central Ru+Ru collisions at 0.4 and 1.528 AGeV . . .	85
4.15	Scaled differential elliptic flow distribution of the light fragments for central Ru+Ru collisions at 0.4 and 1.528 AGeV . .	87
4.16	Scaled differential elliptic flow distribution of the light fragments for semicentral Ru+Ru collisions at 0.4 and 1.528 AGeV	88
4.17	Scaled differential elliptic flow distribution of the light fragments for peripheral Ru+Ru collisions at 0.4 and 1.528 AGeV	89
6.1	Schematic diagram of the upgraded FOPI detector with new time-of-flight system	96
6.2	Operational principle of the single gap RPC	98
6.3	Operational process of the multigap RPC	98
6.4	Correlation between the time and the charge of the induced signals	99
7.1	Schematic plane view of a multigap RPC with its dimensions .	102
7.2	Schematic side view of a multigap RPC with its dimensions .	102



7.3	Picture of the FEE	103
7.4	Test input pulse and the amplified pulse from the FEE	104
7.5	Raw signal from the multigap RPC and the amplified signal with the gain of 100 via the FEE	104
8.1	Schematic diagram of the experimental setup for the efficiency measurement	106
8.2	Schematic diagram of the DAQ system for the efficiency measurement	107
8.3	Schematic diagram of the experimental setup for the time resolution measurement	108
8.4	Schematic diagram of the DAQ system for the time resolution measurement	108
9.1	Efficiency of two multigap RPCs measured with cosmic ray muons as a function of the applied high voltage	111
9.2	Raw charge distributions at both ends of strips of the multigap RPCs at 6.4 kV.	112
9.3	Raw time distributions at both ends of strips of the multigap RPCs at 6.4 kV.	114
9.4	Raw spectra for the time difference between two multigap RPCs at 6.4 kV.	115
9.5	Slewing correction by using the correlation between the average time and charge for each RPCs.	117
9.6	Time difference spectrum between two RPCs at 6.4 kV after the slewing correction	118
9.7	Time resolution and tail fraction of the multigap RPC measured with cosmic ray muons	119



List of Tables

3.1	Centrality selections for the central events in the TMUL distributions	30
3.2	Centrality selection for the flow	31
3.3	Polar angle acceptance of sub-detectors	32
3.4	Correction factors of the Fourier coefficients (v_n) for each centrality selection	64
4.1	Total production yields of the particles for the most central Ru+Ru collisions at 0.4 and 1.528 AGeV	73
9.1	Fit parameters for the slewing correction.	116





PART I

Production of the proton and light fragments
in Ru+Ru collisions at 0.4 and 1.528 AGeV





Chapter 1

Part I : Introduction

In the ongoing relativistic heavy-ion collision experiments, the properties of hot and dense nuclear matter depending on the temperature and density are being investigated [1, 2, 3]. The experimental observables are the particle production, the kinematic properties of the various hadrons, and the collective flow [4, 5].

1.1 Nuclear matter

Figure 1.1 shows the nuclear phase diagram as functions of the temperature (T) and the baryonic chemical potential (μ_B), which is lowest energy state of the particle in a system. Figure 1.1 displays the freeze-out points determined by several heavy-ion experiments [6]. The chemical freeze-out is defined the state when the inelastic collisions stop and the relative particle ratios and yields are fixed. The thermal freeze-out is defined the state when the elastic collisions stop and the transverse momentum spectra do not change any longer.

For relatively low μ_B and high temperature region, the phase transition from the hadron gas to the quark-gluon-plasma (QGP) [1, 7] has been searched



by using the relativistic heavy ion collider (RHIC) at the Brookhaven National Laboratory (BNL) in the USA [8] and to be searched at the Large Hadron Collider (LHC) at the European Organization for Nuclear Research (CERN) in Switzerland [9]. The QGP is the new form of the matter state consisting of the deconfined quarks and gluons, predicted by the quantum chromodynamics (QCD) [10]. The QCD is responsible for the strong interaction among hadrons and partons.

On the other hand, for the relatively low temperature and high baryon density, the properties of nuclear matter has been studied by using the heavy-ion synchrotron (Schwerionensynchrotron:SIS) at Gesellschaft für Schwerionenforschung (GSI). The SIS can accelerate various nuclei up to 2 GeV per nucleon (A GeV). The typical timescale of the collision at SIS energies is about $5 \sim 10$ fm/c which is consistent with approximately 2×10^{-23} s. The temperature of 100 MeV corresponds to 1.2×10^{12} K. The FOPI collaboration has been studied the strangeness production for the in-medium effect at near or sub-threshold energy [11, 12, 13, 14], the nuclear stopping power which is the degree of energy loss of the particles in the fireball [15, 16, 17], and the collective flow of the particles [18, 19, 20, 21].

The equilibrated nuclear matter produced in heavy-ion collisions can be characterized by nuclear equation-of-state (EOS), which relates the energy with the compressibility [2]. The EOS can be obtained by analyzing the kinematic distribution and collective flow of various particles. The total energy in the center of mass is composed of the compressional (E_c), the thermal (E_{th}), and the ground state (E_0) energies [22]:

$$E(\rho, T) = E_c(\rho, T = 0) + E_{th}(\rho, T) + E_0. \quad (1.1)$$

where ρ is the nuclear matter density. The excited hot and dense nuclear matter has a bigger compression pressure, represented as the compressibility (κ), defined as the following relation [23]:

$$\kappa = 9\rho_0^2 \frac{d^2}{d\rho^2} \left(\frac{E}{A} \right). \quad (1.2)$$

A stiff EOS with $\kappa = 380$ MeV and a soft EOS with $\kappa = 200$ MeV are commonly used as shown in figure 1.2 [24].



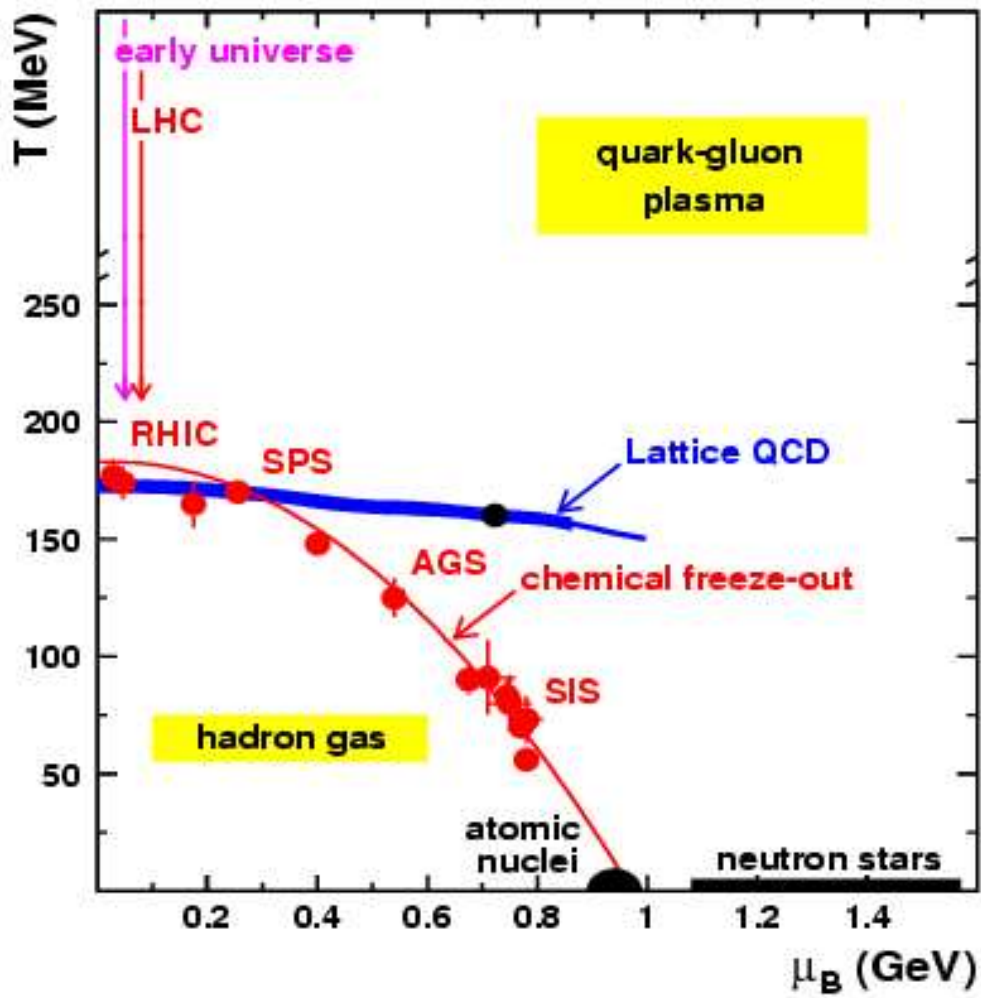


Figure 1.1: Phase diagram of the nuclear matter in temperature and baryon chemical potential [3, 6].



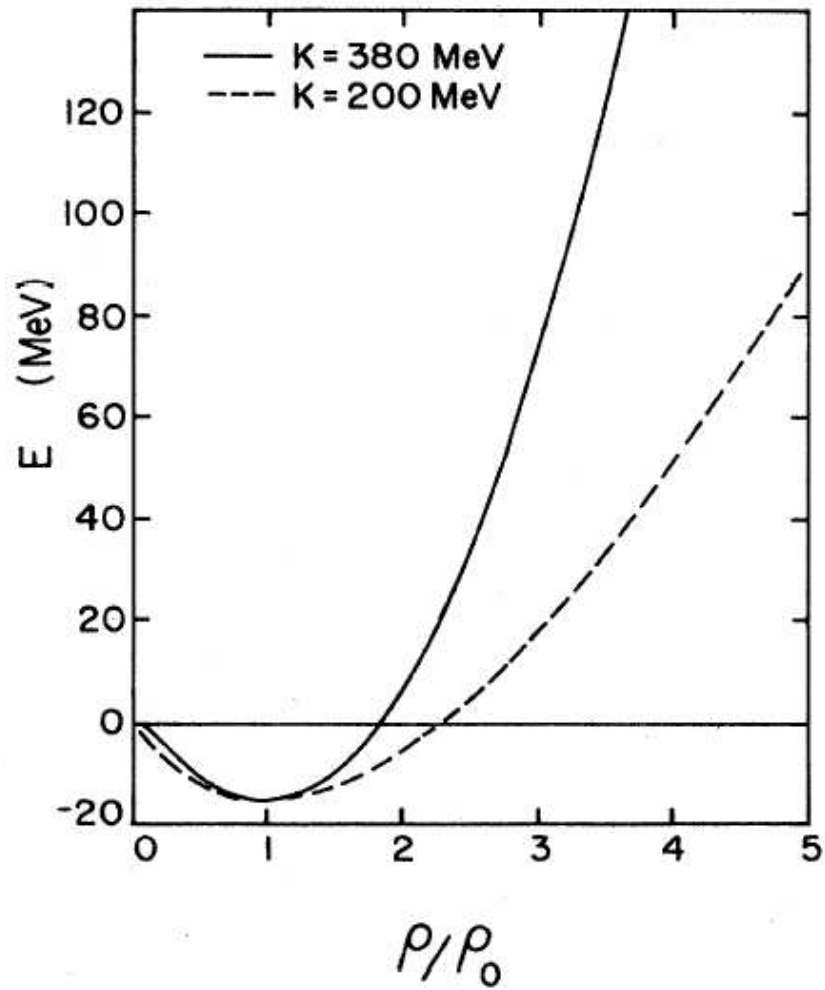


Figure 1.2: Equation-of-state of the nuclear matter with the compressibility parameter $\kappa = 380$ MeV (stiff) and $\kappa = 200$ MeV (soft) [24]. The nuclear matter density in the ground state (ρ_0) is $\sim 0.17 \text{ fm}^{-3}$.



1.2 Collective flow

The collective behaviour of compressed nuclear matter in heavy-ion collisions is depicted in figure 1.3 [25, 26, 27]. The azimuthal distribution of the particles can be studied with respect to the reaction plane which is defined by the impact parameter and beam direction. The in-plane particle emission in forward direction, so called directed or sideward flow, can occur when the spectator is deflected by the participant matter. There are also in- and out-of-plane particle emissions at mid-rapidity, so called elliptic flow, and, specially, the out-of-plane emission is called the squeeze-out. The elliptic flow can take place by the pressure gradients within the expanding nuclear matter.

For the collective flow, the normalized azimuthal distribution can be fitted as follow:

$$\frac{dN}{d\phi} = \frac{1}{2\pi} \left(1 + \sum_{n=1}^{\infty} 2v_n \cos(n\phi) \right) \quad (1.3)$$

where $v_n = \langle \cos(n\phi) \rangle$ is the n -th Fourier coefficient. The anisotropical emission of particles can be characterized by the coefficients, v_n . The v_1 and v_2 describe the sideward and elliptic flows of expanding source, respectively:

$$\begin{aligned} v_1 &= \langle \cos \phi \rangle = \left\langle \frac{p_x}{p_t} \right\rangle \\ v_2 &= \langle \cos 2\phi \rangle = \left\langle \frac{p_x^2 - p_y^2}{p_x^2 + p_y^2} \right\rangle \end{aligned} \quad (1.4)$$

Systematic analysis has shown that the elliptic as well as the directed flows are maximum at a beam energy around 0.4 AGeV, and varies weakly between 0.25 and 0.8 AGeV in Au+Au collisions as shown in figure 1.4 [26]. For $\langle \cos \phi \rangle$, flowing and anti-flowing are represented by positive and negative slopes, respectively, as a function of the rapidity. For $\langle \cos 2\phi \rangle$, negative value implies the squeeze-out and positive value implies the in-plane elliptic flow with respect to the reaction plane.



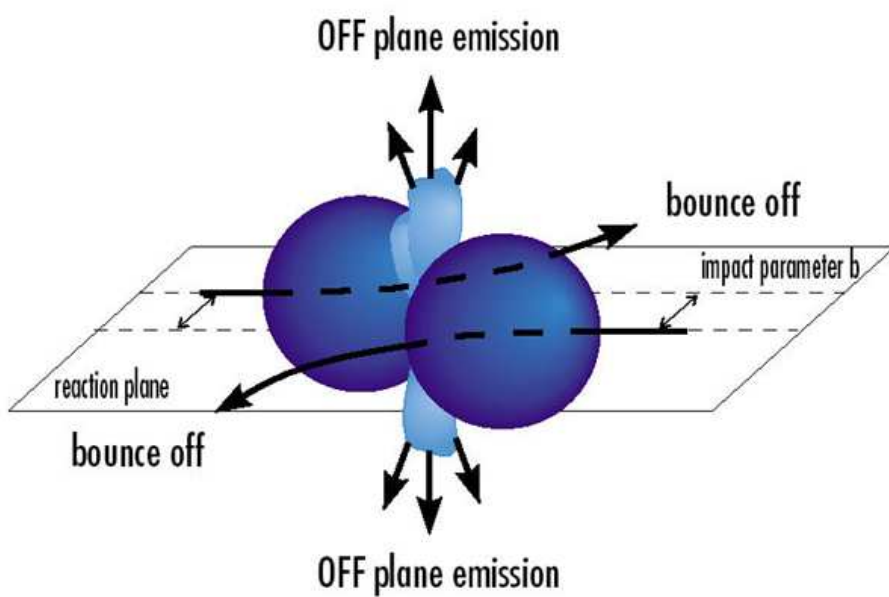


Figure 1.3: Schematic diagram of in-plane bounce-off and out-of-plane squeeze-out with respect to the reaction plane, defined by the impact parameter and beam direction [2].



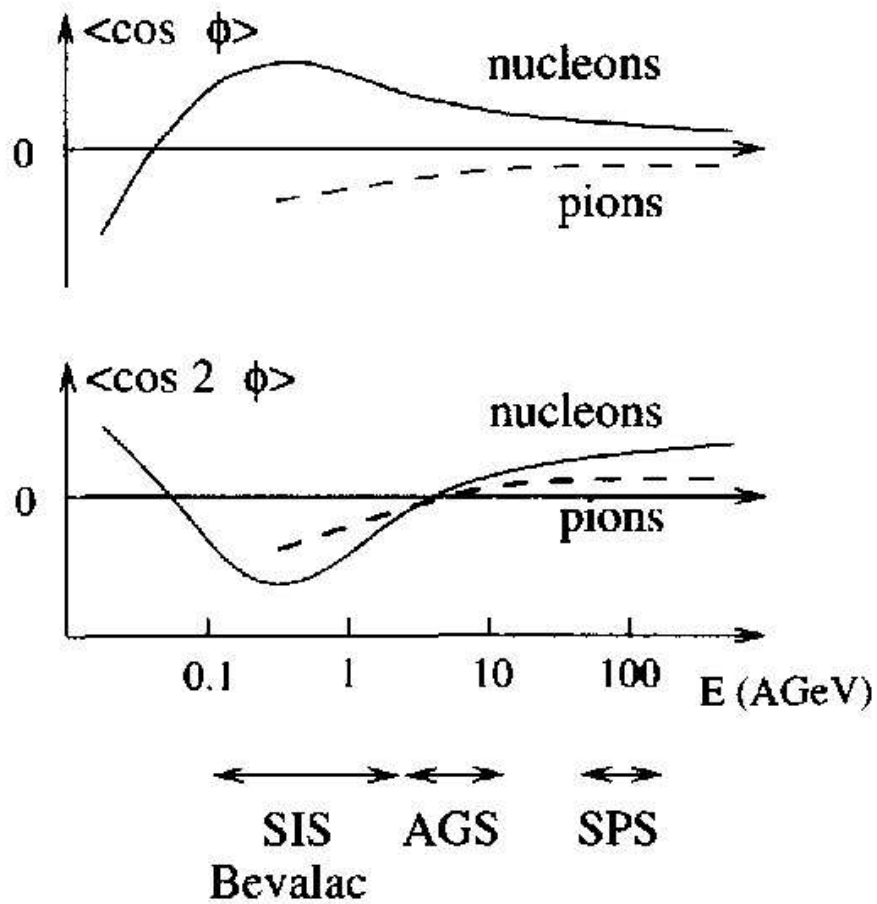


Figure 1.4: Sideward (v_1) and elliptic (v_2) flows of nucleons and pions in Au+Au collisions as a function of beam energy. Maximum elliptic flow is expected at a beam energy around 0.4 AGeV [26].



1.3 Nucleon coalescence model

To describe the yields and momentum spectra of light fragments produced in heavy-ion collisions, the nucleon coalescence model was invented. The basic idea is that any two nucleons, whose relative momentum are within a certain momentum, p_0 , of each other, coalesce to form a deuteron, and that any three nucleons within another p_0 form a triton, etc. Historically, Butler and Pearson developed the model for deuterons in 1960's [28, 29]. Successively, Schwartzschild, Zupancic, and Gosset *et al.* developed the model for the formation of ^3H , ^3He , and ^4He by using a simplified phenomenological extensions of the Butler-Pearson model [30]. Later Schwartzschild and Zupancic extended the model to composite particles from nucleon-nucleus collisions [31], and Gosset *et al.* formulated their phenomenological model for nucleus-nucleus collisions [32].

1.3.1 Coalescence parameter B_A

The cluster formation can be characterized by the invariant coalescence factor (B_A) from the invariant nucleon and cluster momentum spectra via the equation

$$E_A \frac{d^3 N_A}{dp_A^3} = B_A \left[\left(E_p \frac{d^3 N_p}{dp_p^3} \right)^Z \left(E_n \frac{d^3 N_n}{dp_n^3} \right)^N \right]_{p_p=p_n=p_A/A} \quad (1.5)$$

where $p_A = Ap_p$ is the momentum of the cluster and $A = Z + N$ is the mass number of the cluster. Z and N are the numbers of proton and neutron, respectively, and p_p and p_n are the momenta of proton and neutron, respectively [33]. In figure 1.5, the double differential cross sections of light fragments are shown as a function of the particle energy in a laboratory frame from the irradiation of uranium by ^{20}Ne ions at 0.25 (bottom) and 0.4 (top) AGeV [34]. The solid lines are the calculations by the coalescence model.



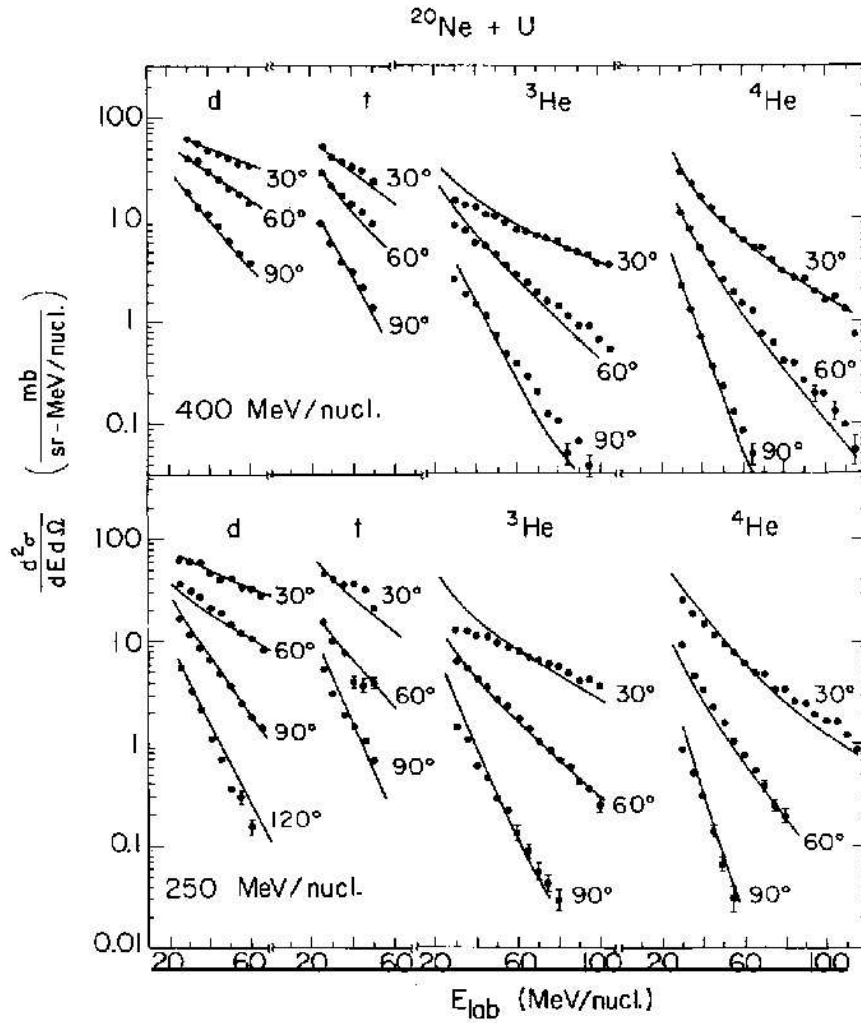


Figure 1.5: Double differential cross section of light fragments as a function of the particle energy in a laboratory frame in $^{20}\text{Ne}+\text{U}$ at 0.25 (bottom) and 0.4 (top) AGeV [34]. The solid lines are the calculations by the coalescence model.



1.3.2 Scaled differential elliptic flow

The collective flow can be used to test the nuclear coalescence scenario in heavy-ion collisions. If the production of the light fragments (d , ${}^3\text{H}$, ${}^3\text{He}$ and ${}^4\text{He}$) are produced by the coalescence mechanism in a collision, the scaled differential elliptic flow, v_2/n , where n is the number of composite nucleons, as a function of the scaled transverse momentum, p_t/n , would agree with the differential v_2 distribution of protons.



Chapter 2

Part I : FOPI detector and the experimental condition

The FOPI detector has been used for a fixed-target heavy-ion experiment at the 'Schwerionensynchrotron' (SIS) of the 'Gesellschaft für Schwerionenforschung' (GSI) in Darmstadt, Germany. The SIS can accelerate various heavy-ion beams from 0.1 to 2.0 GeV per nucleon in order to study the properties of hot and dense nuclear matter. Schematic figure of the accelerator facilities and experimental areas are shown in figure 2.1, and the details of the SIS are shown in figure 2.2. In the synchrotron the available kinetic energy of heavy ion beam can be obtained by the following formula :

$$\frac{E_{beam}}{A} = m_p c^2 \left(\sqrt{1 + \left(\frac{B\rho c Q}{m_p c^2 A} \right)^2} - 1 \right) \quad (2.1)$$

where A and Q are the mass number and charge, respectively, of the beam, m_p is the mass of proton, c is the speed of light, and $B\rho$ is the magnetic rigidity of the synchrotron. The maximum rigidity of the SIS is 18.7 Tm.

The FOPI detector covers nearly full solid angle (4π) by the sub-detector systems which consist of the two drift chambers and scintillation detectors [11]. It is able to detect charged particle, i.e. light mesons (π^\pm ,



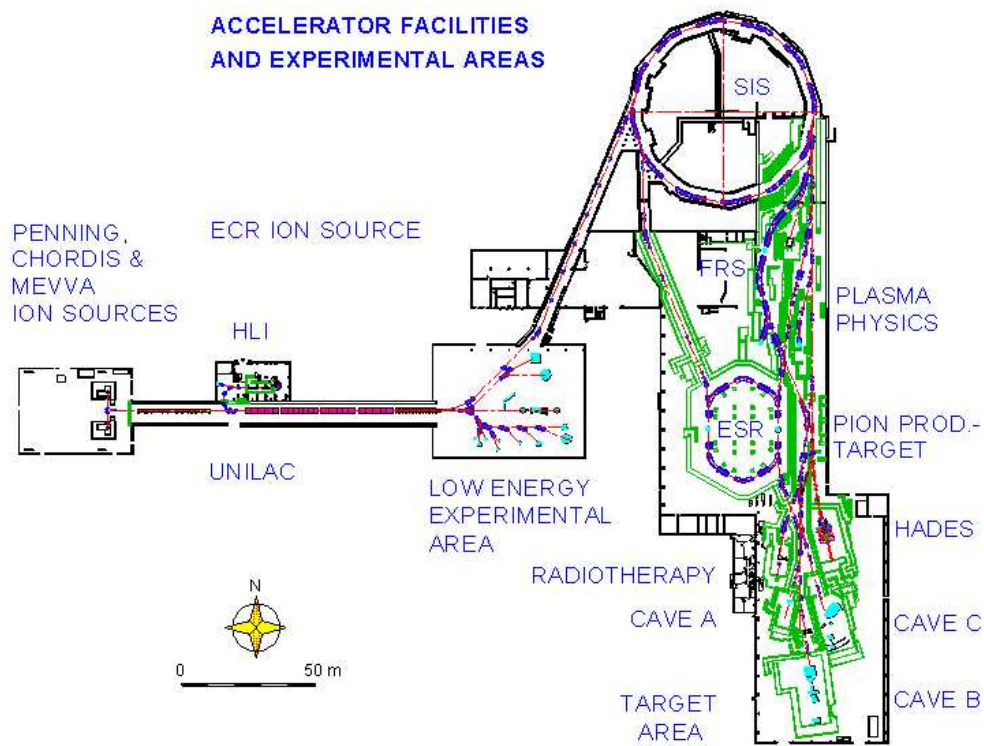


Figure 2.1: Schematic figure of the accelerator facilities and the experimental areas at the GSI: The FOPI detector is located in the cave B.



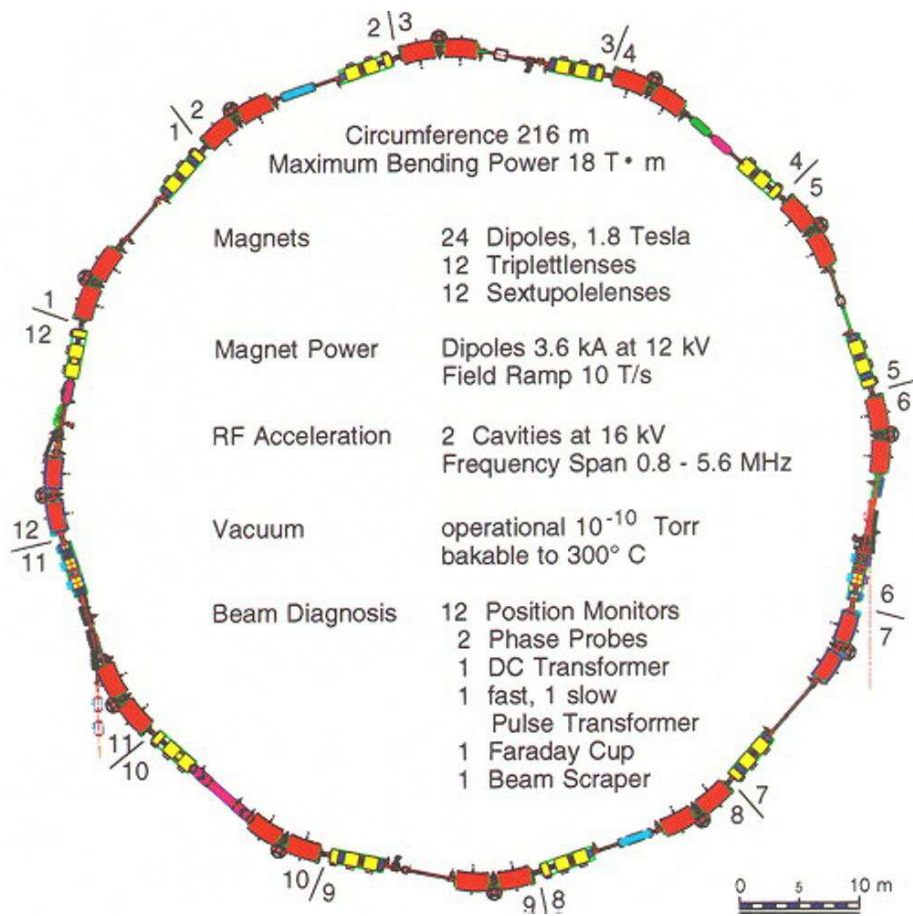


Figure 2.2: Details of the SIS



K^\pm), hydrogen (p , d , ^3H) and helium isotopes (^3He and ^4He), and heavier fragments. The following subsections describe the FOPI detector and the experimental setup for the S183 experiment.

2.1 S183 experiment

The S183 experiment had been performed with the FOPI detector at SIS/GSI in 1996. Figure 2.3 shows the outline of the experimental setup with its dimensions. We used two stable isobaric nuclei ($^{96}_{44}\text{Ru}$ and $^{96}_{40}\text{Zr}$), which have the largest ratio between neutron and proton numbers (N/Z) in the Periodic Table for relatively large masses. The major goals of the S183 experiment were

- Production and flow of the strangeness particles at near or sub-threshold beam energies
- N/Z equilibration: a degree-of-mixing among projectile and target nucleons

The $^{96}_{44}\text{Ru}$ target of 431 mg/cm^2 was supported in a very thin 10 mm diameter aluminum ring. It contained 96.52 % $A=96$ species in isotope abundances. The $^{96}_{40}\text{Zr}$ target of 507 mg/cm^2 , with Zr component of 380 mg/cm^2 , contained 95.6 % $A=96$ in isotope abundances. The diameter of the targets were 10 mm and they positioned between two Kapton foils of 3.65 mg/cm^2 each.

The interaction probability (p_{int}) between the beam and the target can be calculated by the following formula

$$p_{int} = \rho l_z \frac{N_A}{A} \sigma_{tot}^{geo} = \rho l_z \frac{N_A}{A} \left(\sqrt[3]{A_p} + \sqrt[3]{A_t} \right) r_0, \quad (2.2)$$

where ρ and A are the density and mass, respectively, of the target material, l_z is the target thickness ($\sim 100 \mu\text{m}$), N_A is the Avogadro constant. Here, σ_{tot}^{geo} is the total geometrical cross section for a reaction between projectile and target nucleus. The both targets were designed to have 1 % interaction probability in a given minimum beam intensity and a given thickness of the target.



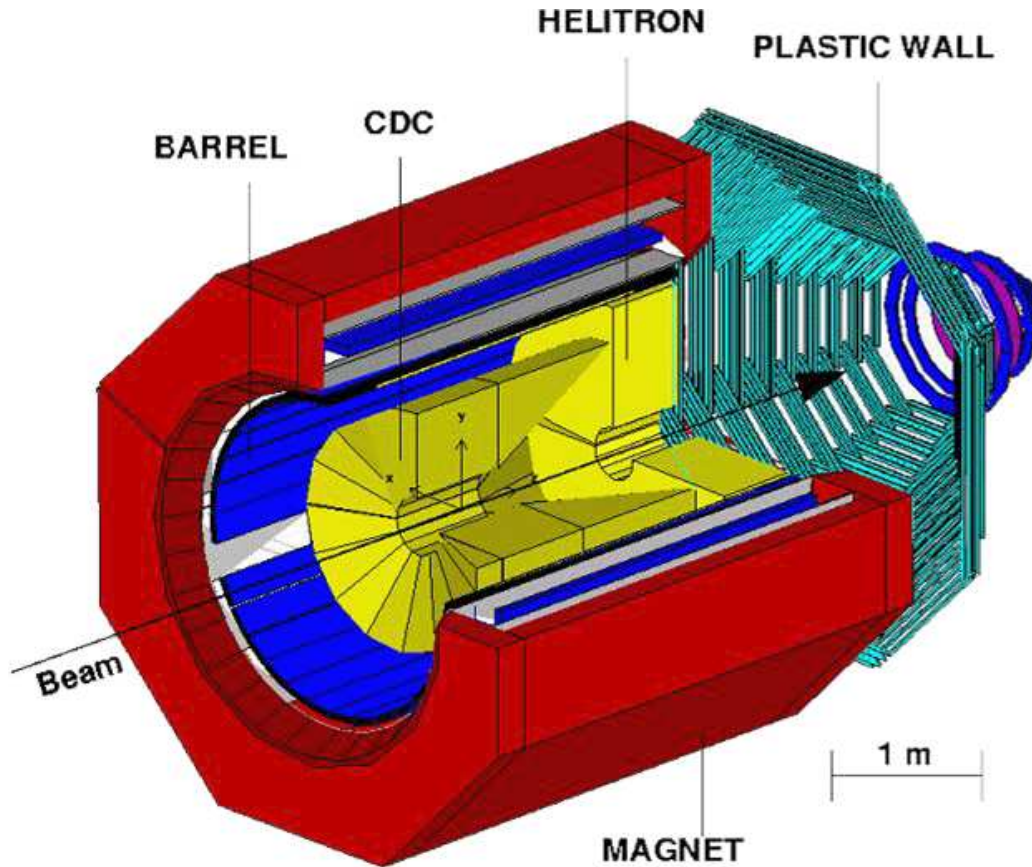


Figure 2.4: FOPI detector with indication of sub-detectors.

2.2 FOPI detector

The sub-detectors of FOPI consist of two drift chambers, which are Central Drift Chamber and Helitron, and the plastic scintillation detectors named Plastic Wall and Barrel [35]. A schematic view of the detector is shown in figure 2.4. The characteristics and the performances of sub-detectors are presented in the following subsections.



2.2.1 Start systems

The start system consists of the start detector, which is used to count incoming ions and provides the reference time t_0 for all sub-detectors, and two veto detectors, dubbed as Halo1 and Halo2, which deliver the veto signal for badly focussed beam particles. The start (S) and two veto detectors (H1 and H2) are shown in figure 2.3. The start detector located at 2.5 m upstream of the target consists of a thin scintillator plate, tilted by 45° from the vertical axis. The signal is read out by two photomultiplier tubes (PMTs) [36]. The time resolution of the start detector is ~ 50 ps. Halo1 is placed right upstream of the start detector and Halo2 is located at 10 cm upstream of the target. Halo1 and Halo2 have a cylindrical hole in the middle in order to define the size of the beam. The anti-coincidence veto system with the start detector can reject the beams, which are not focused on the target.

2.2.2 Magnet

The superconducting magnet, whose dimensions are 3.3 m in length and 2.4 m in diameter, produces a homogeneous solenoidal magnetic field of 0.6 T parallel to the beam axis. The CDC, Helitron, and Barrel are placed inside the magnet as shown in figure 2.4. The transverse and total momenta of the charged particles can be measured from the curvature in the xy plane and the polar angle θ due to their helical motion under the solenoidal magnetic field.

2.2.3 Central Drift Chamber (CDC)

The CDC is the main tracking system of the FOPI detector. It has a cylindrical geometry with conical end caps at the front and back side. The length in the beam axis is 2 m, and the inner and outer radii are 0.2 and 0.8 m, respectively, from the target. It has the full azimuthal coverage and the polar



acceptance covered from 33° to 145° . The CDC consists of 16 sub-sectors in azimuth, and each sub-sector consists of 60 sense and 61 potential wires parallel to the beam axis. The sense wires are $30\text{-}\mu\text{m}$ -thick W-Rh (20%) with a resistance of $500\ \Omega/\text{m}$. The lengths of the sense wires vary between 86 and 190 cm depending on the radial coordinate [11]. The mixed gas, composed of 88% Ar, 10% Isobutane, and 2% CH_4 , flows at the atmospheric pressure. The drift voltage of -15 kV and potential voltage of -1.63 kV, which form homogeneous and high electric fields, are applied.

When the charged particles pass through the CDC gas volume, the ionized electrons drift toward the sense wires where the signals are collected. The drift velocity of electrons is about $45\ \mu\text{m}/\text{ns}$, which is compatible with the longest dead time, which is $\sim 5\ \mu\text{s}$. The hit position on the wire is reconstructed by the method of the charge division [37, 38]. The position resolutions of the hit are estimated as $300\ \mu\text{m}$ in the xy plane and as 10 cm in the z -axis. In order to reduce the mirror track effect, the planes of sense and potential wires are tilted by 8° and the sense wires are staggered by $\pm 100\ \mu\text{m}$ in the planes. The trajectory of charged particle is curved by the homogeneous magnetic field of 0.6 T along the beam axis. The CDC is able to identify the particle species and to measure the momentum of the particle from its trajectory and the specific energy loss of the particle by the following Bethe-Bloch relation [36, 39]:

$$-\frac{dE}{dx} = Kz^2 \frac{Z}{A} \frac{1}{\beta^2} \left[\frac{1}{2} \ln \left(\frac{2m_e c^2 \beta^2 \gamma^2 T_{max}}{I^2} \right) - \beta^2 - \frac{\delta(\beta\gamma)}{2} \right] \quad (2.3)$$

where E : energy of incident particle ($\gamma M c^2$)

z : charge number of incident particle

Z and A : Atomic number and mass of the absorber

K/A ($4\pi N_A r_e^2 m_e c^2 / A$) = $0.3071\ \text{MeVg}^{-1}\text{cm}^2$ for $A = 1\ \text{g mol}^{-1}$

N_a : Avogadro's number = $6.022 \times 10^{23}\ \text{mol}^{-1}$

r_e : classical electron radius ($e^2/4\pi\epsilon_0 m_e c^2 = 2.817\ \text{fm}$)

m_e : electron mass ($0.511\ \text{MeV}/c^2$)

$\beta = v/c$ ($\beta_{max} = 1$)

v : speed of incident particle

c : speed of light ($2.99792458 \times 10^8\ \text{m/s}$)

$\gamma = 1/\sqrt{1 - \beta^2}$



T_{max} : maximum kinetic energy imparted to a free electron in a single collision

$$T_{max} = \frac{2m_e c^2 \beta^2 \gamma^2}{1 + 2\gamma m_e/M + (m_e/M)^2} \text{ with the incident particle of mass } (M)$$

$$T_{max} = 2m_e c^2 \beta^2 \gamma^2 \text{ for } M \gg 2\gamma m_e \text{ due to the low-energy approximation [40]}$$

I : mean excitation energy

$\delta(\beta\gamma/2)$: density effect correction to the ionization energy loss

We can calculate the transverse and total momenta without the charge separation by the following equations

$$\frac{p_t}{z} = e \cdot r \cdot B \quad (2.4)$$

$$p/z = \frac{p_t/z}{\sin(\theta)} \quad (2.5)$$

where $e = 0.3 \text{ T}^{-1}\text{m}^{-1}$, is the elementary charge, z is charge number of incident particle, B is magnetic field in tesla, and r is track radius of incident particle in meter in the xy plane.

The tracking code starts to look into the window of small track density in the xy plane, which is usually the outer circumference of the CDC. Three hits are selected, and they define a circle reaching the origin for the fixed target $(x, y) = (0, 0)$. Successively the tracker softwares keep checking whether there are related hits in the defined circle and refitting the circle with new hits up to the inner radius of the CDC. Finally, the circle becomes the reconstructed track for the charged particle.

The primary vertex of the event can be determined by using the interpolation method from the reconstructed track to the target position. But the interpolated points of all tracks have some allowance for the target position due to the finite resolution of the detector ($\sigma_{xy} = 300 \mu\text{m}$, $\sigma_z = 10 \text{ cm}$). Especially, the polar angle of the particle can be distorted by the position resolution in the z -axis. It can be corrected by means of *refit* procedure which forces the reconstructed vertex position to the origin [37]. The uncorrected events and tracks are called *freefit*.

The energy loss resolution, $\sigma(dE/dx)/(dE/dx)$, as a function of dE/dx



in the CDC is estimated between 15 and 25%. The transverse momentum resolution, $\sigma(p_t)/p_t$, which is calculated from Iso-spin Quantum Molecular Dynamics(IQMD) simulations by using an event generator and the GEANT package [41], rises from 4% for $p_t < 0.5$ GeV/ c to about 12% for $p_t = 2$ GeV/ c [42].

The IQMD model is based on the QMD, considering that the isospin degrees of freedom enter into the cross sections and also the Coulomb interactions. The QMD model is the n -body theory which simulates heavy-ion reactions at intermediate energies on an event-by-event basis. In many cases, the QMD model can describe the non-equilibrium feature of the heavy-ion collisions as the constituents can explicitly interact with each other [23, 22].

2.2.4 Helitron

The Helitron is the drift chamber for tracking of the charged particles in the forward region. It covers the full azimuthal angle, and the polar angle from 7° to 30° in the laboratory frame. It consists of 24 sectors in azimuth, and each sector contains 54 potential and 53 sense wires, which run along radially. The potential wires are made of $125\text{-}\mu\text{m}$ -diameter CuBe, and the sense wires are $50\text{-}\mu\text{m}$ -diameter NiCr with $1\text{ k}\Omega/\text{m}$ resistivity [11, 37]. The Helitron is operated with the same gas mixture as the CDC. The track reconstruction method of the particle is also similar to that of the CDC [38, 43].

2.2.5 Barrel

The Barrel consists of 180 plastic scintillators, whose dimensions is $240 \times 4 \times 3\text{ cm}^3$. They are located at a radius of 111 cm from the beam axis and parallel to the beam axis. It covers about 75 % of full azimuthal angle in the polar angle coverage from 39° to 130° [44]. The PMTs are connected at both ends of each scintillator, and the measured signals provide the time-of-flight (t_{ToF}) and hit position (z) on the z -axis as the following relation:



$$t_{ToF} = \frac{t_L + t_R}{2} - \frac{L}{2v_{\gamma_{propa}}} \quad (2.6)$$

$$z = \frac{t_L - t_R}{2} v_{\gamma_{propa}}, \quad (2.7)$$

where t_L and t_R denote the arrival times of the signal at both ends of the scintillator, L (=240 cm) is the length of scintillator, and $v_{\gamma_{propa}}$ (~ 16 cm/ns) denotes the propagation velocity of the light in the scintillator. The time and position resolutions of the Barrel are ~ 300 ps and ~ 8 cm, respectively. The azimuthal angle resolution is 2° limited by the dimensions of the scintillator. The velocity of the particle can be calculated from t_{ToF} and z by the following relation:

$$v = \frac{s}{t_{ToF}} = \frac{\left[2\rho \sin^{-1}\left(\frac{R_B}{2\rho}\right) / \sin(\theta_{lab}) \right]}{t_{ToF}}, \quad (2.8)$$

where s is the flight path of the particle, ρ is the curvature radius of particle trajectory, θ_{lab} is the emission polar angle, and R_B (=111 cm) is the distance from the beam axis to the scintillators [45]. The geometrical matching between the tracks of the CDC and the hits in the Barrel is required in order to improve the particle identification with certain matching conditions.

2.2.6 Plastic Wall (PLAWA)

The PLAWA consists of 512 scintillator strips which are grouped into 8 radial sectors made of 64 strips. It covers a full azimuthal angle, and polar angle from 7° to 30° in the laboratory frame. Each strip has a rectangular area of 1.8×2.4 cm² and each strip is read out by PMTs at both ends. Two energy signals (E_L , E_R) and measured energy loss (ΔE) are related by the following relation:

$$\Delta E \propto \sqrt{E_L E_R}. \quad (2.9)$$



Two time signals (t_L, t_R) and time-of-flight (t_{ToF}) are connected by the equation 2.6. The hit position x is connected to t_L and t_R by the equation 2.7 or the following relation:

$$x \propto \ln(E_L/E_R) \quad (2.10)$$

The velocity also can be calculated by the equation 2.8. The active scintillator lengths are different from 45 cm at $\theta_{lab}=7^\circ$ to 165 cm at $\theta_{lab}=30^\circ$, and time resolution σ_{ToF} varies between 80 and 120 ps, which correspond to 1.2 and 2 cm, respectively, of position resolution. The PLAWA gives fast information of the charged particle multiplicity in an event, thus it is suited for the online trigger. The present isospin experiment had three specific event triggers at the hardware levels [46]. *Minimum bias* is triggered for $PMUL \geq 1$, *Medium bias* for $\sim 50\%$ of the *Minimum bias* rate, and *Central bias* for $\sim 10\%$ of the *Minimum bias* rate.

2.2.7 Zero-Degree Counter (ZDC)

The ZDC is made of 252 trapezoidal shape scintillator paddles which are arranged in seven concentric rings, and it has the polar angle coverage from 1° to 7° in the laboratory frame. The ZDC measures the time-of-flight (t_{ToF}) by equation 2.6, the velocity (v) by equation 2.8, and the energy loss (ΔE) by equation 2.9.



Chapter 3

Part I : Analysis

In this chapter, the event selection, the collision centrality determination, the track quality assurance, the charge separation, and the particle identification will be presented. For the backward region, the matching efficiency between the CDC and the Barrel has been obtained. And we have calculated the matching efficiency between the Helitron and the PLAWA for the forward region. The CDC track efficiency has been determined by the simulation result of the IQMD model.

3.1 Event selection

The major sources of the experimental background events are the double beam interactions and the non-target events for the beam to collide with the material other than the target.

3.1.1 Double beam interaction

The double beam interaction events can not be distinguished in a certain time interval. The sub-detectors of the FOPI have different dead times



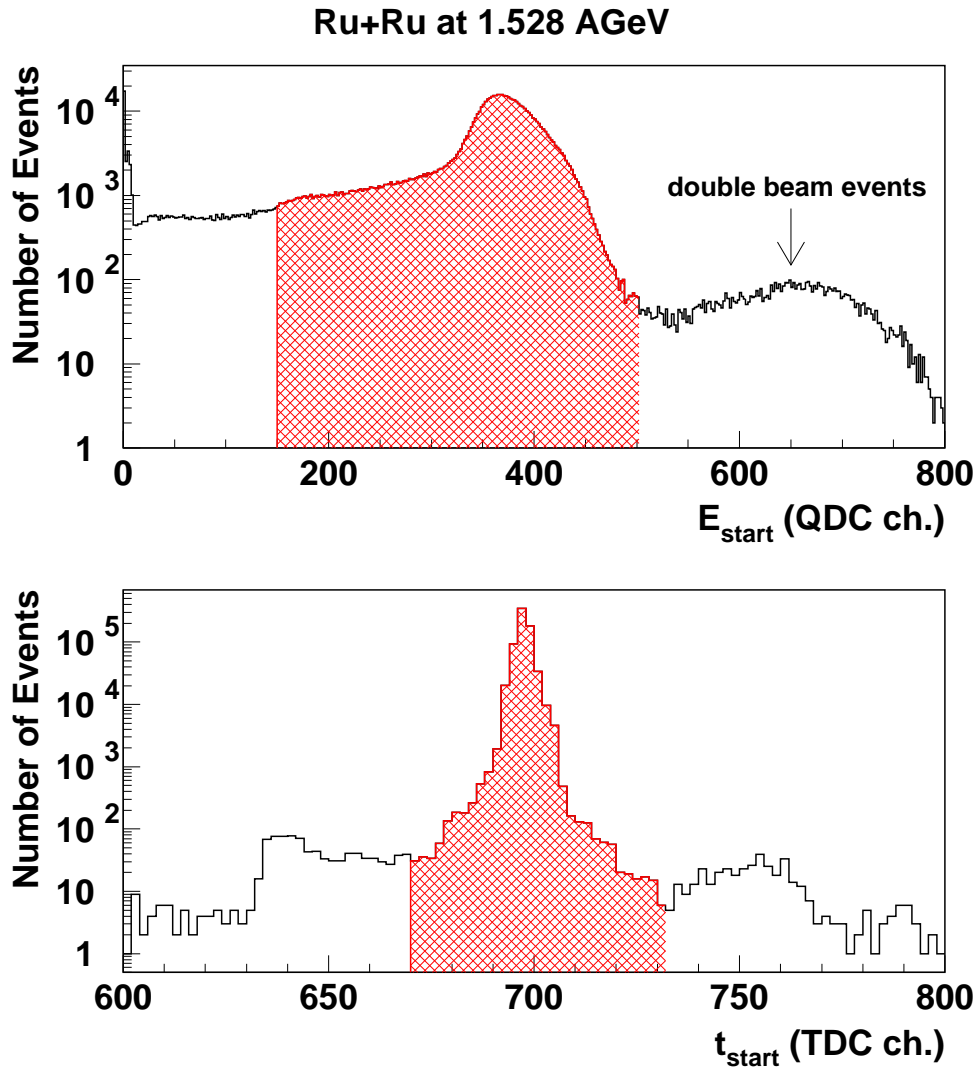


Figure 3.1: Deposited energy (top) and arrival time (bottom) distributions of the start counter in Ru+Ru collisions at 1.528 AGeV. The shaded areas represent the selection criteria of good interaction events.



due to the reponse time of the scintillation counters and the drift velocity of the drift chambers. Unless the time interval between two incoming ions is larger than 100 ns they can not be separated by the trigger system [37, 45]. The deposited energy and the arrival time distributions of the start counter are used shown in figure 3.1. The measured energy loss due to double beam interaction events is expected to be about double of the single event, and it results in two peak structure. Therefore, we regard the peak near 400 channels in the energy deposit distribution in figure 3.1 as good events.

3.1.2 Non-target event

The non-target upstream events are not fully rejected by the halo detectors and the trigger system. The beam can interact with not only the target but also the start counter, beam pipe, the exit window of the vacuum pipe in the beam line, and other air molecules near beam path, etc. In figure 3.2, the cut has been applied to the reconstructed primary vertex distributions with a certain tolerance taking into account for the target size (10 mm diameter and 100 μm thickness) and the detector performance (300 μm position resolution in the xy plane and 10 cm position resolution in the z -axis). The discontinuous distribution of z_{vertex} at ± 20 cm is due to the *refit* procedure, forcing the event vertex at the target position. The vertices in $|z_{vertex}| \leq 20$ cm are refitted as shown in figure 3.2.

3.2 Collision centrality

The total multiplicity of the charged particle is used to identify the collision centrality of the collisions. The particle multiplicity in the central collisions is expected to be higher than that in the peripheral collisions [47]. The total multiplicity distributions of the charged particles in Ru+Ru collisions at 0.4 and 1.528 AGeV are shown in figure 3.3. In this analysis, the total multiplicity (TMUL) is defined by the sum of the multiplicities measured by



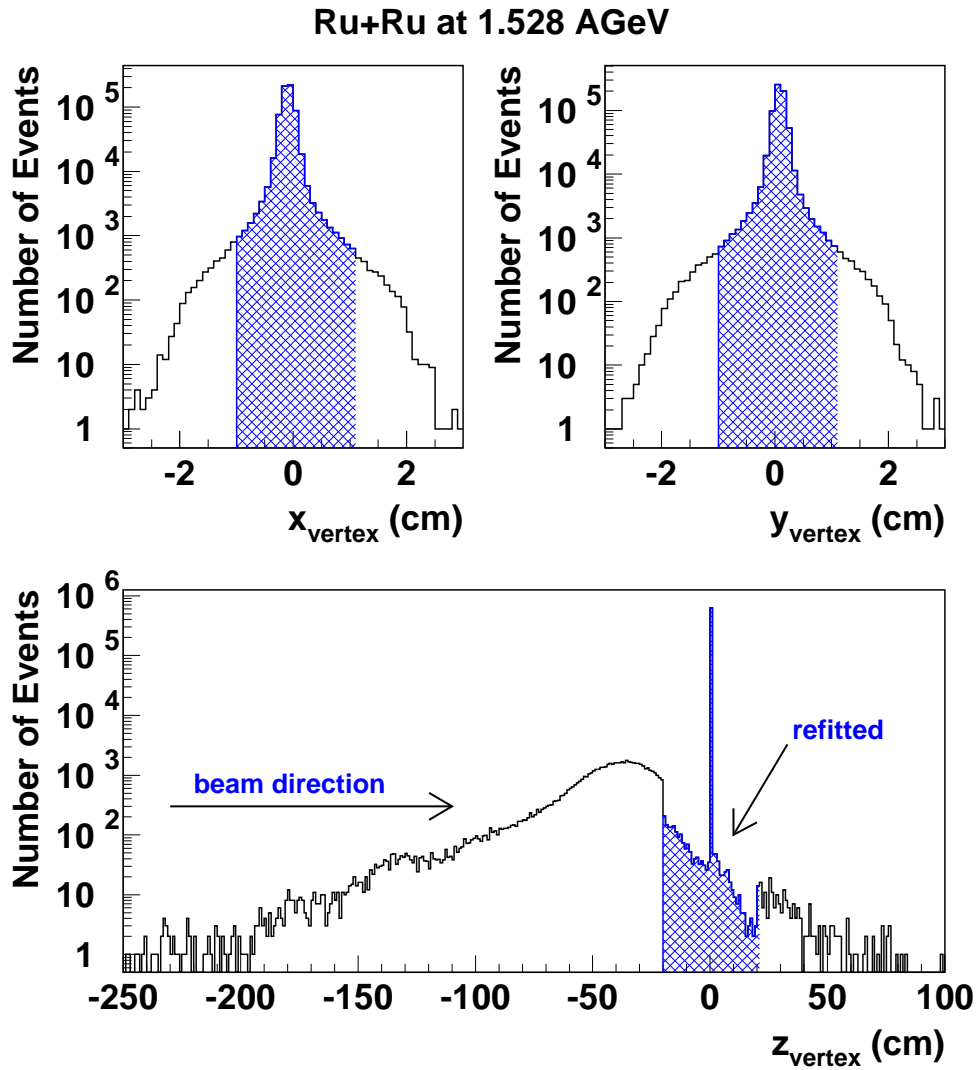


Figure 3.2: Primary vertex distributions in Ru+Ru collisions at 1.528 AGeV: x_{vertex} (top left) and y_{vertex} (top right) are in the xy plane and z_{vertex} (bottom) is along the beam axis.



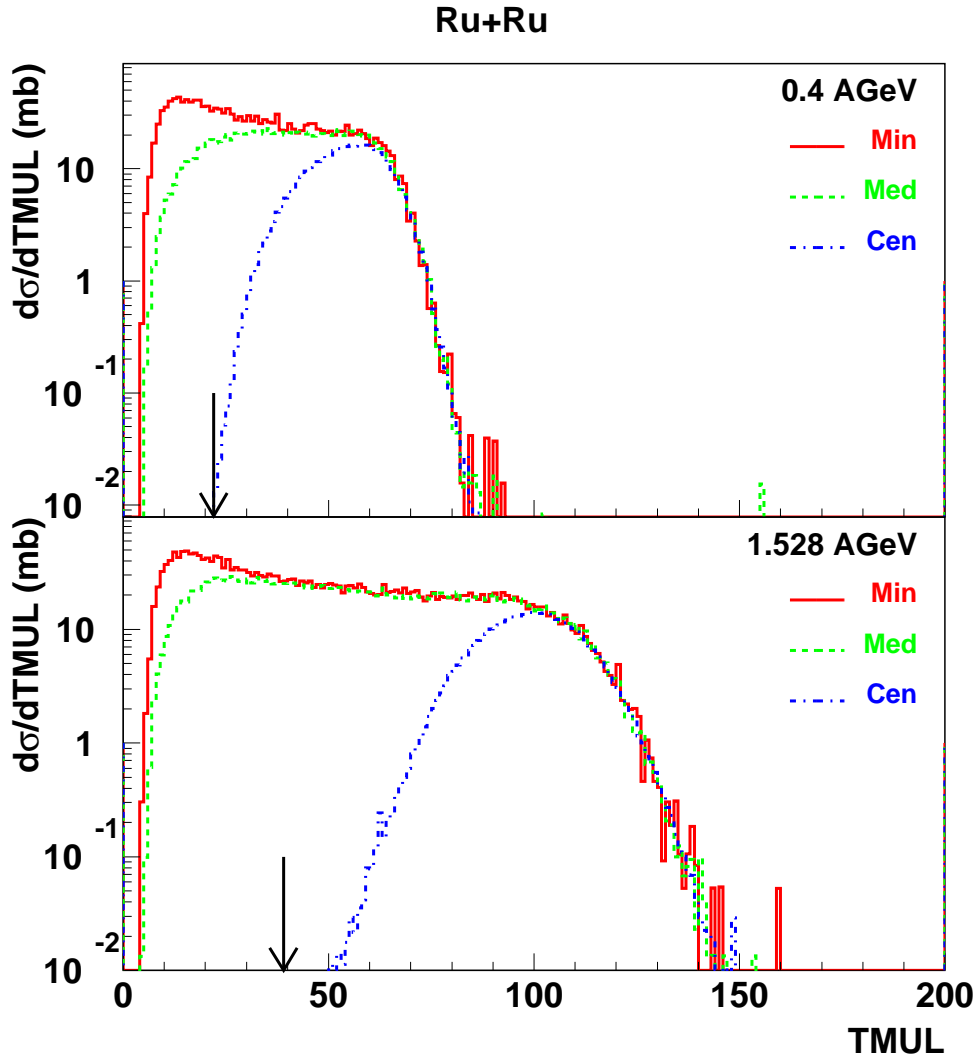


Figure 3.3: Total multiplicity distributions of the charged particles in Ru+Ru collisions at 0.4 (top) and 1.528 (bottom) AGeV: Minimum bias (solid line: Min), Medium bias (dashed line: Med), Central bias (dashed-dot line: Cen) are shown. The downward arrows indicate the lowest cut values for the centrality conditions for this analysis.



the CDC (CMUL) and PLAWA (PMUL):

$$\text{TMUL} = \text{CMUL} + \text{PMUL}. \quad (3.1)$$

The total multiplicity distributions are weighted by the scaling factor of each trigger. The solid, dashed, and dashed-dot lines represent the Minimum, Medium, and Central bias events, respectively.

The collision centrality has been estimated by applying the sharp cut off approximation to the total multiplicity distributions. The total geometrical cross section of Ru+Ru collisions (σ_{tot}^{RuRu}) is 3794 mb from the following formula:

$$\sigma_{geo}(\text{mb}) = 10\pi r^2 = 10\pi r_0^2 (A_{beam}^{1/3} + A_{target}^{1/3})^2, \quad (3.2)$$

where $r_0 = 1.2$ fm and A is the mass number. The geometrical impact parameter can be estimated by

$$b_{geo}(\text{fm}) = \sqrt{\frac{\sigma_{geo}}{10\pi}}. \quad (3.3)$$

The total multiplicity distribution for the Minimum bias condition was not completely measured at the low multiplicity due to the background events. For the most central events in the spectrum analysis, we selected almost the same fraction of σ_{geo} at both beam energies as summarized in table 3.1. For the flow analysis, the three kinds of centralities were selected as summarized in table 3.2. The downward arrows in figure 3.3 indicate the lowest cut values of centrality selection.

E_{beam} (A GeV)	System	Centrality	TMUL	σ_{geo} (mb)	b_{geo} (fm)	$\sigma_{geo}/\sigma_{tot}$ (%)
0.4	Ru + Ru	Central	≥ 63	≤ 99	≤ 1.78	2.6
1.528	Ru + Ru	Central	≥ 110	≤ 95	≤ 1.75	2.5

Table 3.1: Centrality selections for the central events in the TMUL distributions.



E_{beam} (AGeV)	System	Centrality	TMUL	σ_{geo} (mb)	b_{geo} (fm)	$\sigma_{geo}/\sigma_{tot}$ (%)
0.4	Ru + Ru	TMUL02	≥ 61	≤ 134	≤ 2	≤ 3.5
		TMUL24	44 ~ 60	135 ~ 507	2 ~ 4	3.5 ~ 13
		TMUL46	22 ~ 43	508 ~ 1120	4 ~ 6	13 ~ 30
1.528	Ru + Ru	TMUL03	≥ 97	≤ 285	≤ 3	≤ 7.5
		TMUL35	71 ~ 96	286 ~ 794	3 ~ 5	7.5 ~ 21
		TMUL57	39 ~ 70	795 ~ 1550	5 ~ 7	21 ~ 41

Table 3.2: Centrality selections with TMUL distributions for the central (TMUL02, TMUL03), semicentral (TMUL24, TMUL35), and peripheral (TMUL46, TMUL57) collision events.

3.3 Track selection

For the selection of good quality tracks, the number of hits for each track are used in the CDC (npt_{CDC}) and Helitron ($npt_{Helitron}$). The $npt_{CDC} \geq 33$ and $npt_{Helitron} \geq 15$ are applied. The geometrical acceptance of the sub-detectors in polar angle are applied as summarized in table 3.3. The proton and deuteron can be identified from the information of the CDC and Helitron. IN addition, the information of the Barrel and the PLAWA were used to separate the hydrogen (Z_1) and helium (Z_2) isotopes.

In the following sub-chapters, the cut condition for the distances between each track and the event vertex ($d0_{free}$ and $z0_{free}$), the matching condition between the CDC and Barrel ($\Delta z, \Delta\phi, \chi^2$), and the matching condition between the Helitron and PLAWA ($\Delta\theta, \Delta\phi$) will be presented.

3.3.1 $d0_{free}$ and $z0_{free}$ of CDC

The distance between each track and the event vertex in the CDC has been examined. The large deviation can occur due to the finite detector res-



Detectors	θ_{lab} ($^{\circ}$)
CDC	33 \sim 140
Barrel	39 \sim 130
Helitron	9 \sim 26
PLAWA	7 \sim 30

Table 3.3: Polar angle acceptance of sub-detectors.

olution and the weakly decaying resonances. Here, we take into account the deviation: one is due to the reconstructed mirror tracks in xy plane ($d0_{free}$) and the other is due to the finite hit resolution along the z -axis ($z0_{free}$). Primarily, $d0_{free}$ and $z0_{free}$ depend on the momentum of particles as shown in figure 3.4. The spreads around zero of $d0_{free}$ and $z0_{free}$ are getting narrower toward high momentum. For this analysis, the distributions of $d0_{free}$ and $z0_{free}$ are divided into each 100 MeV/ c momentum bin. Then, each distribution is fitted by the Gaussian function. The cut at $\pm 3\sigma$ were used for this analysis.

3.3.2 Matching conditions between CDC and Barrel

The reconstructed tracks in the CDC are extrapolated to the location of the Barrel at the radius of 111 cm. When the extrapolated tracks of the CDC and the hits in the Barrel are matched in a certain allowance, we consider that the radius of track curvature (ρ) is greater than the half of the Barrel radius ($R/2 = 55.5$ cm). Thus, the transverse momentum of the particle can be calculated as

$$p_t = B\rho Q. \quad (3.4)$$

The quality of matching has been determined by

$$\chi^2 = \left(\frac{\Delta z}{\sigma_z}\right)^2 + \left(\frac{\Delta\phi}{\sigma_\phi}\right)^2, \quad (3.5)$$

where Δz is the distance between the extrapolated track location of the CDC and the hit of the Barrel on the z -axis, $\Delta\phi$ is the difference between the



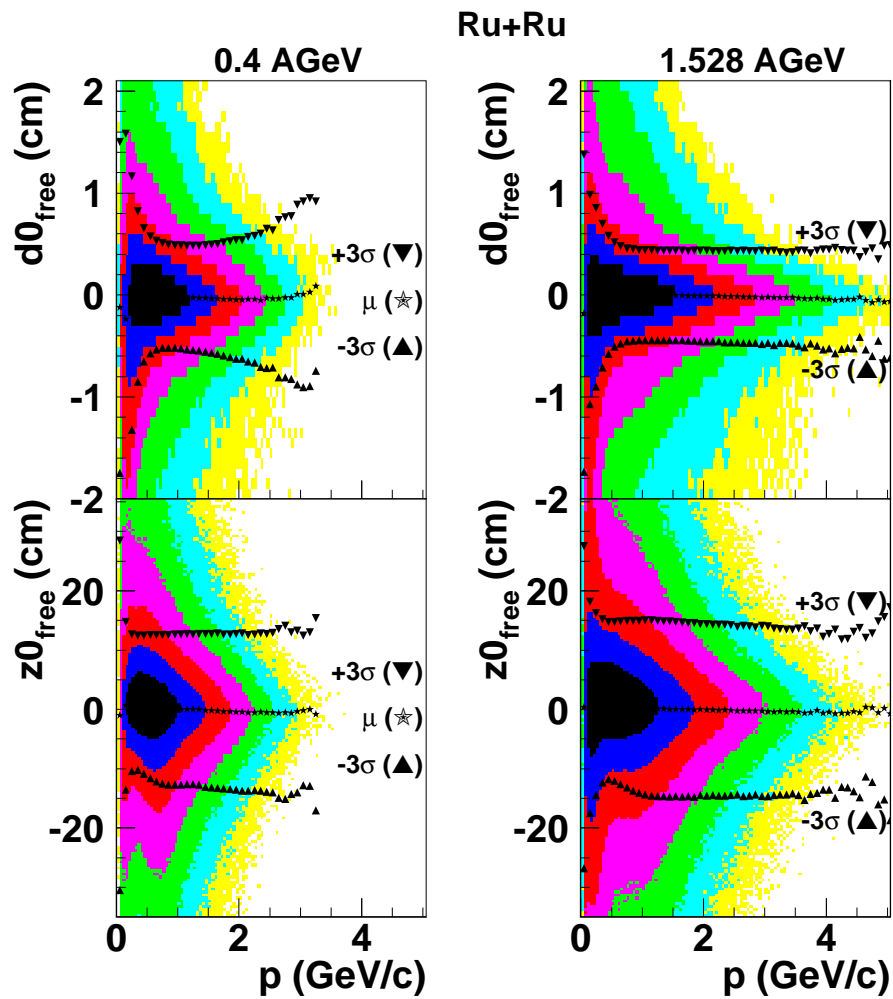


Figure 3.4: Deviation between tracks and primary event vertex as a function of momentum in Ru+Ru collisions at 0.4 (left) and 1.528 (right) AGeV: $\pm 3\sigma$ from the Gaussian fit functions and the mean values, which were used for this analysis, are shown.



azimuthal angle of the extrapolated track of the CDC and the azimuthal angle of the Barrel hit. Here, $\sigma_z = 15$ cm and $\sigma_\phi = 2^\circ$ were used. In order to estimate the proper cut criteria, the distributions of Δz and $\Delta\phi$ are divided into each 100 MeV/ c momentum bin. Then, each distribution is fitted by the Gaussian function. The momentum dependences of the 3σ deviations for the matching variables are shown in figure 3.5. Since the 3σ deviations of $\Delta\phi$ and Δz are almost independent of the momentum, we applied the constant cuts as $-14 \text{ cm} \leq \Delta z \leq 18 \text{ cm}$, $|\Delta\phi| \leq 1.5^\circ$, and $\chi^2 \leq 2.5$ as shown in figure 3.5 by the thick lines.

3.3.3 Matching conditions between Helitron and PLAWA

The extrapolated tracks of the Helitron and hits in the PLAWA are matched in order to filter good quality tracks. It also serves to separate the hydrogen (Z_1) and helium (Z_2) isotopes. $\Delta\theta$ and $\Delta\phi$ are the angle difference of the polar and azimuthal angles between the extrapolated track of the Helitron and the hit in the PLAWA. In order to estimate the proper cut criteria, the distributions of $\Delta\theta$ and $\Delta\phi$ are divided into each 100 MeV/ c momentum bin. Then, each distribution is fitted by the Gaussian function. The spread around zero of $\Delta\theta$ is getting wider toward high momentum as shown in figure 3.6. The thick lines indicate the cut conditions for this analysis: $|\Delta\theta| \leq 3.5^\circ$, and $|\Delta\phi| \leq 3.0^\circ$.

3.4 Charge selection

In order to identify the heavier fragments (^3H , ^3He , and ^4He), we need to separate the particles by using the charge information from the measured particle velocities of the Barrel the energy loss of the CDC in the backward. Similarly, we can repeat for the PLAWA and the Helitron in the forward. The results are shown in figure 3.7. We can clearly separate the charge by using the correlation between the CDC and Barrel at 0.4 (top-left) and 1.528 (top-right)



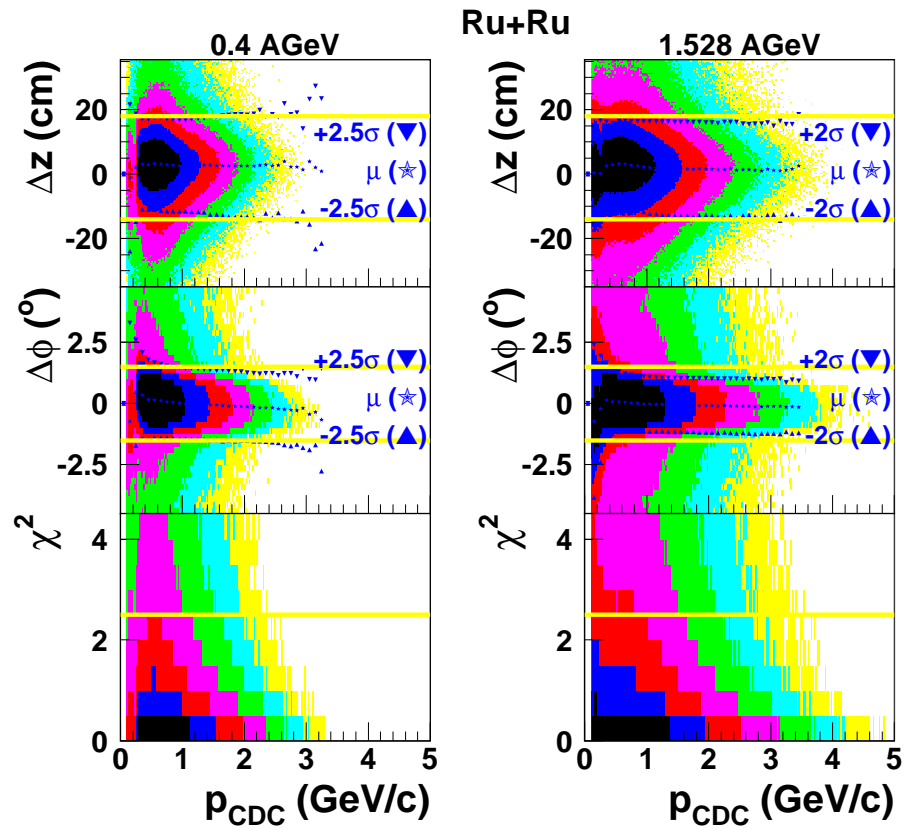


Figure 3.5: Matching condition between the extrapolated CDC tracks and the Barrel hits in Ru+Ru collisions at 0.4 (left) and 1.528 (right) AGeV. The thick lines indicate the cut conditions for this analysis: $-14 \text{ cm} \leq \Delta z \leq 18 \text{ cm}$, $|\Delta\phi| \leq 1.5^\circ$, and $\chi^2 \leq 2.5$.



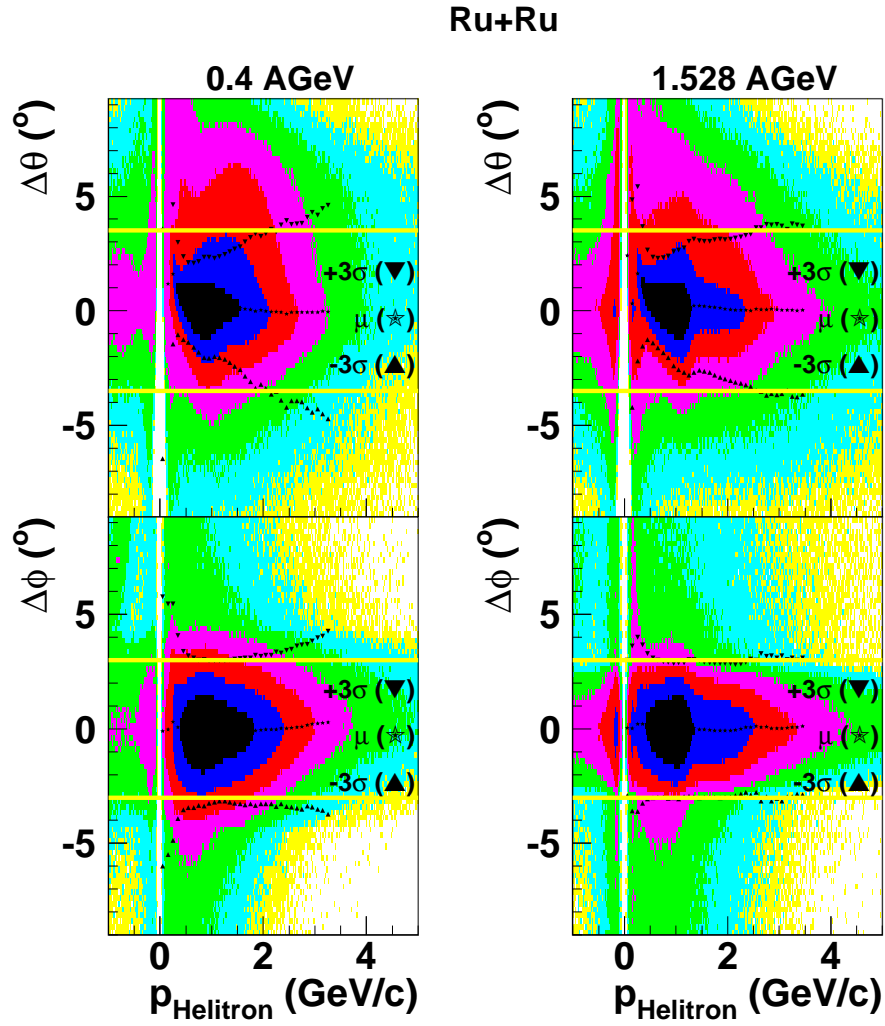


Figure 3.6: Matching condition between the extrapolated Helitron tracks and the PLAWA hits in Ru+Ru collisions at 0.4 (left) and 1.528 (right) AGeV: The thick lines indicate the cut conditions for this analysis: $|\Delta\theta| \leq 3.5^\circ$, and $|\Delta\phi| \leq 3.0^\circ$.



AGeV. But the Helitron shows the limited capability for slow particles, which is the decision ambiguity of the track sign and insufficient rejection power of mirror track particularly at $E_{beam} > 1$ AGeV. This problem in the Helitron comes from the smaller active volume than the CDC [43]. In order to avoid the unclear charge separation, we only take the data β_{PLA} less than 0.8 at 1.528 AGeV. Figure 3.8 shows the charge distribution of the Barrel (Z_{Barrel}) and PLAWA (Z_{PLAWA}) with the proper charge cut for $Z=1$ and $Z=2$.

Furthermore, the charge information ($Z_{Helitron}$) from the Helitron has been used to remove the background hits, which were declared as $Z=1$ although they were $Z=2$ particles from the PLAWA, and vice versa. In figure 3.9, the correlation between the charge and mass ($m_{Helitron}$) of Helitron is shown in Ru+Ru collisions at 0.4 (top-left) and 1.528 (top-right) AGeV, respectively. Note that even after the charge separation cut to the PLAWA in figure 3.8 was applied, the background in the bottom-right plot for $Z_{PLAWA}=2$ was not negligible. Therefore we devised the additional charge cut (dashed-line) of the Helitron to remove the background in the lower-left panel of figure 3.9, which is from the wrong charge assignment. Finally, $Z=1$ is defined as $Z_{Helitron} < -0.2m_{Helitron}+2.1$ on the bottom-left plot and $Z=2$ is defined as $Z_{Helitron} > -0.2m_{Helitron}+2.1$ on the bottom-right plot in figure 3.9.

Similar to the Helitron analysis, we have investigated the correlations between the charge and mass determined by the CDC and the Barrel in Ru+Ru collisions at 0.4 (top) and 1.528 (bottom) AGeV in figure 3.10. Additionally, the correlations between the charge of the PLAWA and the mass of the Helitron (right-side) in Ru+Ru collisions at 0.4 (top) and 1.528 (bottom) AGeV are also shown in figure 3.10. The dashed-lines indicate the charge cut used in this analysis.

3.5 Particle identification (PID)

After applying the matching condition and charge selection criteria, the correlations between the momentum of the drift chamber and the velocity of the scintillation detector were obtained. In figure 3.11, the correlations between the momentum of the Helitron ($p_{Helitron}$) and the velocity of the



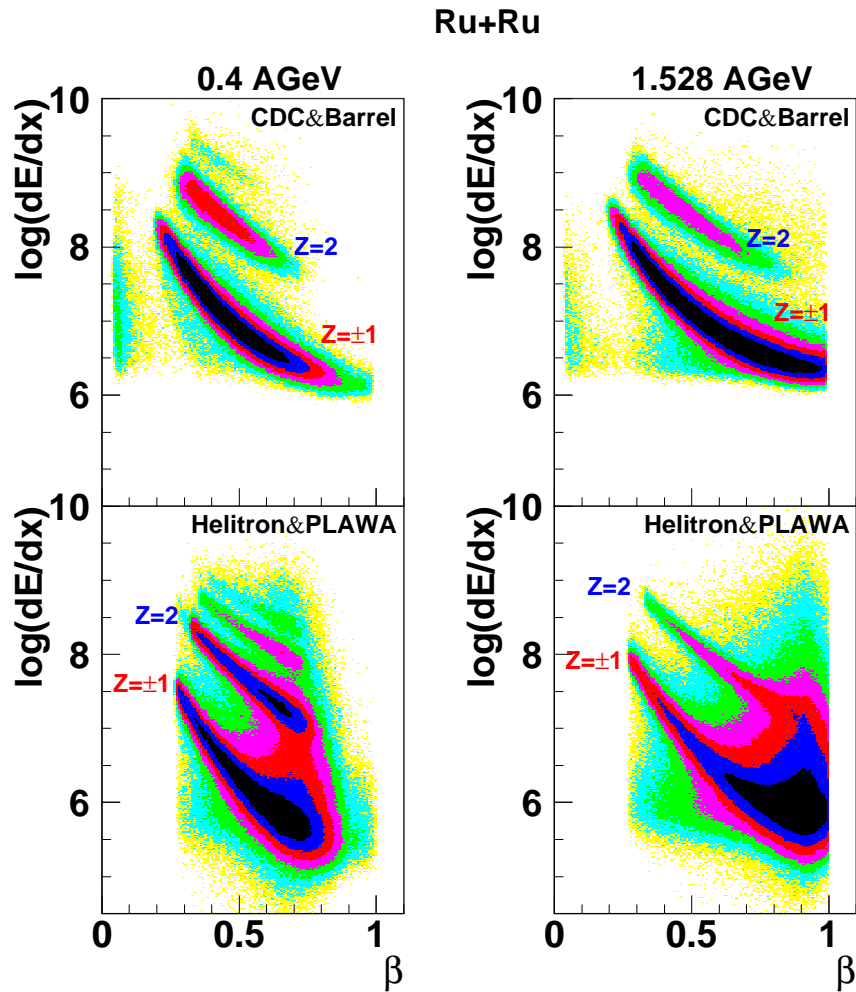


Figure 3.7: Correlation between the energy loss of the drift chamber (CDC and Helitron) and the velocity β measured by the scintillation detectors (Barrel and PLAWA): the correlation between the CDC and Barrel at 0.4 (top-left) and 1.528 (top-right) AGeV and the correlation between the Helitron and PLAWA at 0.4 (bottom-left) and 1.528 (bottom-right) AGeV are shown.



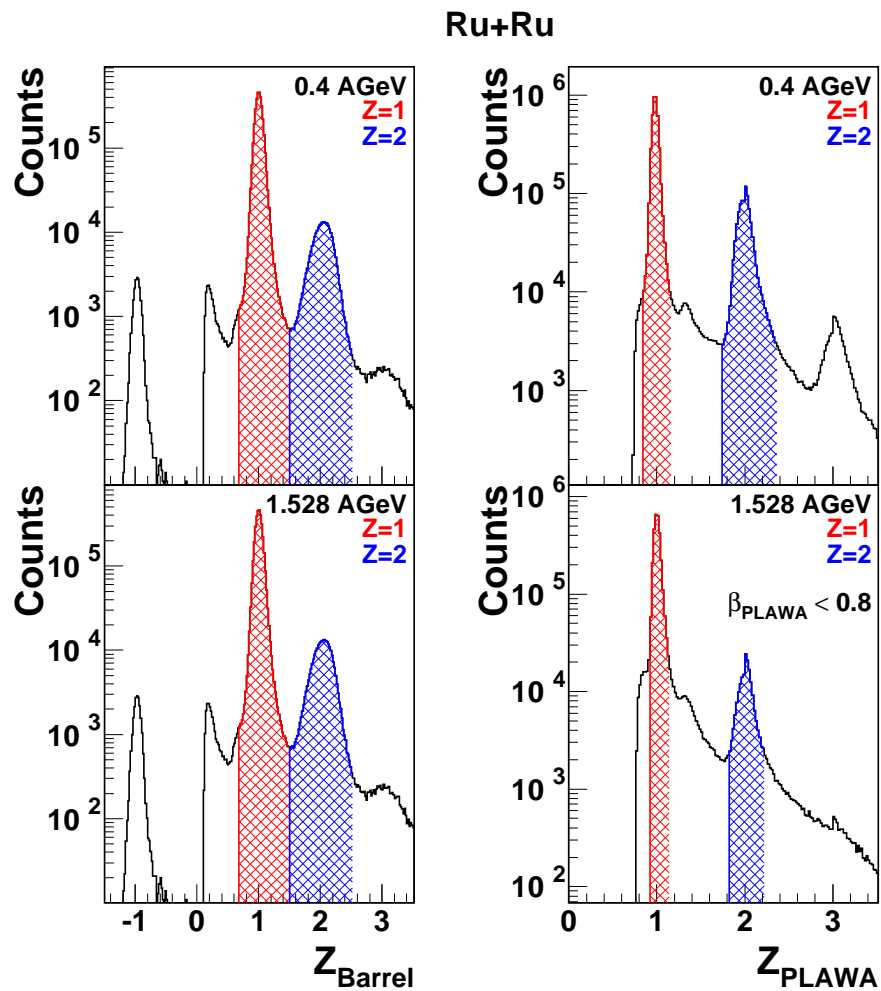


Figure 3.8: Charge distribution in the Barrel (left) and PLAWA (right) at 0.4 (top) and 1.528 (bottom) AGeV. The figure also indicate the charge cut condition, which is represented by the shaded area, for this analysis.



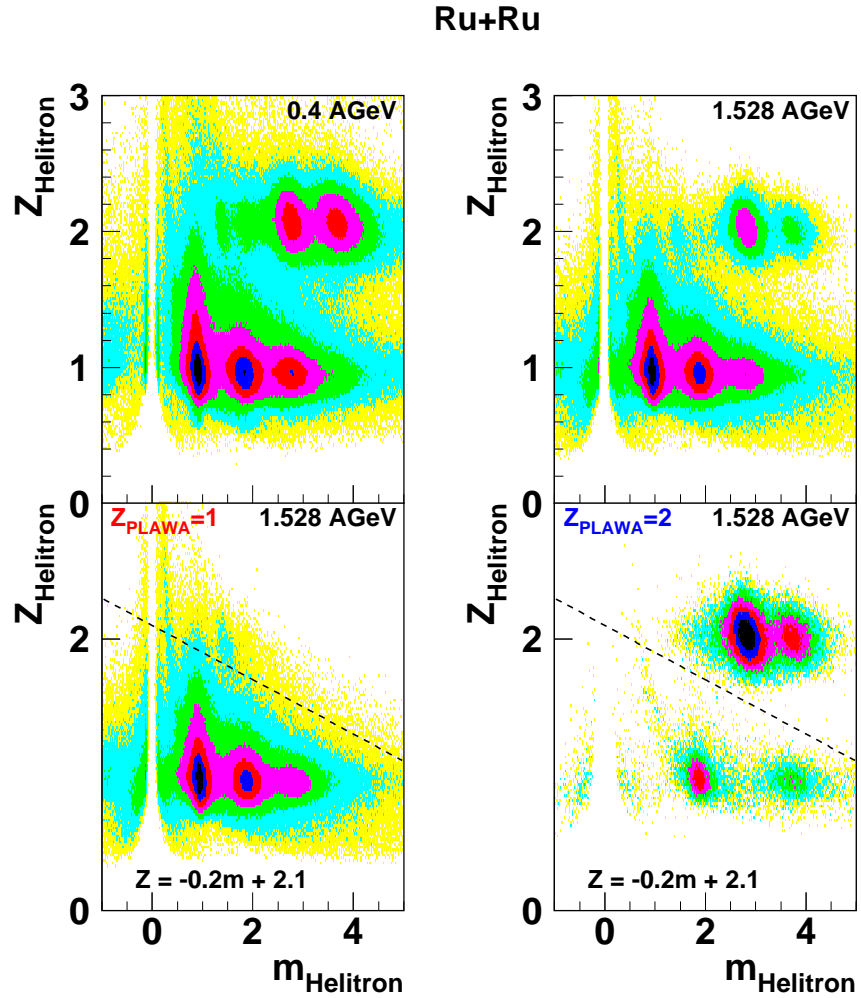


Figure 3.9: Correlation between the charge ($Z_{Helitron}$) and mass ($m_{Helitron}$) of the Helitron in Ru+Ru collisions at 0.4 (top-left) and 1.528 (top-right) AGeV. After applying the charge cut (Z_{PLAWA}) of the PLAWA in figure 3.8, the charge cut (dashed-line) of the Helitron has been applied to remove the background due to wrong charge assignment.



Ru+Ru

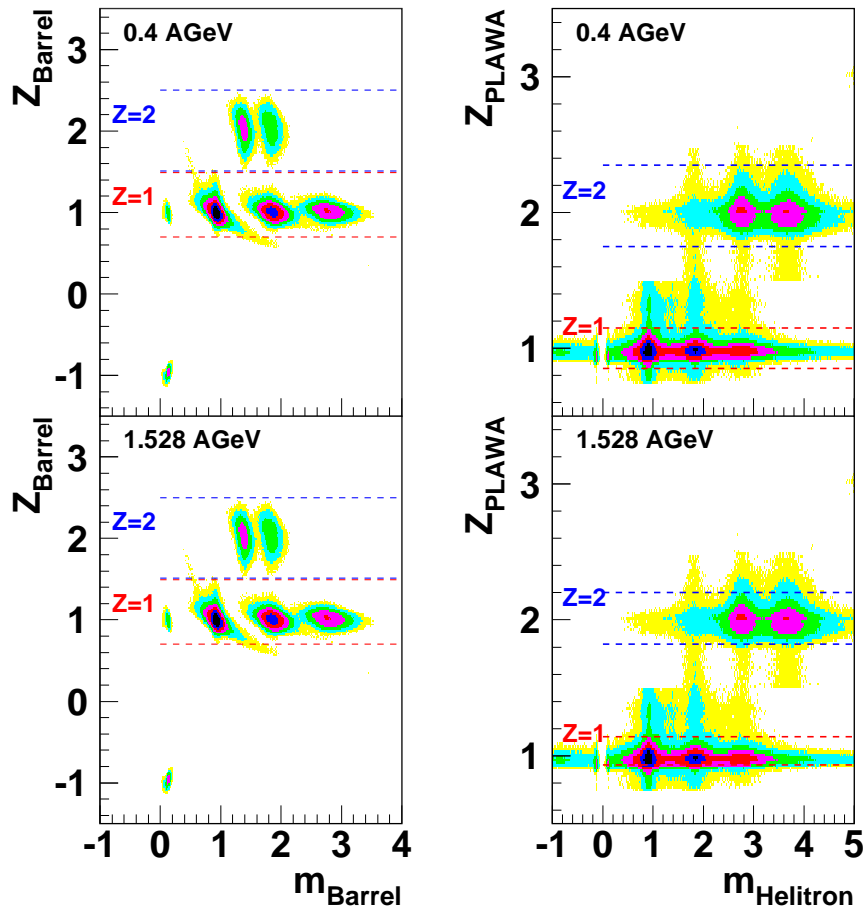


Figure 3.10: Correlation between the charge (Z_{Barrel}) and mass (m_{Barrel}) of the Barrel (left-side) and the correlation between the charge of the PLAWA (Z_{PLAWA}) and the mass of the Helitron ($m_{Helitron}$) (right-side) in Ru+Ru collisions at 0.4 (top) and 1.528 (bottom) AGeV. The dashed-lines imply the charge cut.



PLAWA (β_{PLAWA}) in Ru+Ru collisions at 0.4 (left) and 1.528 (right) AGeV are shown. The correlation of $|Z|=1$ (top) and that of $Z=2$ (bottom) are shown together with the expected particle mass lines which are represented by the dashed lines. Now the correlations between the mass ($m_{Helitron}$) and momentum ($p_{Helitron}$) of the Helitron are used for the PID in Ru+Ru collisions at 0.4 (left) and 1.528 (right) AGeV in figure 3.12. In order to estimate the proper mass cut criteria, the mean of the mass distribution (squares) and the standard deviation (circles) of the proton ($\pm 3\sigma$) and others ($\pm 2\sigma$) were obtained in each 100 MeV/ c momentum bin. The dashed-lines are the applied mass cut for the PID. The velocity cut ($\beta_{PLA} < 0.8$) has been applied at 1.528 AGeV due to the limited performance of the Helitron (see section 3.4).

In figure 3.13, the correlations between the momentum of the CDC (p_{CDC}) and the velocity of the Barrel (β_{Barrel}) are shown in Ru+Ru collisions at 0.4 (left) and 1.528 (right) AGeV: $|Z|=1$ on the top and $Z=2$ on the bottom plots. The calculated particle mass lines are drawn in the dashed lines. The correlations between the mass of the Barrel (m_{Barrel}) and momentum of the CDC (p_{CDC}) are used for the PID in Ru+Ru collisions at 0.4 (left) and 1.528 (right) AGeV in figure 3.14. In order to estimate the proper mass cut criteria, the mean of the mass distribution (squares) and the standard deviation (circles) of the proton ($\pm 3\sigma$) and others ($\pm 2\sigma$) were obtained in each 100 MeV/ c momentum bin. The dashed-lines are the applied mass cut for the PID.

The detected particles in the CDC can be lost by reasons that the low velocity particles are not reached up to the Barrel and there is the limitation of polar and azimuthal acceptance of the Barrel. So, we have to consider these unmatched tracks of CDC with the hits of the Barrel. The CDC can identify the pion, proton and deuteron by itself from the correlation between the energy loss and momentum of incident particles. In the left-side plots at figure 3.15, the correlation between the energy loss and the momentum of CDC in Ru+Ru collisions at 0.4 (top) and 1.528 (bottom) AGeV. The expected particle mass lines (dashed-lines) have drawn by using the equation 2.3. The correlation between the mass (m_{CDC}) and momentum (p_{CDC}) of the unmatched CDC tracks are used for the PID in Ru+Ru collisions at 0.4 (left) and 1.528 (right) AGeV in the right-side plots in figure 3.15. In order to estimate the proper mass cut criteria, we also obtained the mean of the mass



distribution (squares) and the standard deviation (circles) of the proton ($\pm 3\sigma$) and deuteron ($\pm 2\sigma$) in each 100 MeV/ c momentum bin. The dashed-lines are the applied mass cut for the PID.

3.6 Efficiency correction

The real tracks in the FOPI experiment can be lost due to the finite detector resolution and the track quality cut for the sub-detectors [44]. The matching efficiencies between the drift chambers (CDC and Helitron) and the scintillation detectors (Barrel and PLAWA) have been obtained by using the experimental data. The track reconstruction efficiency of the CDC has been calculated by using the IQMD simulation.

3.6.1 Matching efficiency between Helitron and PLAWA

The matching efficiency between the Helitron and PLAWA in $9^\circ \leq \theta_{lab} < 26^\circ$ has been estimated dividing the number of tracks in the Helitron after matching cut by the number of hits in the PLAWA before the matching cuts. In figure 3.16, the matching efficiencies of the $|Z|=1$ (left) and $Z=2$ (right) between the Helitron and PLAWA have been calculated in Ru+Ru collisions at 0.4 AGeV. The assumption is that the efficiency of the PLAWA is 100 % at 0.4 AGeV. It is fitted by the 4th-order polynomial function and the fitted results are applied for the correction of the matching cut. At the mid-rapidity region, the efficiencies of $|Z|=1$ and $Z=2$ vary from 45 to 85 % and from 50 to 80 %, respectively, as a function of the polar angle. Near beam rapidity region, the efficiency of $Z=2$ fall down little bit above 20° due to the limited PID performance of the Helitron. The matching efficiency at 0.4 AGeV strongly depends on the polar angle but it has a weak dependence on the rapidity.

After applying the matching cut at 1.528 AGeV, the hits in the PLAWA may include the background hits which can be removed by the cut as shown



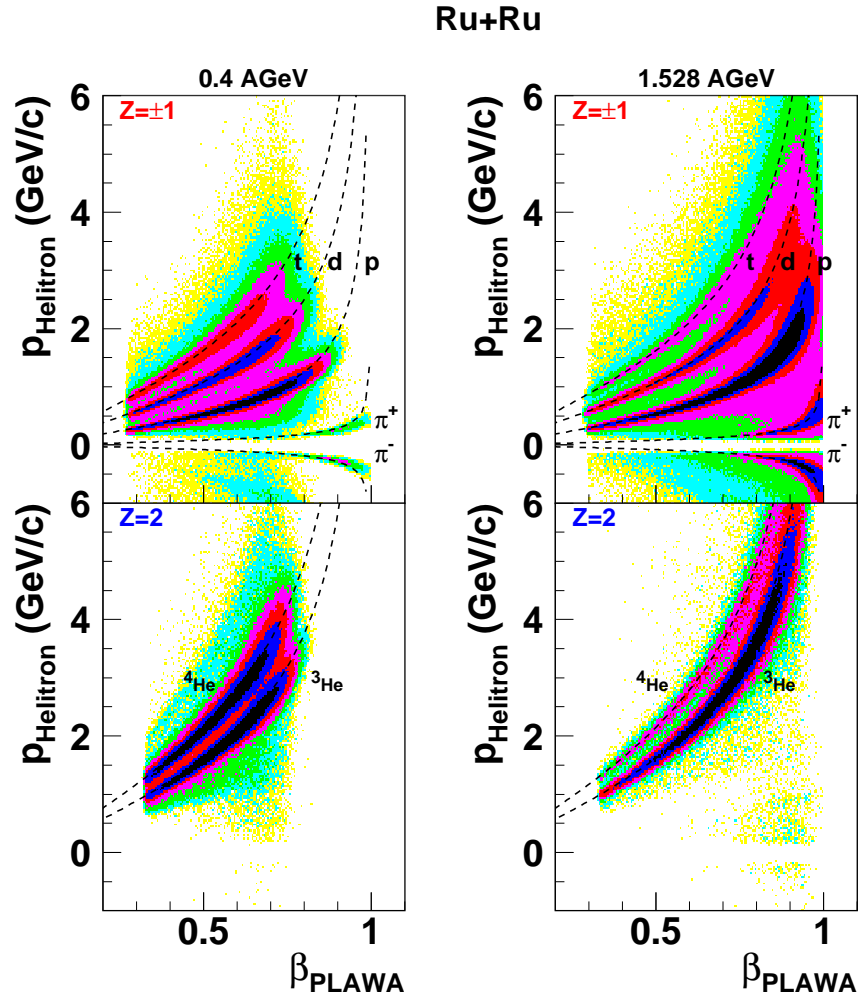


Figure 3.11: Correlation between the momentum of the Helitron ($p_{Helitron}$) and the velocity of PLAWA (β_{PLAWA}) in Ru+Ru collisions at 0.4 (left) and 1.528 (right) AGeV. The correlations for $|Z|=1$ (top) and $Z=2$ (bottom) are shown with the expected particle mass lines drawn by the dashed lines.



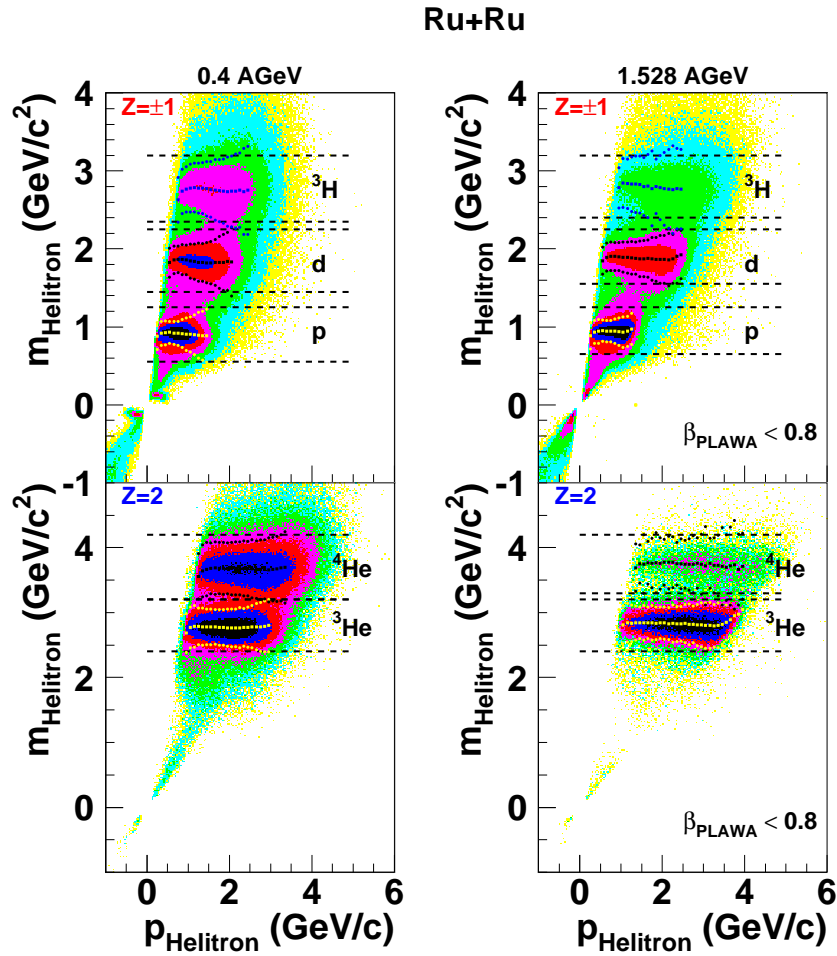


Figure 3.12: Correlation between the mass ($m_{Helitron}$) and momentum ($p_{Helitron}$) of the Helitron in Ru+Ru collisions at 0.4 (left) and 1.528 (right) AGeV. The mean values (squares) and the standard deviations (circles) of the proton ($\pm 3\sigma$) and others ($\pm 2\sigma$) are drawn in each 100 MeV/c momentum bin. The dashed lines are the applied mass cuts for the PID. The velocity cut ($\beta_{PLAWA} < 0.8$) has been applied at 1.528 AGeV.



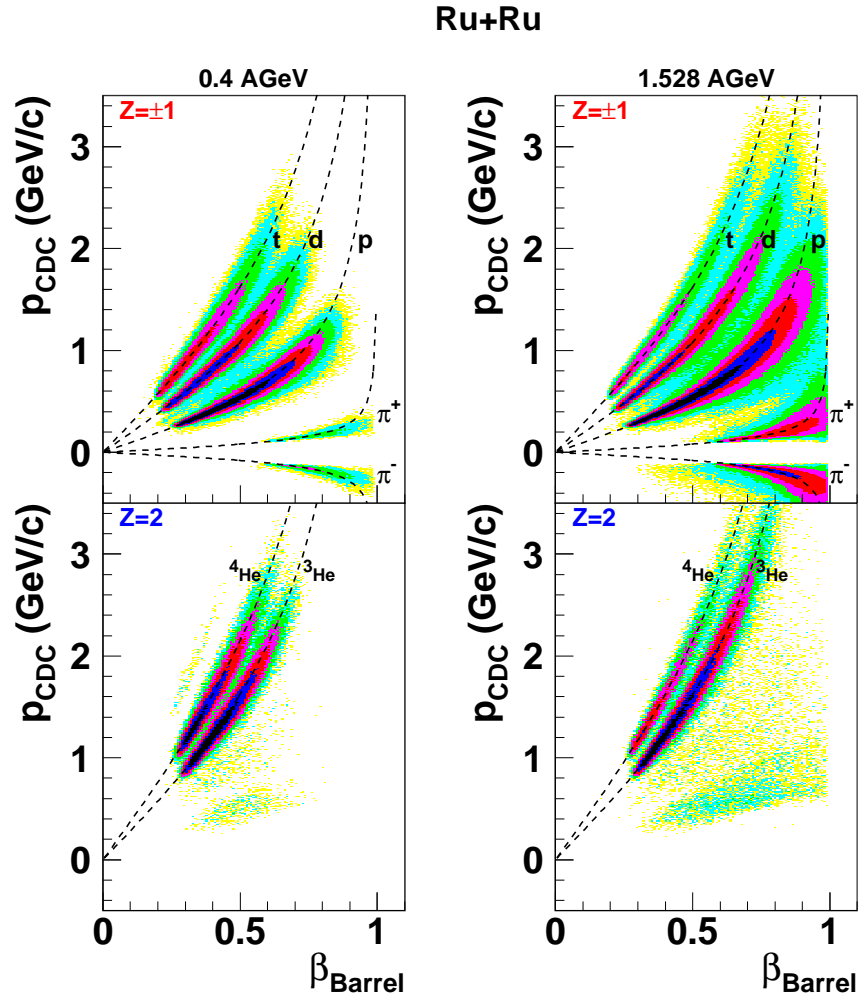


Figure 3.13: Correlation between the momentum of the CDC (p_{CDC}) and the velocity of Barrel (β_{Barrel}) in Ru+Ru collisions at 0.4 (left) and 1.528 (right) AGeV. The correlations for $|Z|=1$ (top) and $Z=2$ (bottom) are shown with the expected particle mass lines drawn by the dashed lines.



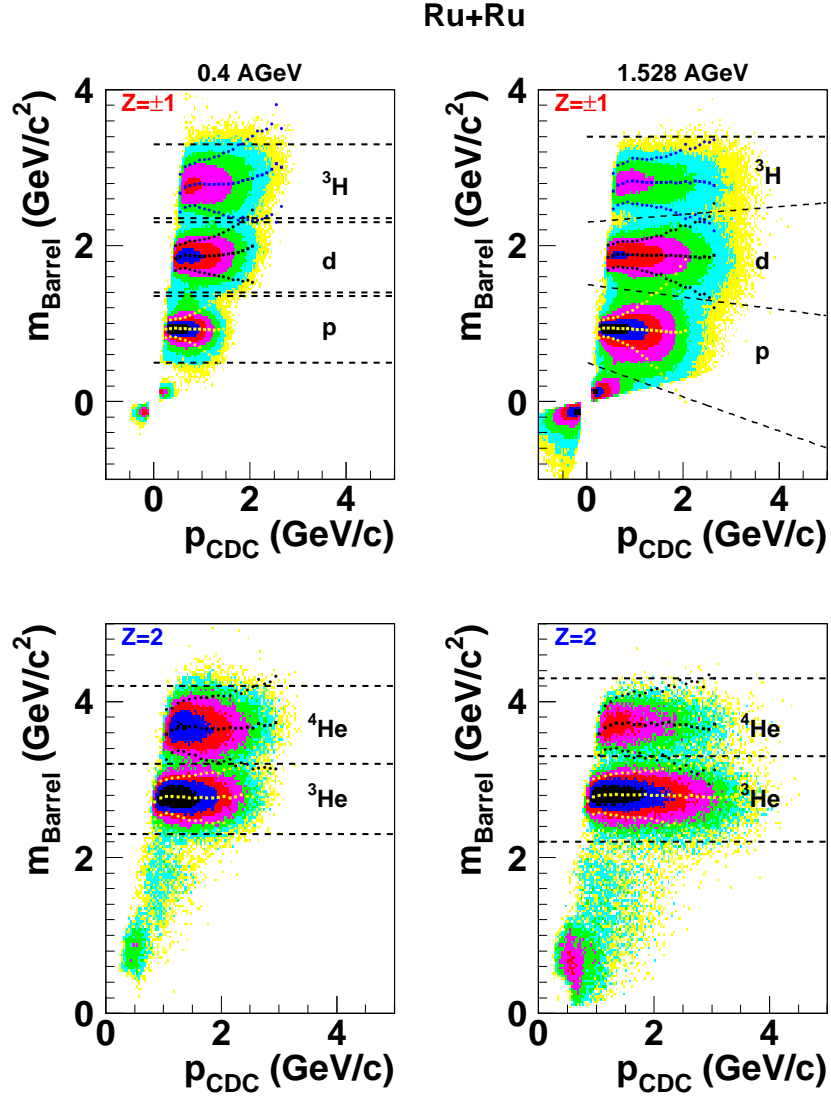


Figure 3.14: Correlation between the mass of the Barrel (m_{Barrel}) and the momentum of the CDC (p_{CDC}) in Ru+Ru collisions at 0.4 (left) and 1.528 (right) AGeV. The mean values (squares) and the standard deviations (circles) of the proton ($\pm 3\sigma$) and others ($\pm 2\sigma$) are drawn for each 100 MeV/c momentum bin. The dashed lines are the applied mass cuts for the PID.



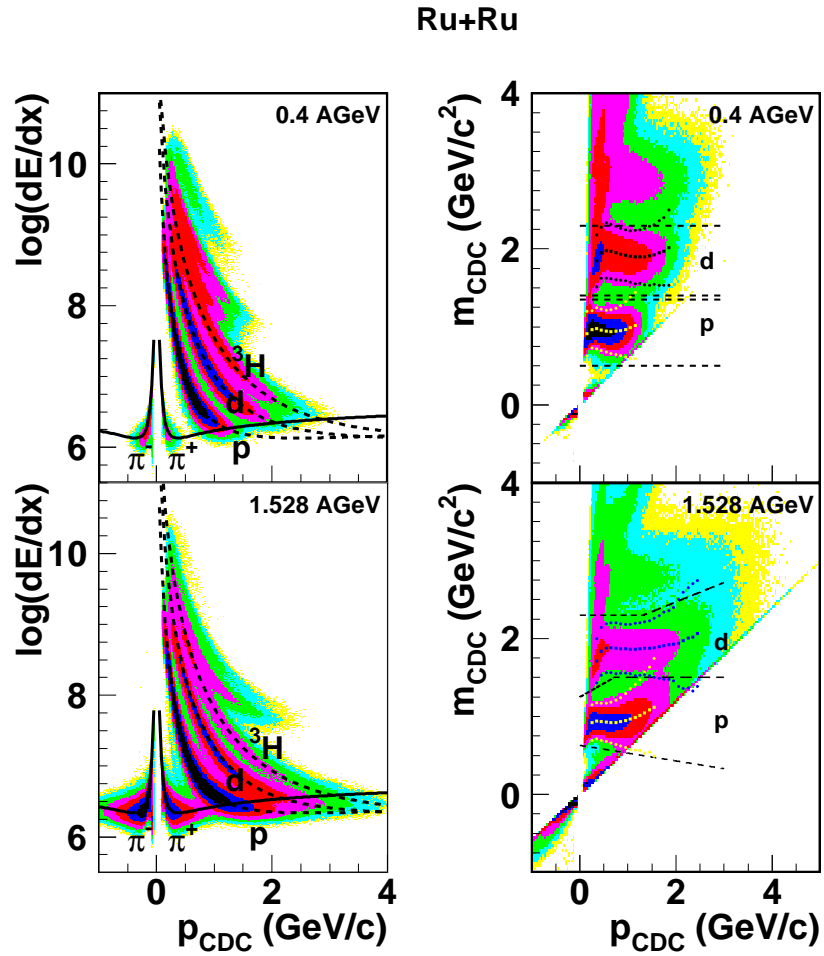


Figure 3.15: Correlations between the energy loss and momentum (p_{CDC}) of the CDC in Ru+Ru collisions at 0.4 (top-left) and 1.528 (bottom-left) AGeV. The correlations between the mass (m_{CDC}) and momentum (p_{CDC}) of the unmatched CDC tracks in Ru+Ru collisions at 0.4 (top-right) and 1.528 (bottom-right) AGeV. The dashed lines are the applied mass cuts for the PID in the right-side plots. See the text for more details.



in figure 3.9. Therefore, 100% efficiency of the PLAWA at 1.528 AGeV is assumed after the charge cut shown in figure 3.9. In figure 3.17, the mass distributions of the Helitron for $|Z|=1$ (top) and $Z=2$ (bottom) for $0.3 < \beta_t \gamma \leq 0.35$ and $-0.3 \leq y^{(0)} < -0.2$ are shown in Ru+Ru collisions at 1.528 AGeV. The background (closed circles) has been fitted by the linear function in order to estimate the background (dashed line). Subsequently, the matching efficiencies of the hydrogen (left) and the helium (right) isotopes between the Helitron and PLAWA as a function of the $\beta_t \gamma$ has been calculated in Ru+Ru collisions at 1.528 AGeV. As shown in figure 3.18, the matching efficiencies are fitted by the 4th-order polynomial functions and the fitted functions are applied for the correction of the matching cut. The matching efficiency at 1.528 AGeV strongly depends on the polar angle and the rapidity. At the mid-rapidity region, the efficiencies of $|Z|=1$ and $Z=2$ vary from 10 to 70 % and from 40 to 75 %, respectively, as a function of the $\beta_t \gamma$.

3.6.2 Matching efficiency between CDC and Barrel

In order to identify the heavier fragments (^3H , ^3He , and ^4He), the charge information of the particles is needed from the Barrel. Some particles, detected by the CDC, can not reach the Barrel due to the low momentum or the geometrical acceptance mismatching (Barrel covers about 75 % of the full azimuthal angle [44]). During the matching process, the background can be reduced, but at the same time, the real tracks in the CDC can be also lost. The matching efficiency between the CDC and Barrel is defined by the ratio of the number of hits in the Barrel after applied the matching cut to the number of tracks in the CDC before applied the matching cut. The assumption is that the matching efficiency of the deuteron is the same as that of the heavier fragments.

In figure 3.19, the matching efficiency of the deuteron between the CDC and Barrel as a function of transverse momentum is shown in Ru+Ru collisions at 0.4 (left) and 1.528 (right) AGeV. The matching efficiencies are fitted by the linear function (thick solid lines) in the p_t region where the deuteron can be identified, and the linear functions are extended to the higher p_t region (thin solid lines). The matching efficiencies show a small dependence on p_t



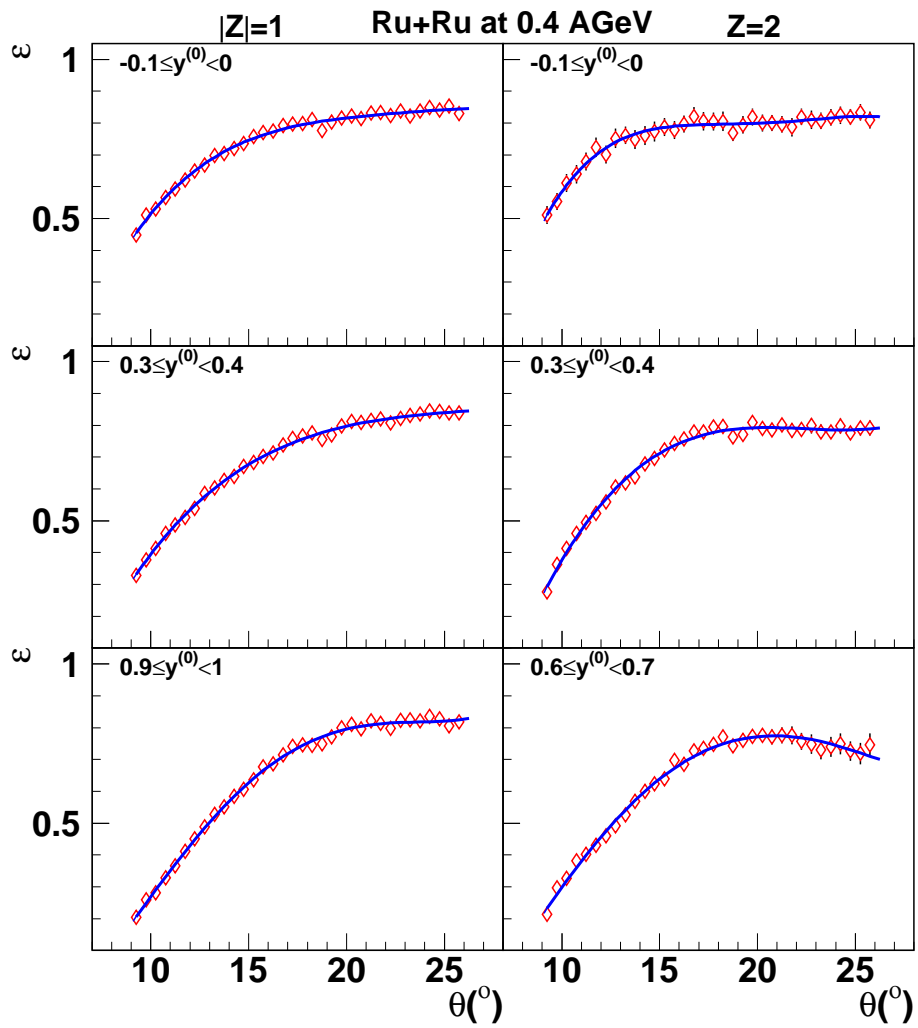


Figure 3.16: Matching efficiencies of the hydrogen (left) and the helium (right) isotopes between the Helitron and the PLAWA in Ru+Ru collisions at 0.4 AGeV. The data are fitted by the 4th-order polynomial functions.



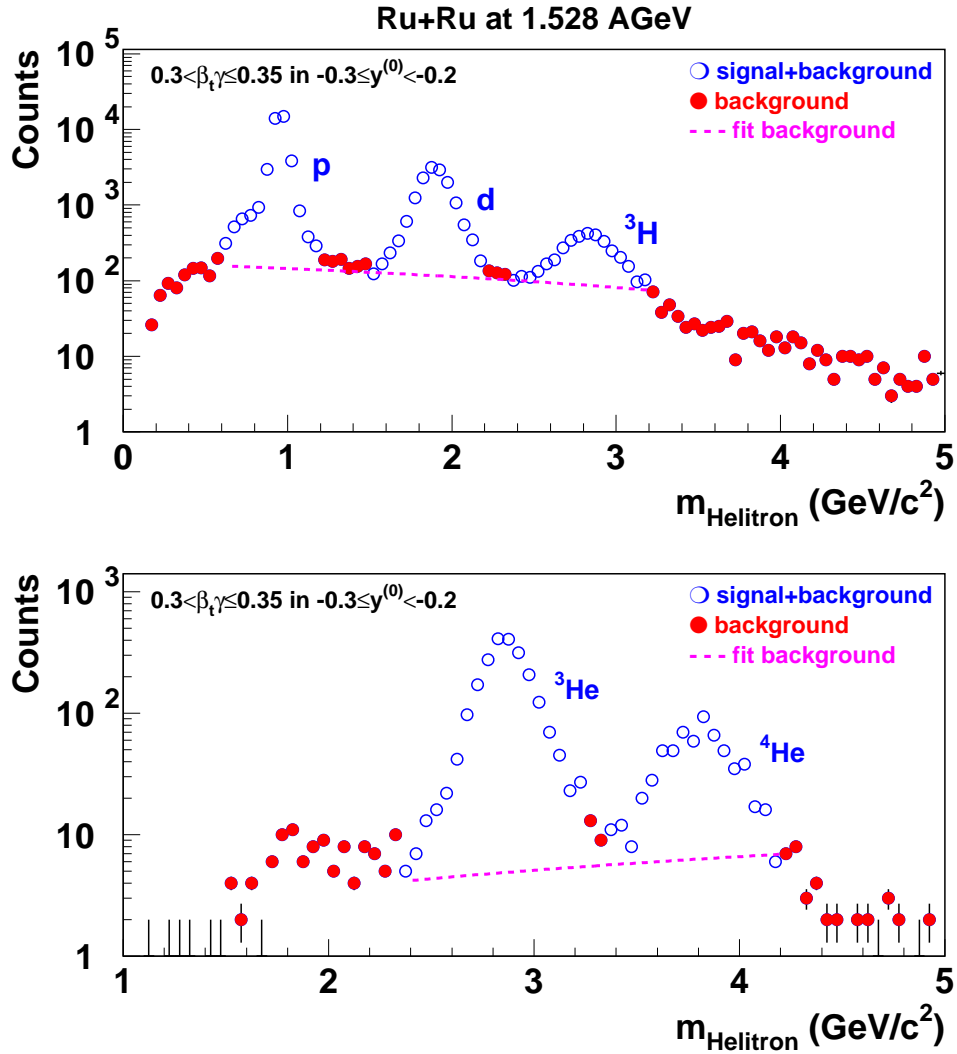


Figure 3.17: Mass distributions from the Helitron for $|Z|=1$ (top) and $Z=2$ (bottom) at $0.3 < \beta_t \gamma \leq 0.35$ and $-0.3 \leq y^{(0)} < -0.2$ in Ru+Ru collisions at 1.528 AGeV. The background (closed circles) has been fitted by the linear function in order to estimate the background (dashed line).



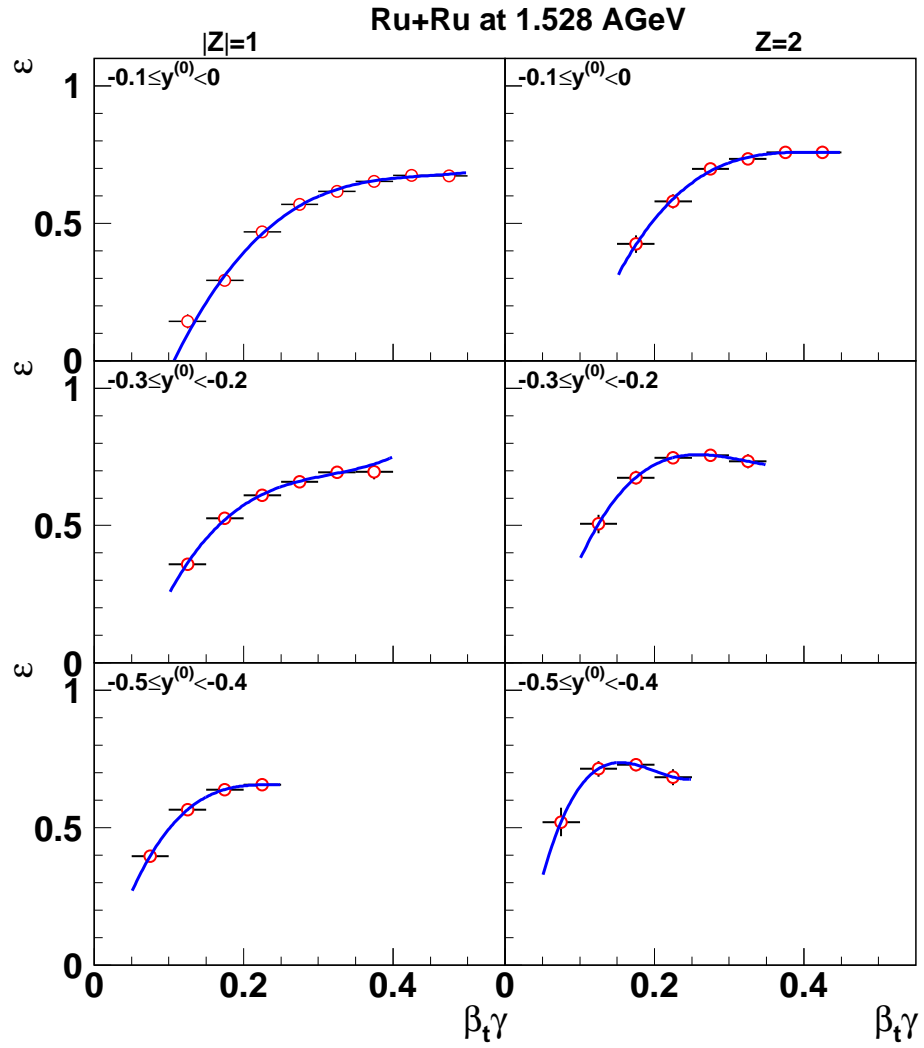


Figure 3.18: Matching efficiencies of the hydrogen (left) and the helium (right) isotopes between the Helitron and the PLAWA as a function of the $\beta_t \gamma$ in Ru+Ru collisions at 1.528 AGeV. The data are fitted by the 4th-order polynomial functions.



and $y^{(0)}$, which are about 70 ~ 80 % and 60 ~ 70 % at 0.4 and 1.528 AGeV, respectively.

3.6.3 CDC track efficiency

The CDC track efficiency has been calculated by using the IQMD model as an event generator with the GEANT detector simulation. The GEANT takes into account the geometrical acceptance and materials of the CDC. The CDC-GEANT package [41] provides us the response information when the particles pass through the CDC. The CDC track efficiency is defined as the ratio of the detected tracks by the CDC-GEANT package to the generated tracks from the IQMD. The efficiency of the deuteron is assumed to be the same for heavier fragments.

The CDC track efficiencies of the proton (left) and deuteron (right) as a function of p_t in Ru+Ru collisions at 0.4 AGeV are shown in figure 3.20. In figure 3.21, the CDC track efficiencies of the proton (left) and deuteron (right) as a function of p_t are presented in Ru+Ru collisions at 1.528 AGeV. The track efficiencies are fitted by the linear function (thick solid line) in the proper p_t region where the particles can be identified. The fitted linear functions are extended to the higher p_t region (thin solid lines).

In 0.4 AGeV, the track efficiencies depend slightly on p_t in general. But the efficiencies in the target region ($-1.1 \leq y^{(0)} < -0.9$) show the strongest dependence on p_t . It reflects the fact that the relatively low momentum particles in the target rapidity suffer the strong target absorption effect. In $-1.6 \leq y^{(0)} < -1.1$ (bottom), the efficiencies are higher than those of the target region but the target absorption effect does not disappear completely.

In 1.528 AGeV, the track efficiencies depend slightly on p_t in $-0.9 \leq y^{(0)} < -0.1$ (top). The efficiencies of the proton and the deuteron are ~ 70 and $\sim 90\%$ respectively at about 1 GeV/ c . The efficiencies in target region ($-1.1 \leq y^{(0)} < -0.9$) are reduced somewhat due to the target absorption.



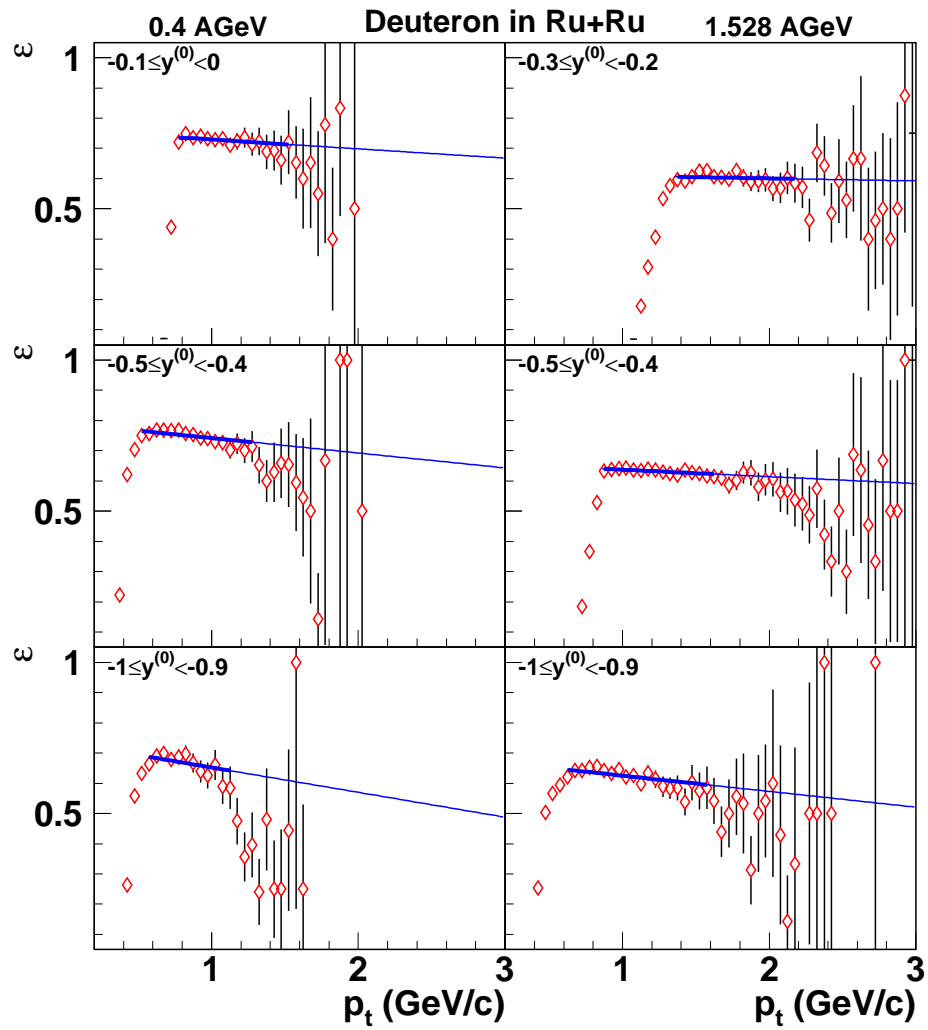


Figure 3.19: Matching efficiencies between the CDC and Barrel as a function of p_t in Ru+Ru collisions at 0.4 (left) and 1.528 (right) AGeV. The matching efficiencies are fitted by the linear functions (solid lines).



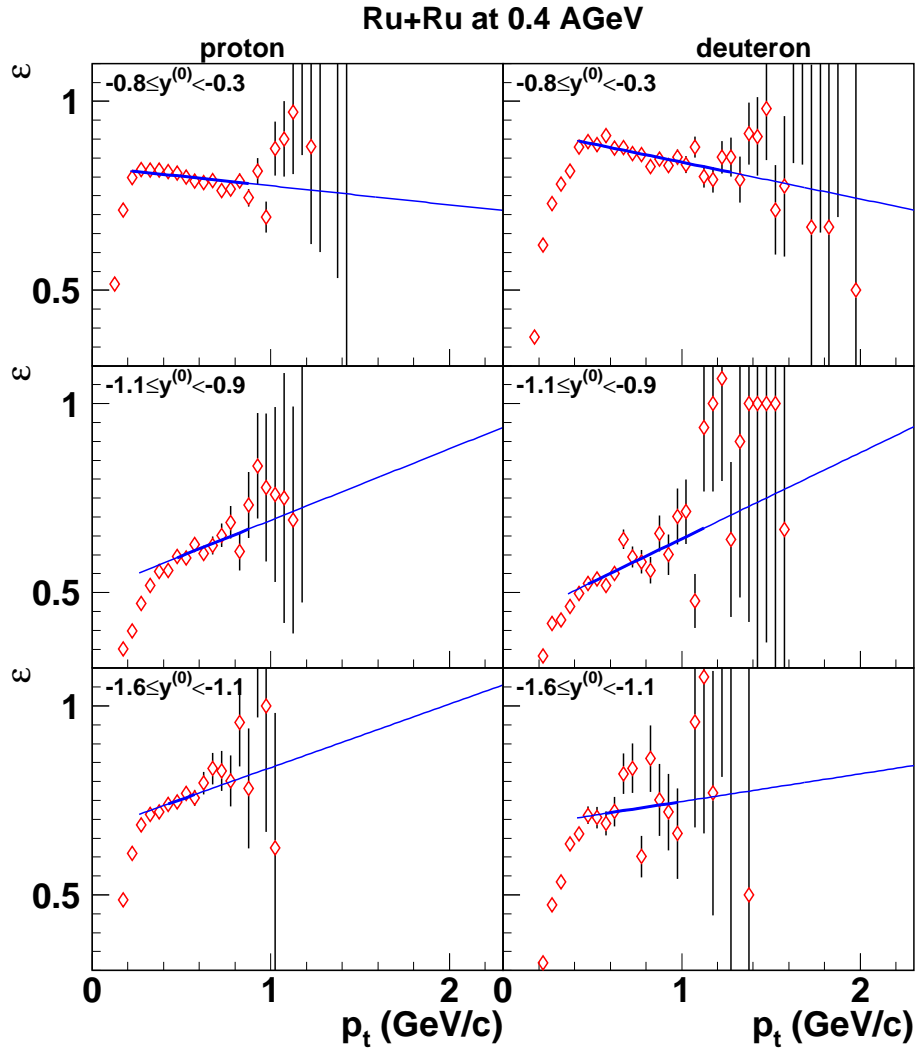


Figure 3.20: CDC track efficiencies as a function of p_t calculated by the IQMD simulation in Ru+Ru collisions at 0.4 AGeV. The track efficiencies are fitted by the linear function (thick solid line) in the proper p_t region where the particles can be identified. The linear functions are extended to the higher p_t region (thin solid lines).



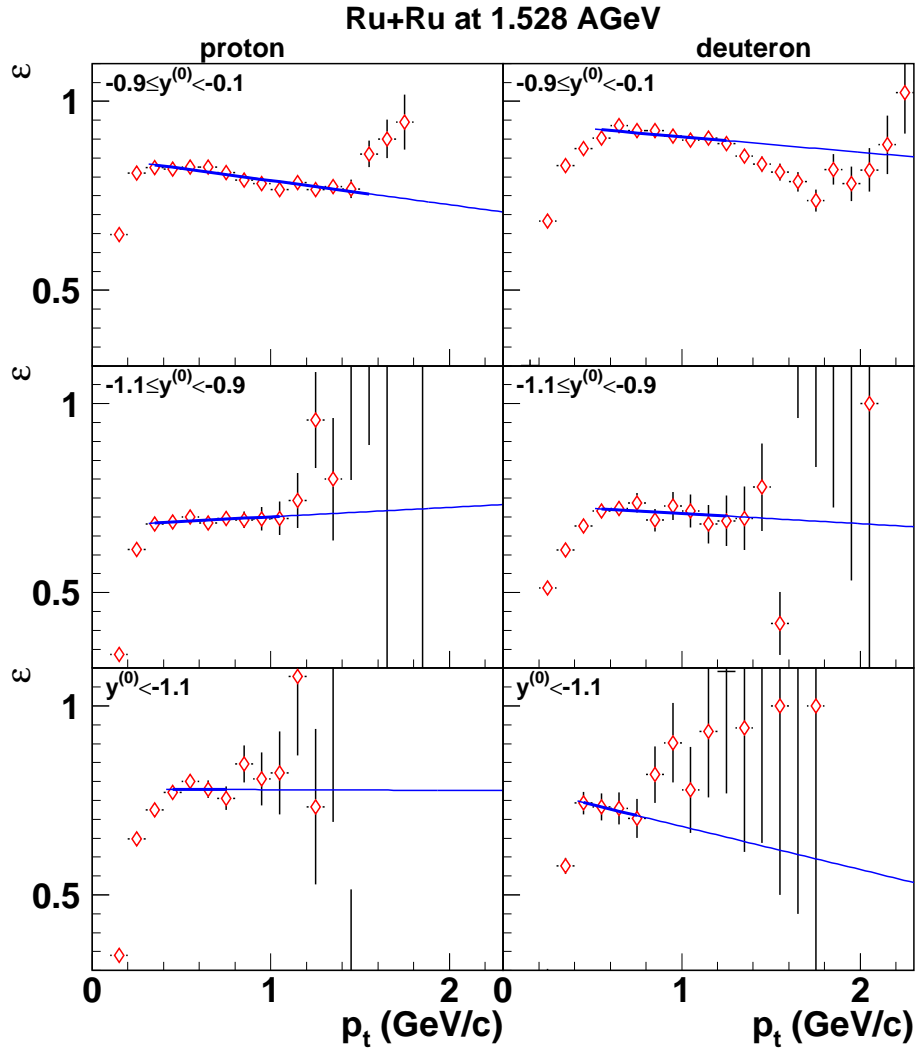


Figure 3.21: CDC track efficiencies as a function of p_t calculated by the IQMD simulation in Ru+Ru collisions at 1.528 AGeV. The track efficiencies are fitted by the linear function (thick solid line) in the proper p_t region where the particles can be identified. The linear functions are extended to the higher p_t region (thin solid lines).



3.7 Phase space distribution

The phase-space distributions of the hydrogen and the helium isotopes in Ru+Ru collisions at 0.4 (left) and 1.528 (right) AGeV are shown in figures 3.22 and 3.23, respectively.

The phase-space distributions are presented by the normalized transverse momentum ($p_t^{(0)}$) versus the normalized rapidity ($y^{(0)}$):

$$p_t^{(0)} = \frac{p_t}{m\beta_{cm}\gamma_{cm}} \quad (3.6)$$

where β_{cm} and γ_{cm} are velocity and Lorentz gamma factor of the CM frame.

$$y^{(0)} = \frac{y_{lab}}{y_{cm}} - 1 \quad (3.7)$$

where y_{cm} is the rapidity in center-of-mass (CM) frame.

All kinds of the efficiencies discussed previously are corrected for the phase-space distributions. The geometrical limits of the sub-detectors are drawn by the solid lines. The phase-space distributions of the proton (top) and deuteron (middle) are from the CDC and the Helitron (HEL). On the other hand, the distributions for ^3H , ^3He , and ^4He are from the Barrel (BAR) and the Helitron. For 1.528 AGeV, the additional velocity cut at $0.8c$ (dashed line) are drawn for rejecting the ambiguous PID region.



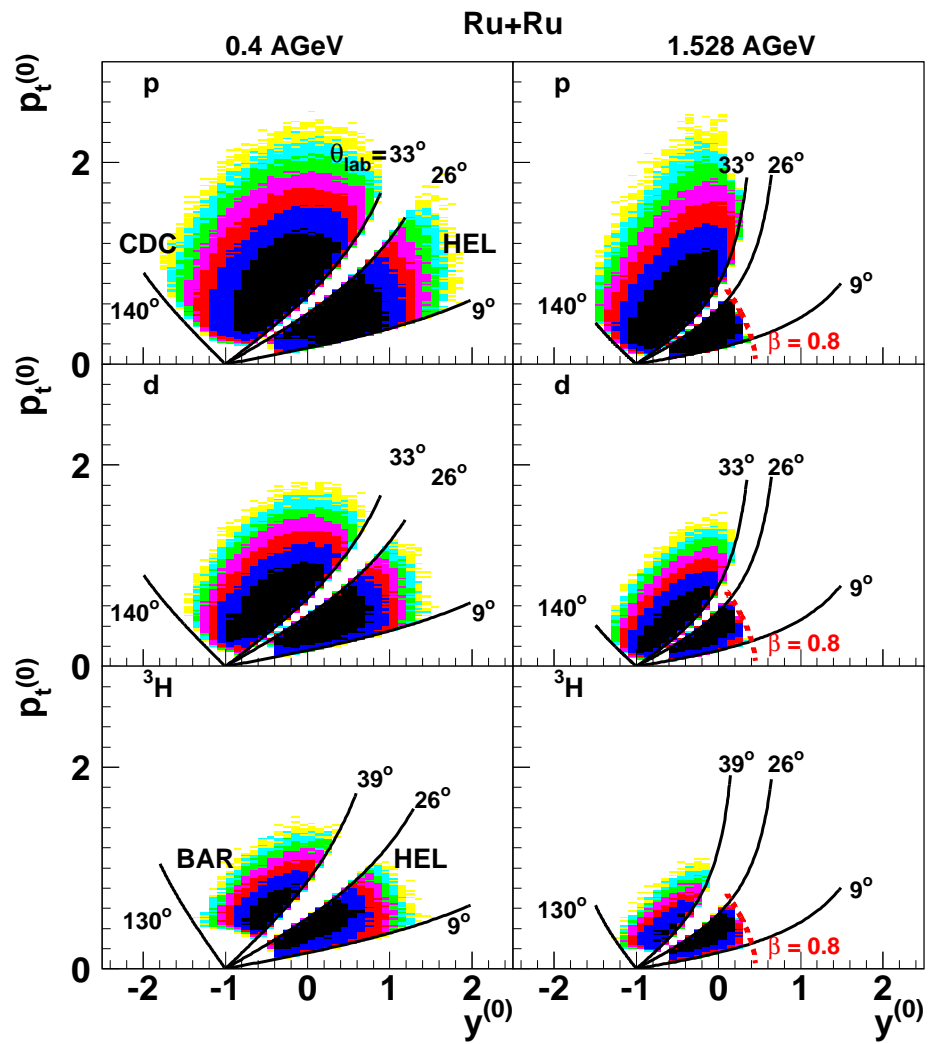


Figure 3.22: Phase-space distributions of the the hydrogen isotope in Ru+Ru collisions at 0.4 (left) and 1.528 (right) AGeV.



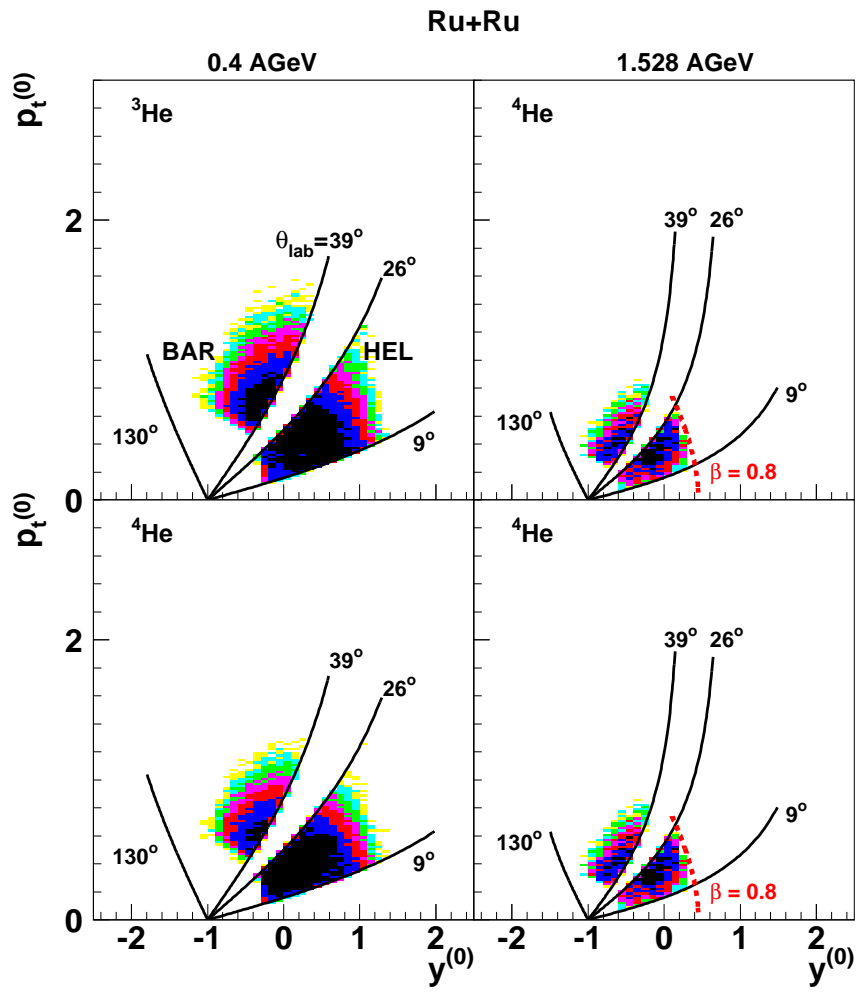


Figure 3.23: Phase-space distributions of the helium isotope in Ru+Ru collisions at 0.4 (left) and 1.528 (right) AGeV.



3.8 Reaction plane reconstruction

The collective motion of the emitting particles in heavy-ion collisions has been studied in order to understand the properties of the nuclear matter. The particle distributions have been analyzed relative to the reaction plane which is defined by the impact parameter (\vec{b}) and beam direction (\vec{z}). The x -direction is defined as the impact parameter direction in the reaction plane.

The azimuthal angle of the reaction plane has been reconstructed by using the trasverse momentum method proposed by Danielewicz and Odyniec [25]. The orientation of reaction plane (ϕ_{RP}) is calculated by summing the transverse momenta of all particles for a given event i except the particles near mid-rapidity:

$$\vec{Q}^i = \begin{pmatrix} Q^i \cdot \cos \phi_{RP} \\ Q^i \cdot \sin \phi_{RP} \end{pmatrix} = \sum_{k=1}^N w_k \cdot |\vec{p}_t^i| \cdot \begin{pmatrix} \cos \phi_k \\ \sin \phi_k \end{pmatrix} \quad (3.8)$$

where ϕ_k is the azimuthal angle of the particle k , $w_k = -1$ for $y^{(0)} \leq -0.2$, and $w_k = +1$ for $y^{(0)} \geq +0.2$. Here N is the total number of particles and \vec{Q}^i is the total tranverse momentum of the particle in an event.

The identified hydrogen and helium isotopes in figures 3.22 and 3.23 are used to reconstruct the reaction plane. The azimuthal angle distribution of the reaction plane (ϕ_{RP}) and the resolution ($\Delta\phi_{RP}$) are shown in the top and the middle pannels, respectively, of figure 3.24. And the width $\sigma_{\Delta\phi}$ are plotted as a function of the impact parameter in the bottom pannels of figure 3.24. The fluctuation of the azimuthal angle distribution is less than 10 %. The quality of the reconstructed reaction plane has been estimated by the method introduced in [25]: an event is randomly divided into two sub-events containing half of the particles, and, then, two independent estimation of the azimuthal angle (ϕ_1 and ϕ_2) of the reaction plane were subtracted. The resolution of the reaction plane can be obtained by fitting the angle difference distributions ($\Delta\phi_{RP} = \phi_1 - \phi_2$) by the Gaussian function with a constant offset. The resolutions of the reaction planes are 34° and 42° at 0.4 and 1.528 AGeV, respectively. The resolution of the reaction plane has the dependence on the collision centrality as shown in the bottom plot of figure 3.24. As



expected, the best resolutions were obtained for the semicentral collisions at both beam energies.

The direction of the reconstructed reaction plane will differ from the true reaction plane due to the fluctuations in measured particle multiplicity and transverse momentum resolution of the detector. The Fourier coefficients (v_n) were corrected by $\langle \cos n\Delta\phi \rangle$ following the Ollitrault's correction method [26], which is described below briefly.

If ψ is the measured azimuthal angle of the particles with respect to the reconstructed reaction plane, ϕ is the azimuthal angle of the particles with respect to the true reaction plane, and $\Delta\phi$ is the difference between the reconstructed and true reaction plane, one can express $\psi = \phi - \Delta\phi$. If many events are used to obtain the average distribution of $\Delta\phi$, one can assume that $\Delta\phi$ and ϕ are independent. According to this assumption, the relation between the measured and the true Fourier coefficients are

$$\langle \cos n\psi \rangle = \langle \cos n\phi \rangle \langle \cos n\Delta\phi \rangle . \quad (3.9)$$

The correction factor $\langle \cos n\Delta\phi \rangle$ for the n -th Fourier coefficient can be obtained from a parameter χ . The relation between $\langle \cos \Delta\phi_{RP} \rangle$ and χ on the top plot in figure 3.25 can be determined in the following equation:

$$\begin{aligned} \langle \cos \Delta\phi_{RP} \rangle &= \langle \cos \phi_1 \rangle \langle \cos \phi_2 \rangle \\ &= \frac{\pi}{8} \chi^2 e^{-\chi^2} \left[I_0 \left(\frac{\chi^2}{4} \right) + I_1 \left(\frac{\chi^2}{4} \right) \right]^2 , \end{aligned} \quad (3.10)$$

where I_0 and I_1 are the modified Bessel functions. For the n -th correction factor ($\langle \cos n\Delta\phi \rangle$) on the bottom plot in figure 3.25 one finds

$$\langle \cos n\Delta\phi \rangle = \frac{\sqrt{\pi}}{2} \chi e^{-\chi^2/2} \left[I_{\frac{n-1}{2}} \left(\frac{\chi^2}{2} \right) + I_{\frac{n+1}{2}} \left(\frac{\chi^2}{2} \right) \right] . \quad (3.11)$$

The correction factors for $n=1$ and $n=2$ are provided the solid and dashed lines, respectively, at the bottom plot in figure 3.25, and they are also summarized in table 3.4 for each centrality selection.



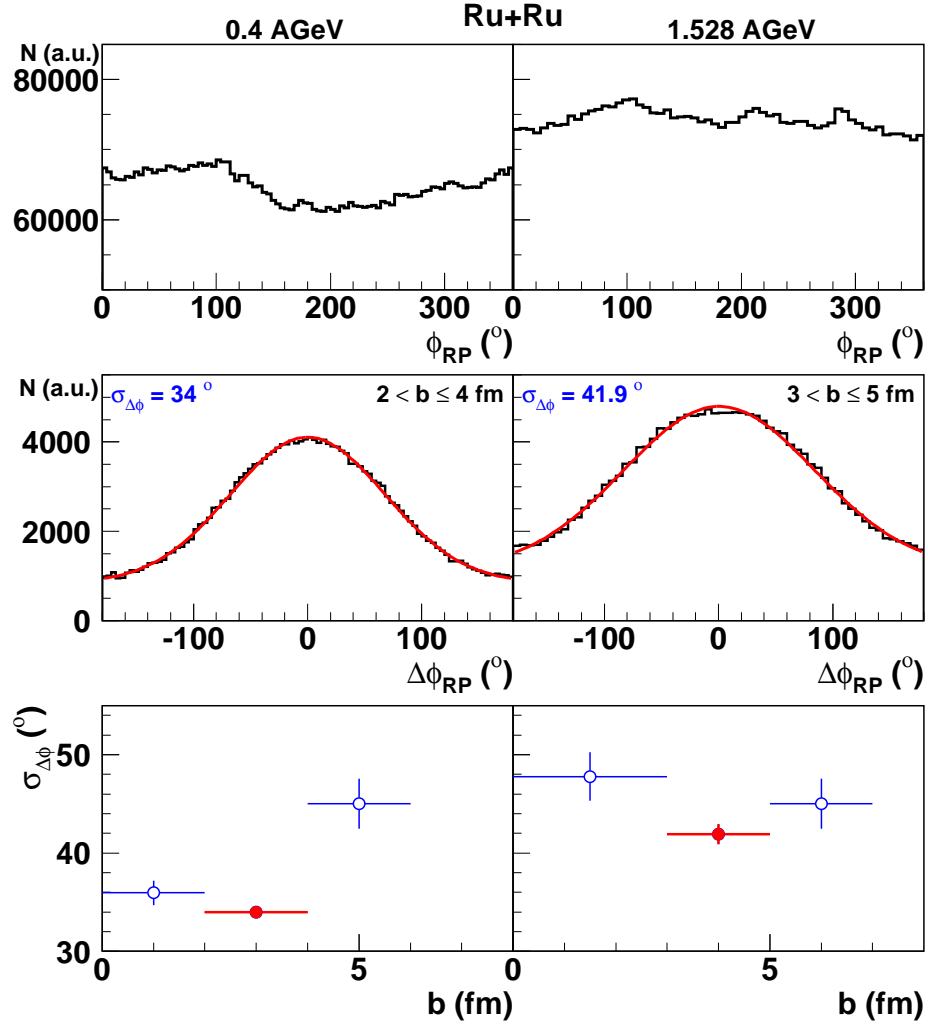


Figure 3.24: Azimuthal angle distribution (ϕ_{RP} on top) and the azimuthal distribution of the reaction plane ($\Delta\phi_{RP}$ on middle) and the reaction plane resolution ($\sigma_{\Delta\phi}$ on bottom) in Ru+Ru collisions at 0.4 (left) and 1.528 (right) AGeV.



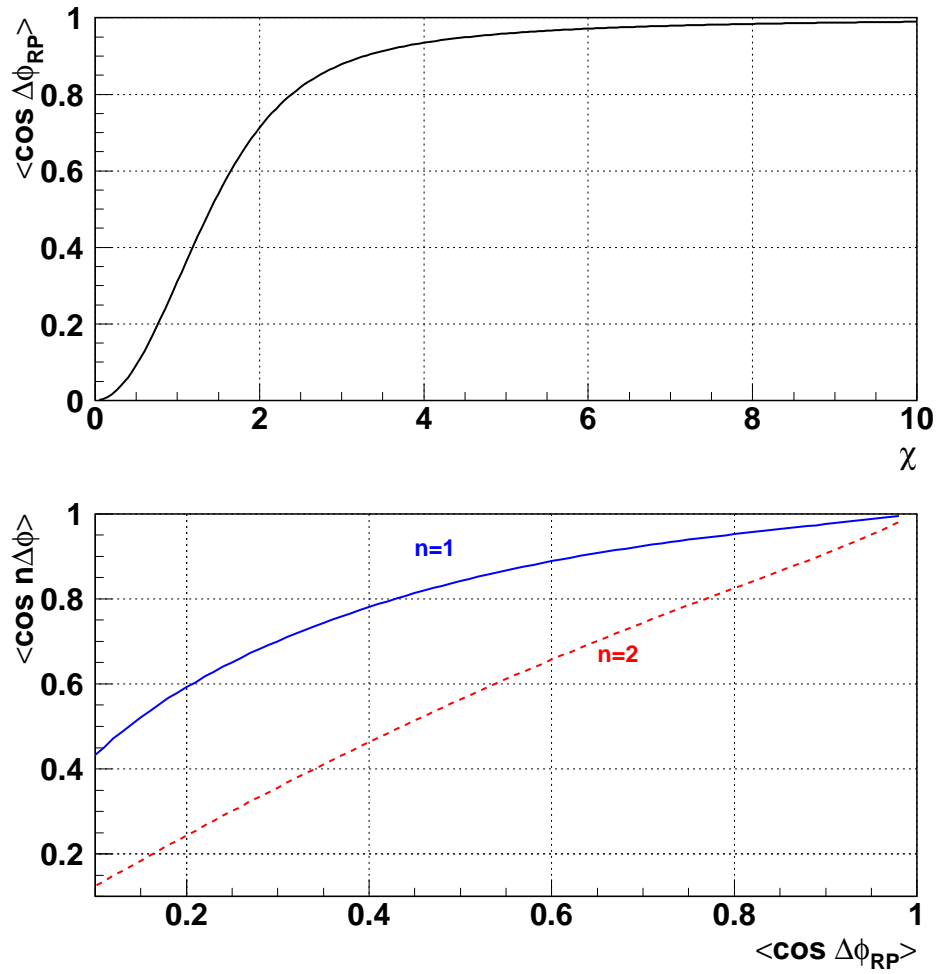


Figure 3.25: Correction factors for the Fourier coefficients (v_n) by using O-litrault correction [26]. The relations between $\langle \cos \Delta\phi_{RP} \rangle$ and χ and $\langle \cos n\Delta\phi \rangle$ and $\langle \cos \Delta\phi_{RP} \rangle$ are presented on the top and bottom plots, respectively. The correction factors for $n=1$ and $n=2$ are provided by solid and dashed lines, respectively.



v_n	E_{beam}	Centrality	correction factor
v_1	0.4	TMUL02	0.623
		TMUL24	0.723
		TMUL46	0.691
	1.528	TMUL03	0.465
		TMUL35	0.642
		TMUL57	0.595
v_2	0.4	TMUL02	0.272
		TMUL24	0.384
		TMUL46	0.345
	1.528	TMUL03	0.145
		TMUL35	0.292
		TMUL57	0.246

Table 3.4: Correction factors of the Fourier coefficients (v_n) for central (TMUL02, TMUL03), semicentral (TMUL24, TMUL35), and peripheral (TMUL46, TMUL57) collision events in Ru+Ru collisions.



Chapter 4

Part I : Results and Discussions

4.1 Kinematic distributions of the proton and light fragments

For the most central collisions, the invariant transverse momentum spectra and the rapidity distributions of the hydrogen and helium isotopes have been obtained in Ru+Ru collisions at 0.4 and 1.528 AGeV. The radial flow velocity and temperature have been estimated and compared to the other published results.

4.1.1 Invariant spectra

For the most central collisions, the invariant transverse momentum spectra of the hydrogen and helium fragments are shown in figures 4.1 and 4.2, respectively, in Ru+Ru collisions at 0.4 AGeV. In figures 4.3 and 4.4, the invariant transverse momentum spectra of the hydrogen and helium frag-



ments in Ru+Ru collisions at 1.528 AGeV are provided. The $PLA(B)$ (circles) and $PLA(F)$ (diamonds) imply the matched data between the Helitron and PLAWA in backward and forward rapidity regions in the center-of-mass system, respectively. For the proton and deuteron, the $CDC(B)$ (squares) and $CDC(F)$ (triangles) denote the CDC data in backward and forward rapidity regions in the center-of-mass system, respectively. For the ${}^3\text{H}$, ${}^3\text{He}$, and ${}^4\text{He}$, the $CDC(B)$ (squares) and $CDC(F)$ (triangles) mean the matched data sets between the CDC and Barrel in backward and forward rapidity regions in the center-of-mass system, respectively.

Starting with the next to the mid-rapidity bin, each spectrum is multiplied by a decreasing order of 10 for a clearer display. The spectra of the proton and deuteron have been corrected by the matching efficiency for forward (Helitron and PLAWA) and the CDC track efficiency for the backward rapidity region. The spectra of the ${}^3\text{H}$, ${}^3\text{He}$, and ${}^4\text{He}$ have been corrected by the matching efficiencies for forward (Helitron and PLAWA) and backward (CDC and Barrel) rapidity region.

In the Ru+Ru collision system, one can expect the symmetry between the forward (F) and backward (B) rapidity regions in the center-of-mass system. The invariant spectra at 0.4 AGeV show good agreements. But at 1.528 AGeV, only the spectra in the backward region are used due to the finite detector performance in the forward region [43]. And the spectra of the light fragments (d , ${}^3\text{H}$, ${}^3\text{He}$, and ${}^4\text{He}$) at the mid-rapidity region could not be used due to the unclear PID.

In order to make up the missing p_t ranges which is due to the finite detector acceptance, the spectra in a given rapidity region have been fitted by the simple thermal blast formula proposed by Siemens and Rasmussen [48]:

$$\frac{1}{2\pi p_t} \frac{d^2N}{dp_t dy^{(0)}} = C \cdot E \exp(-\gamma_r E/T) \cdot \left[\left(\gamma_r + \frac{T}{E} \right) \frac{\sinh \alpha}{\alpha} - \frac{T}{E} \cosh \alpha \right] \quad (4.1)$$

where α is defined as $(\gamma_r \cdot \beta_r \cdot p)/T$ with $\gamma_r = 1/\sqrt{1 - \beta_r^2}$. Here the constant C , radial flow velocity (β_r), and thermal freeze-out temperature (T) are free fitting parameters. And E and p are the total energy and momentum of the particle in the center-of-mass system.



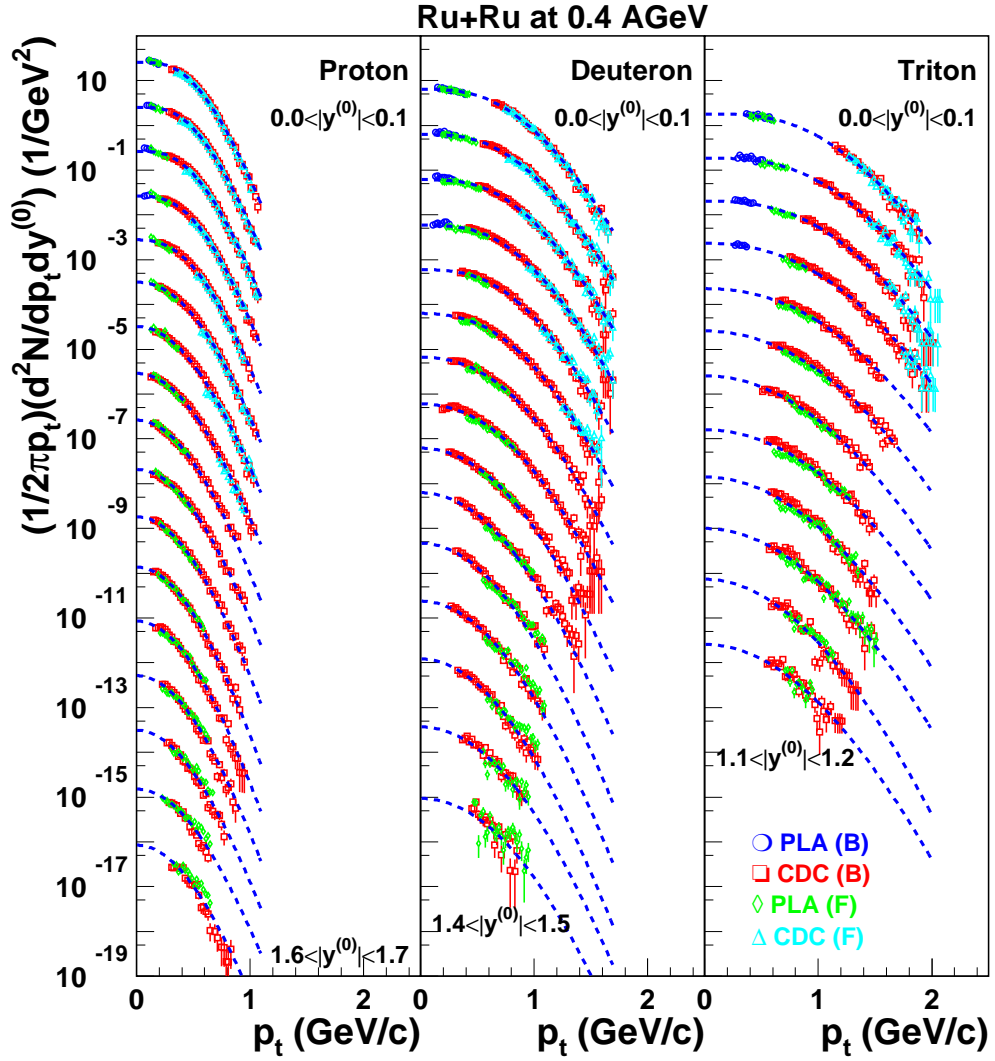


Figure 4.1: Invariant spectra of the hydrogen isotopes in Ru+Ru collisions at 0.4 AGeV. The dashed lines are the fit functions by the simple thermal blast formula, equation 4.1, with three free fitting parameters (C , β_r , and T). The detail explanation is given in the text.



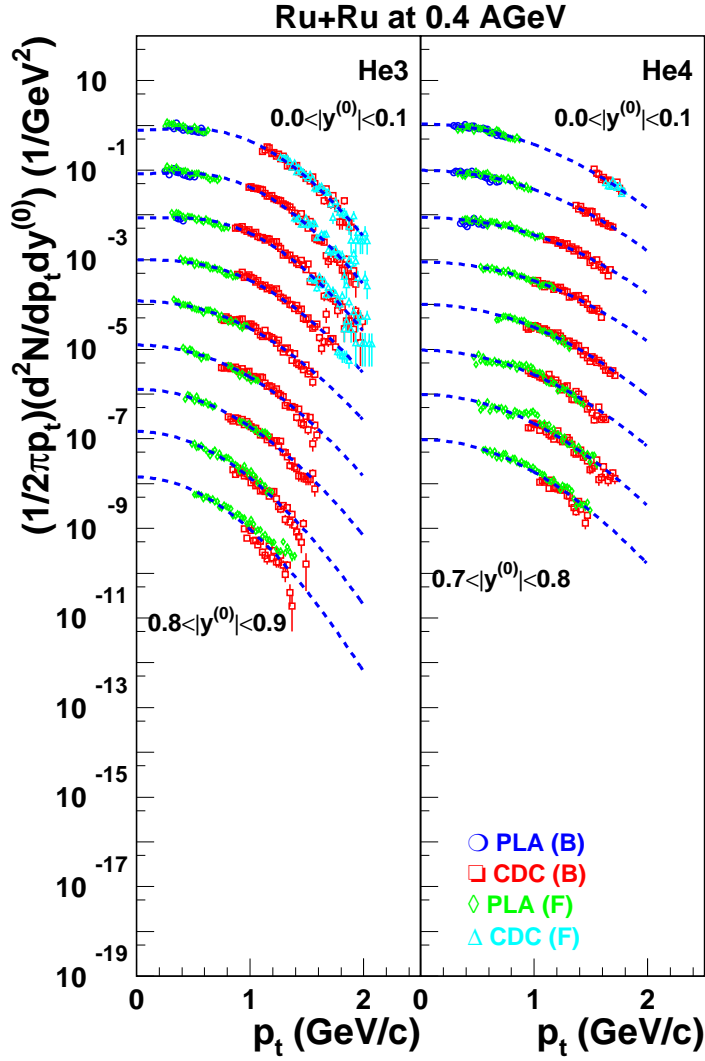


Figure 4.2: Invariant spectra of the helium isotopes in Ru+Ru collisions at 0.4 AGeV. The dashed lines are the fit functions by the simple thermal blast formula, equation 4.1, with three free fitting parameters (C , β_r , and T). The detail explanation is given in the text.



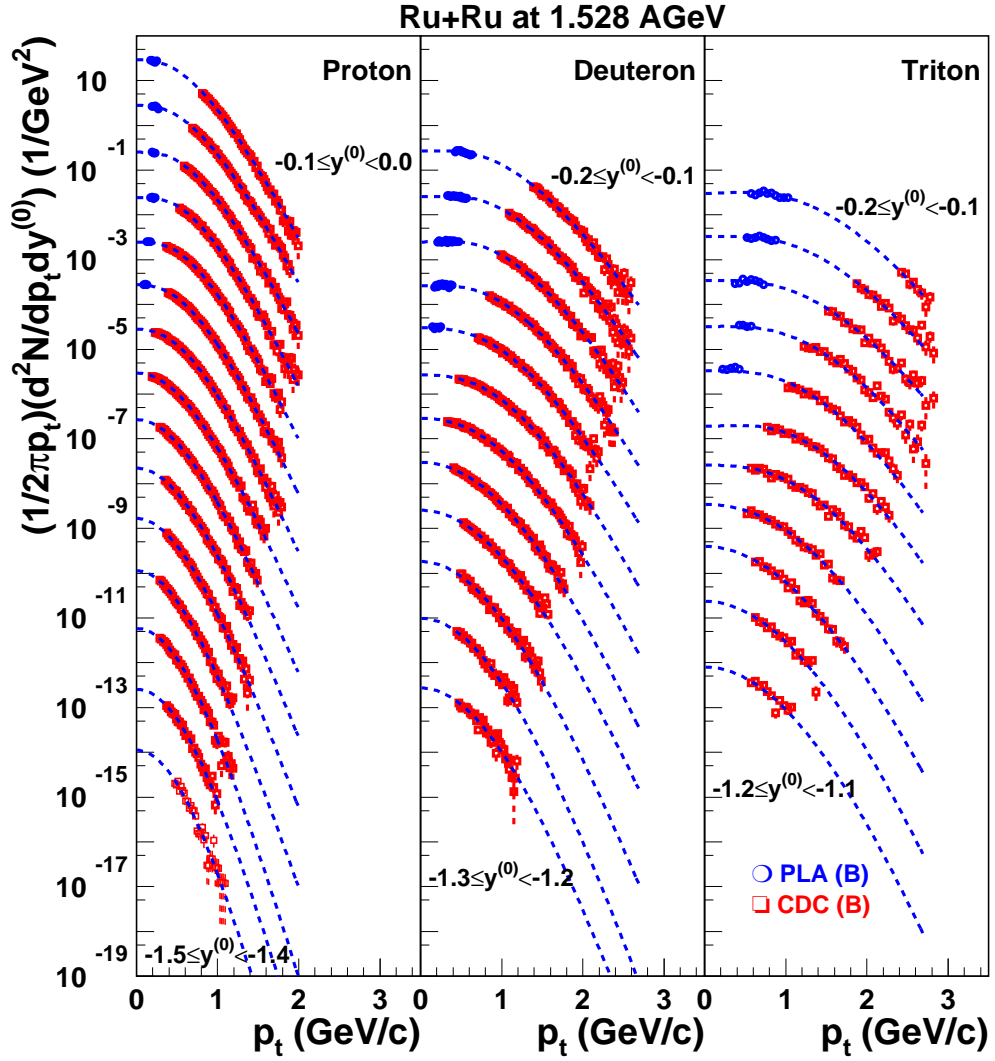


Figure 4.3: Invariant spectra of the hydrogen isotopes in Ru+Ru collisions at 1.528 AGeV. The dashed lines are the fit functions by the simple thermal blast formula, equation 4.1, with three free fitting parameters (C , β_r , and T). The detail explanation is given in the text.



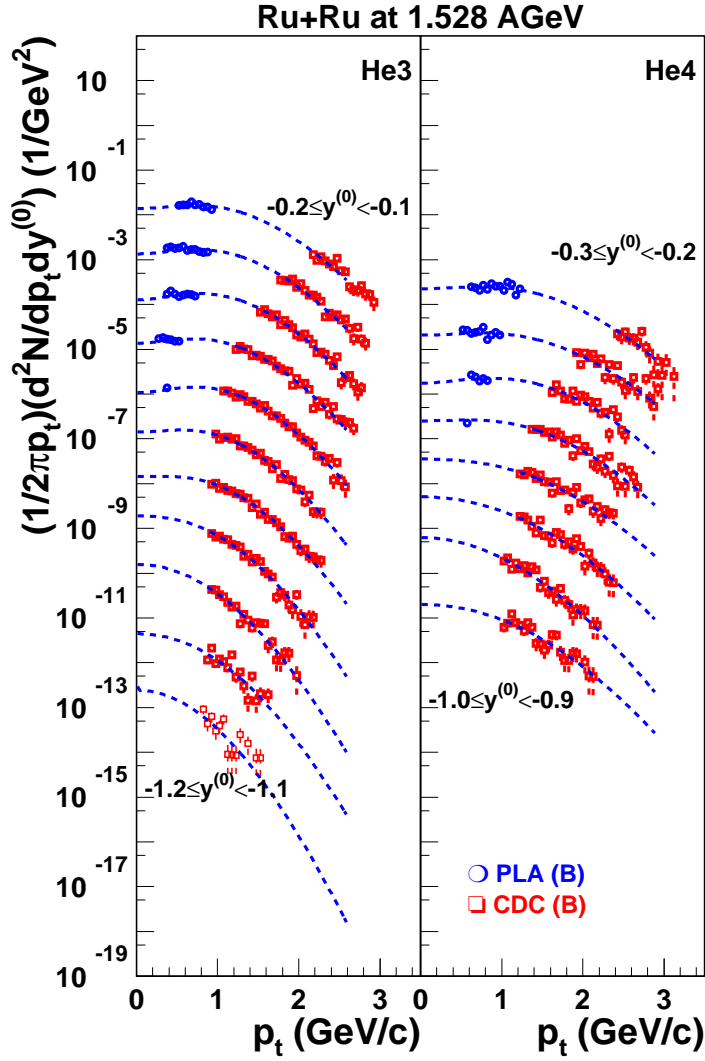


Figure 4.4: Invariant spectra of the helium isotopes in Ru+Ru collisions at 1.528 AGeV. The dashed lines are the fit functions by the simple thermal blast formula, equation 4.1, with three free fitting parameters (C , β_r , and T). The detail explanation is given in the text.



4.1.2 Rapidity spectra

The missing p_t ranges were covered by means of the fitted simple thermal blast formula. By integrating the fit functions for a given rapidity bin, the $dN/dy^{(0)}$ of the particles can be determined. The rapidity distributions of the hydrogen (top) and helium (bottom) isotopes for the most central Ru+Ru collisions at 0.4 (left) and 1.528 (right) AGeV are shown in figure 4.5. The proton (circles), deuteron (squares), ^3H (triangles), ^3He (diamonds), and ^4He (stars) are plotted.

For 0.4 AGeV, the rapidity distributions of ^3He and ^4He are very close so that the ^4He data have been scaled by 0.5 for a clear display. Note that in order to get the $dN/dy^{(0)}$ data near the target and beam rapidity regions at 0.4 AGeV, the measured rapidity distributions of the helium isotopes are fitted by the quadratic functions. The total production yields are obtained by integrating the quadratic function. The results are summarized in table 4.1.

On the other hand, for 1.528 AGeV, the mid-rapidity yields other than protons are missing. Therefore, we fit the measured spectra by the quadratic equation to estimate the mid-rapidity yields. The total yields at 1.528 AGeV are also summarized in table 4.1.

4.1.3 Radial flow velocity and temperature

In order to understand the properties of the expanding nuclear matter in heavy-ion collisions, one needs to estimate the mean radial flow velocity, $\langle\beta_r\rangle$, and temperature, T , and the inverse slope parameter T_B from the Boltzmann-like distribution. Originally, the simple thermal blast model was used for the spherical coordinates. But the rapidity spectra are not isotropic, we limit the application of the model only to the mid-rapidity data. As a result, the radial flow velocity corresponds to the transversal flow velocity. In this analysis, the free fitting parameters of the simple thermal blast formula have been used to understand the expansion dynamics as explained in the next paragraphs.



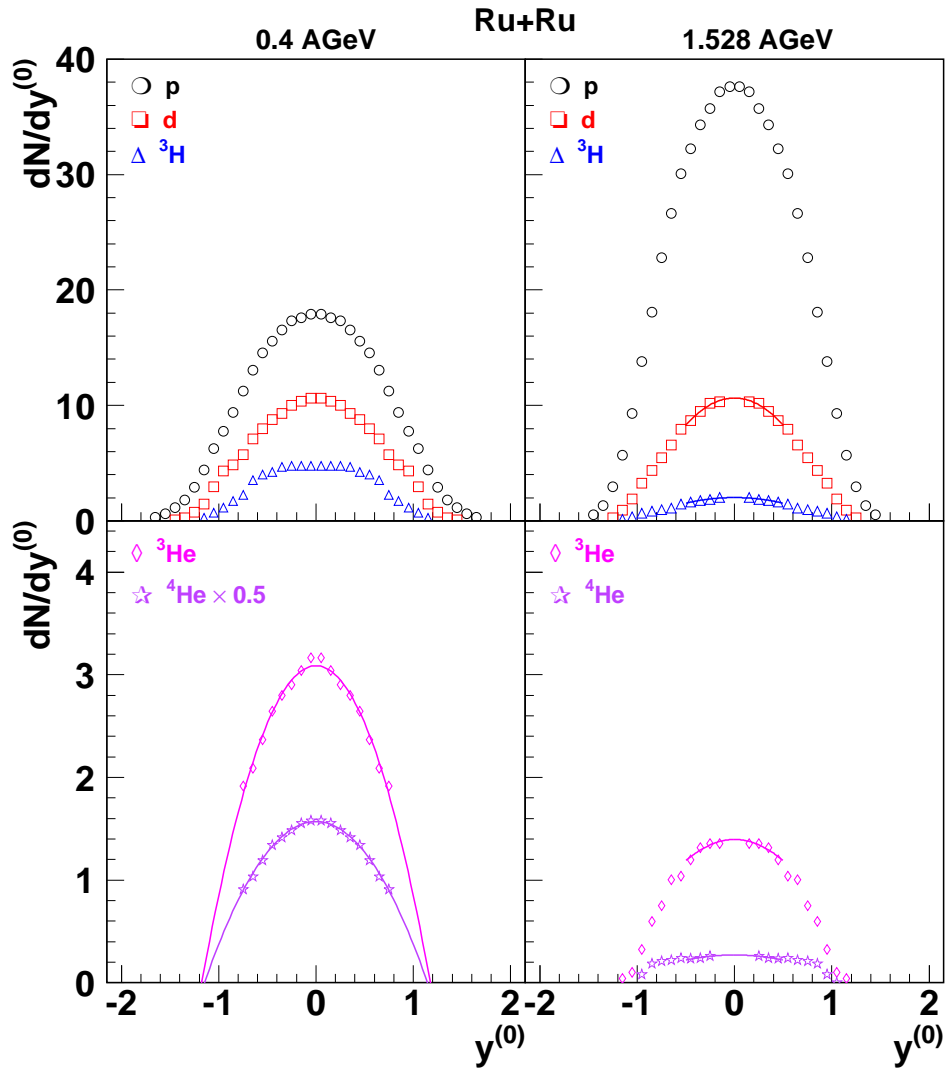


Figure 4.5: Rapidity distributions of the hydrogen (top) and helium (bottom) isotopes for the most central Ru+Ru collisions at 0.4 (left) and 1.528 (right) AGeV. The proton (circles), deuteron (squares), ${}^3\text{H}$ (triangles), ${}^3\text{He}$ (diamonds), and ${}^4\text{He}$ (stars) are drawn.



E_{beam} (AGeV)	σ_{geo} (mb)	Particle type	Total yield	Sys. err. (%)
0.4	102	p	31.7	5
		d	16.9	8
		^3H	7.4	11
		^3He	4.8	14
		^4He	4.8	11
1.528	95	p	61.6	5
		d	16.1	12
		^3H	3.0	27
		^3He	2.1	20
		^4He	0.4	34

Table 4.1: Total production yields of the particles for the most central Ru+Ru collisions at 0.4 and 1.528 AGeV. The details of the systematic error estimates will be explained in details in section 4.1.4.

If the thermal equilibrium is achieved locally in the non-relativistic limit, the thermal energy should be $(3/2)T$. The relation between the total flow (E_F), the thermal (E_T), and the mean kinetic ($\langle E_{kin} \rangle$) energy of the expanding source can be described as [49]

$$\langle E_{kin} \rangle = E_F \cdot A + E_T = \frac{1}{2}m_0 \langle \beta_r \rangle^2 \cdot A + \frac{3}{2}T, \quad (4.2)$$

where m_0 is the nucleon rest mass and A is the mass number of the particle. According to equation 4.2, the $\langle E_{kin} \rangle$ of the system for the most central Ru+Ru collisions can be obtained from β_r and T , which are free fitting parameters, to the invariant spectra.

At the mid-rapidity, $\langle E_{kin} \rangle$ of all particles can be calculated at 0.4 AGeV, but $\langle E_{kin} \rangle$ of the light fragments can not be derived directly from the experimental data at 1.528 AGeV because the data are missing. Therefore, in order to get $\langle E_{kin} \rangle$ of the light fragments at 1.528 AGeV, the distributions of $\langle E_{kin} \rangle$ at other than midrapidities are fitted by the 4-th order of polynomial function. Then, the $\langle E_{kin} \rangle$ values at the mid-rapidity are conjectured and plotted as a function of the mass of particle shown in figure 4.7. The



proton (circles), deuteron (squares), ^3H (triangles), ^3He (diamonds), and ^4He (stars) are drawn for 0.4 (top) and 1.528 (bottom) AGeV in figure 4.7. The mean kinetic energies have been fitted by the linear equation for the energy relation given in equation 4.2. From that the mean radial flow velocity and temperature at the midrapidity region are determined in figure 4.7.

In figure 4.8, $\langle \beta_r \rangle$ and T are compared to the other published results as a function of the beam energy. The closed star symbols are from this analysis for the most central Ru+Ru collisions at 0.4 and 1.528 AGeV. The open circles are the results from the EOS experiment [50] and other results are from the FOPI experiment [15, 47, 49].

4.1.4 Systematic errors

The systematic errors of the data were estimated by the following considerations.

- Centrality selection dependence, compared the results obtained by the total multiplicity and those by the ratio of the total transverse to longitudinal kinetic energies (E_{rat}).
- Matching condition method dependence between the tracker (CDC or Helitron) and time-of-flight (Barrel or PLAWA).
- Charge separation at dependence between the hydrogen and the helium isotopes.
- Particle Identification method dependence in the mass distribution.
- Uncertainty of the estimated matching efficiencies between the tracker and time-of-flight.
- Uncertainty of the CDC track efficiencies estimated by the IQMD simulation.
- Discrepancy of the transverse momentum spectra between the backward and forward regions.



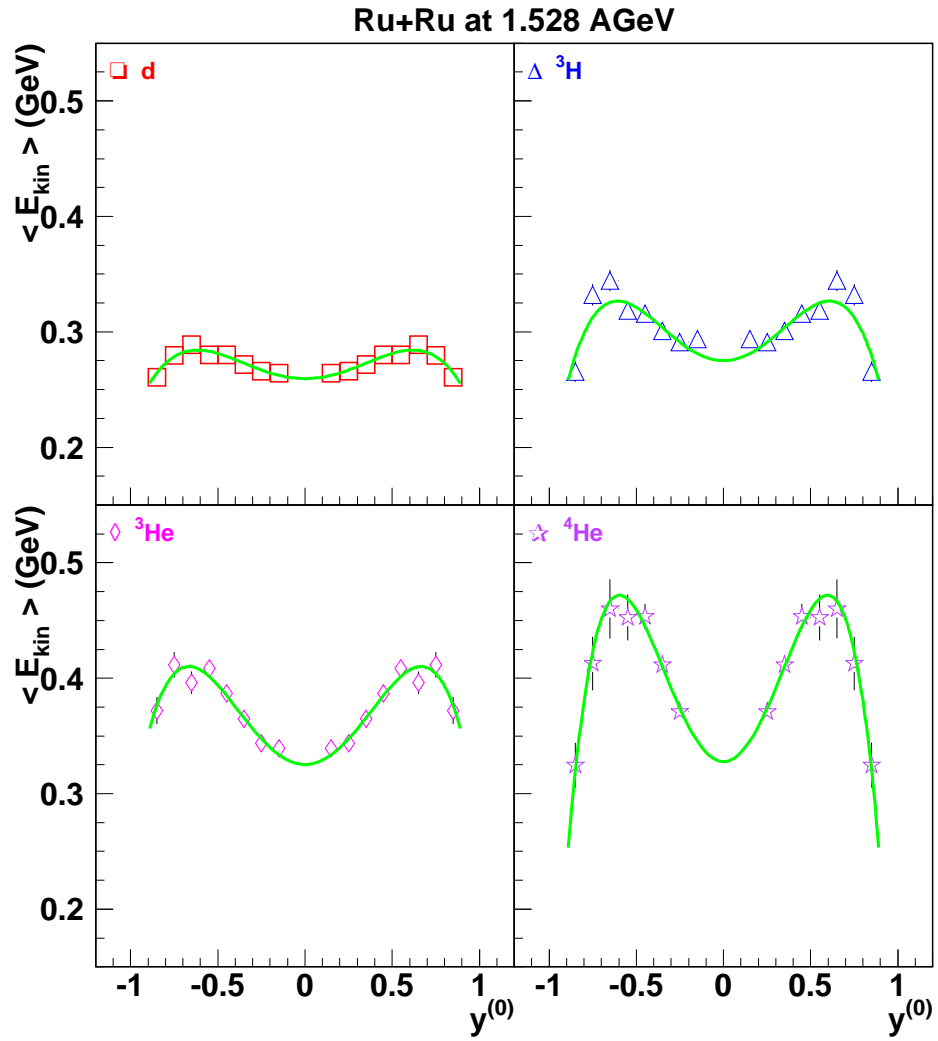


Figure 4.6: Mean kinetic energy distributions of the light fragments (d , ${}^3\text{H}$, ${}^3\text{He}$, and ${}^4\text{He}$) for the most central Ru+Ru collisions at 1.528 AGeV. The solid lines are the fits by the 4th-order polynomial function.



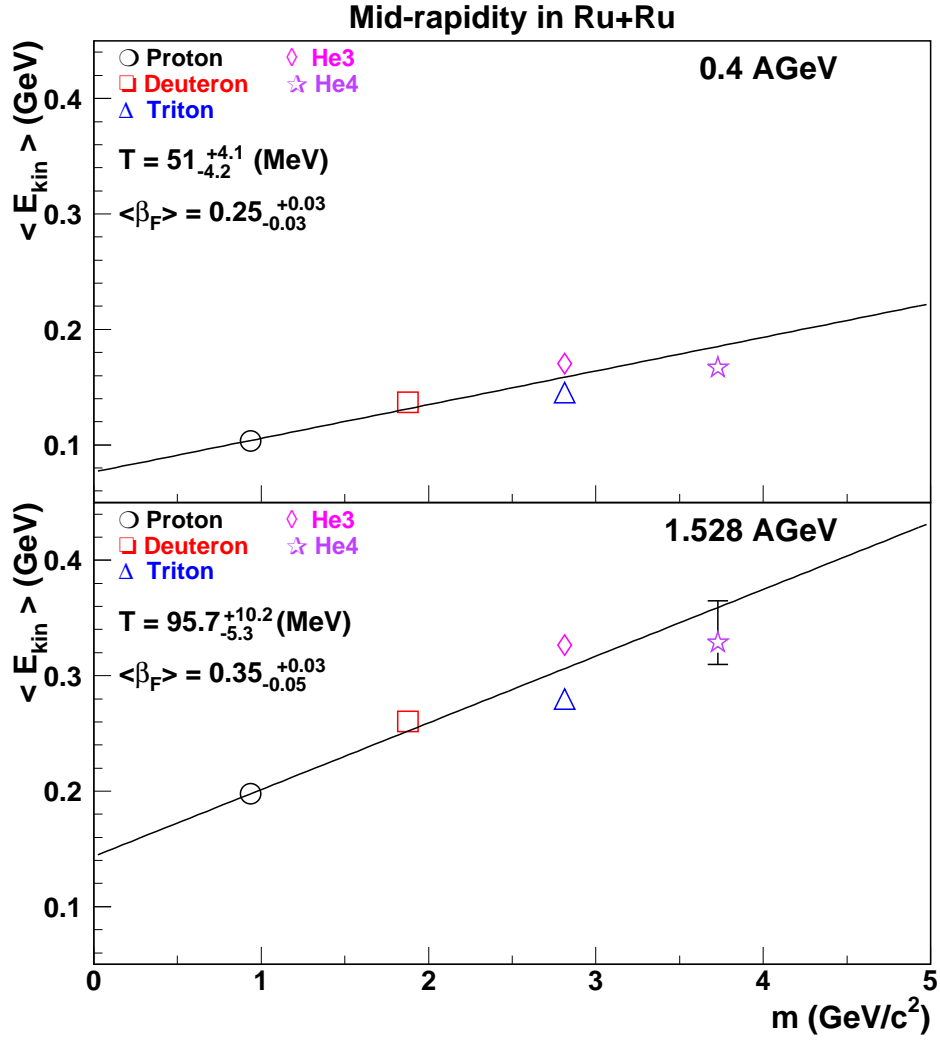


Figure 4.7: Mean kinetic energies of the light fragments (d , ${}^3\text{H}$, ${}^3\text{He}$, and ${}^4\text{He}$) as a function of the particle mass for the most central Ru+Ru collisions at 0.4 (top) and 1.528 (bottom) AGeV. In order to obtain the mean radial flow velocity and the temperature, the mean kinetic energies have been fitted by the linear equation as shown in equation 4.2.



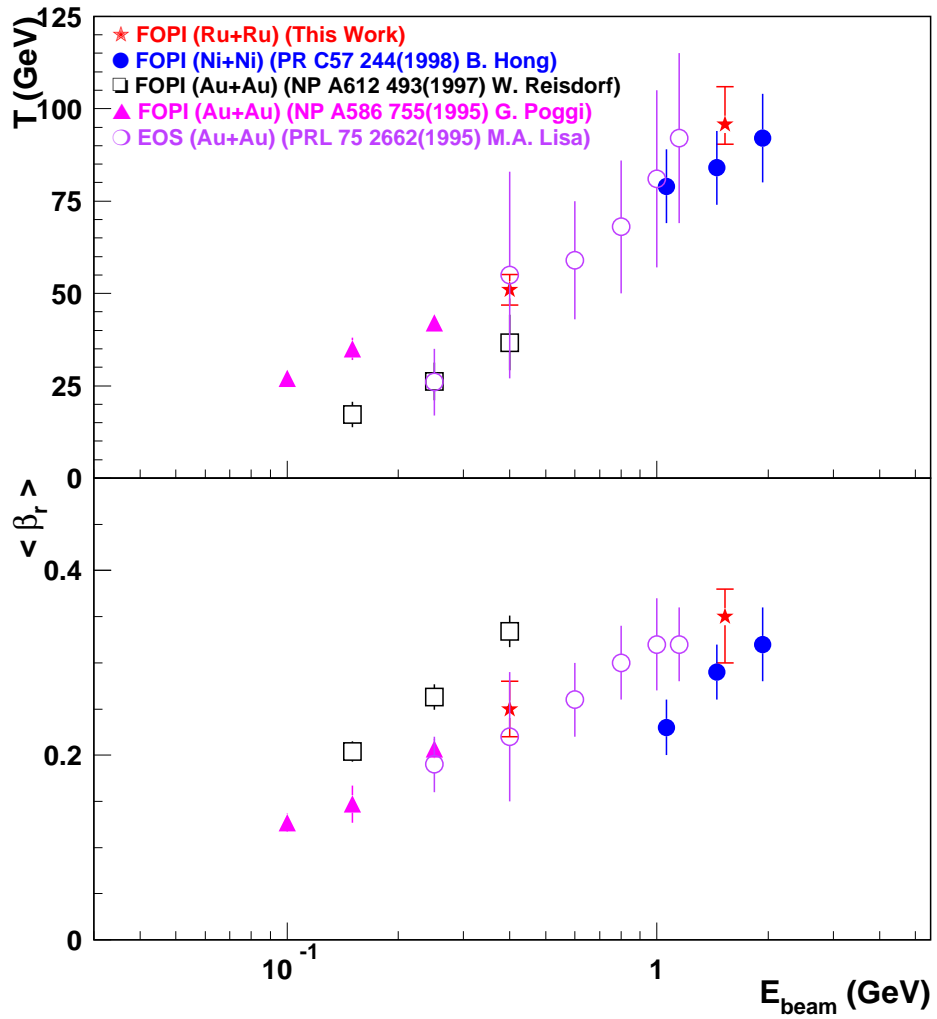


Figure 4.8: Comparison of the temperature (top) and the mean radial flow velocity (bottom) of various experiments as a function of the beam energy [15, 47, 49, 50].



- Choice of the fit functions for the invariant spectra.
- Uncertainty of obtained physical values by fitting data due to the limited geometrical acceptance.

The systematic error of total production yields of the proton and light fragments is presented in the last column of the table 4.1. The yield of the triton at 1.5 AGeV has a relatively large systematic error due to the uncertainties of the charge separation and PID in the forward region due to a large background. The systematic error of the ${}^4\text{He}$ at 1.5 AGeV has even large systematic error, because the production yield is relatively small. In figure 4.7, the systematic errors of the radial flow velocity are 12% and 14% at 0.4 and 1.528 AGeV, respectively. The systematic errors of the temperatures are about 8% and 11% at 0.4 and 1.528 AGeV, respectively.

4.2 Differential elliptic flow

The differential elliptic flows, v_2 , of the protons and the light fragments have been analyzed at the mid-rapidity for $|y^{(0)}| \leq 0.5$ at 0.4 AGeV and $-0.5 \leq y^{(0)} \leq 0.0$ at 1.528 AGeV. For the event centrality given in table 3.2, the differential elliptic flows of the light fragments as a function of the transverse momentum, p_t , are presented at 0.4 (top) and 1.528 (bottom) AGeV in figures 4.9, 4.10, and 4.11 in comparison with the proton data. The magnitudes of the v_2 values of the particles increase linearly with p_t . The differential elliptic flow for peripheral collisions rises more rapidly than that of the central collisions.



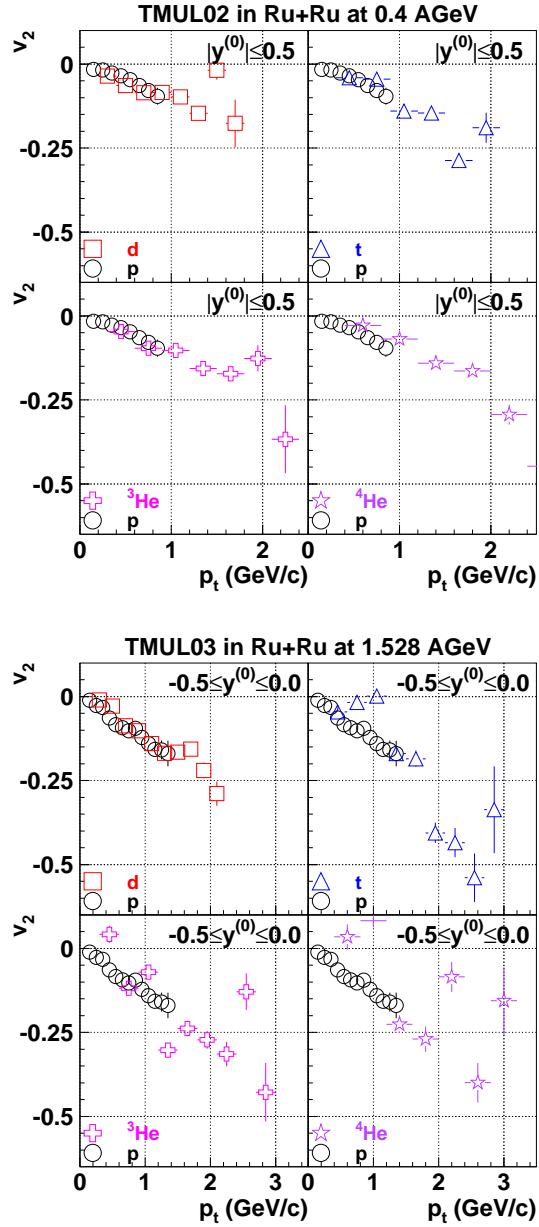


Figure 4.9: Differential v_2 distributions of the light fragments as a function of p_t in comparison with that of the protons in central Ru+Ru collisions at 0.4 (top) and 1.528 (bottom) AGeV.



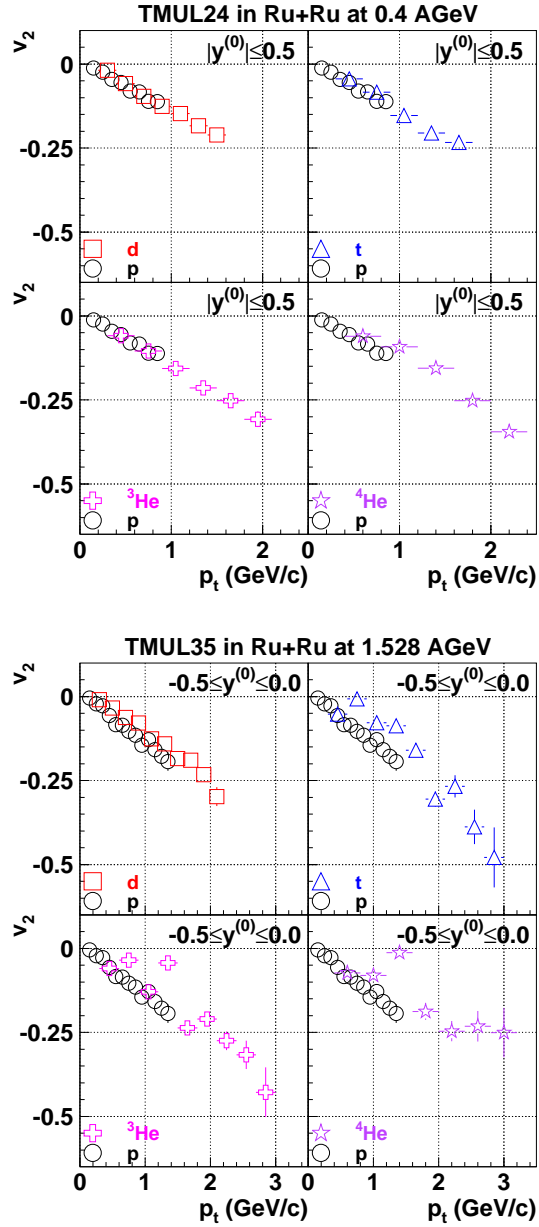


Figure 4.10: Differential v_2 distributions of the light fragments as a function of p_t in comparison with that of the protons in semicentral Ru+Ru collisions at 0.4 (top) and 1.528 (bottom) AGeV.



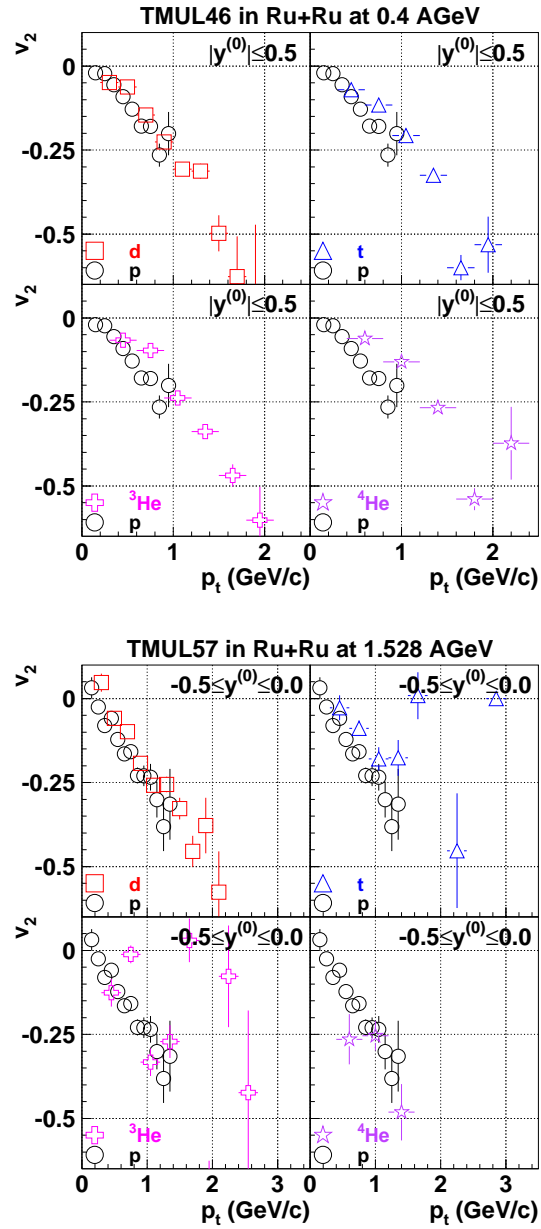


Figure 4.11: Differential v_2 distributions of the light fragments as a function of p_t in comparison with that of the protons in peripheral Ru+Ru collisions at 0.4 (top) and 1.528 (bottom) AGeV.



4.3 Nucleon coalescence parameters

In this section, we have tested the nucleon coalescence model in two different way. First, we applied equation 1.5 to the invariant spectra of light fragments. And, then, we compared the scaled differential elliptic flow, v_2/n , where n is the number of composite nucleons.

4.3.1 Coalescence coefficient B_A

In figures 4.12 and 4.13, the invariant spectra of the light fragments (symbols) are displayed with the scaled and powered invariant spectra of protons (dashed lines) calculated by equation 1.5 in Ru+Ru collisions at 0.4 and 1.528 AGeV, respectively. Here the spectra of neutrons in equation 1.5 are assumed to be identical to those of protons.

Figure 4.12 shows that equation 1.5 are satisfied within 10% not only at the mid-rapidity, but also at the whole rapidity region for d and ${}^3\text{H}$ at 0.4 AGeV. A similar agreement ($\sim 10\%$) can be also found for ${}^3\text{He}$ and ${}^4\text{He}$ at the high- p_t region ($p_{At} > 1$ GeV/ c). But the discrepancies are larger at $\sim 20\%$ for $p_{At} < 1$ GeV/ c .

For 1.528 AGeV, the spectra of the light fragments, except ${}^3\text{He}$ at $p_{At} < 1$ GeV/ c , and the scaled spectra of protons agree within $\sim 25\%$ for $p_{At} < 1$ GeV/ c , and less than 10% at $p_{At} > 1$ GeV/ c as shown in figure 4.13. In $p_{At} < 1$ GeV/ c at 1.528 AGeV, there are somewhat large discrepancies between the spectra of ${}^3\text{He}$ and the scaled spectra of proton, which is still to be understood. Therefore, for this region the invariant spectra of ${}^3\text{He}$ and proton by the CDC were used to estimate the coalescence parameter.

Figure 4.14 shows the coalescence parameters, B_A , estimated by the CDC data, as a function of the normalized rapidity. The coalescence parameter values decrease with the beam energy. In addition, they are almost independent of the rapidity near the mid-rapidity.



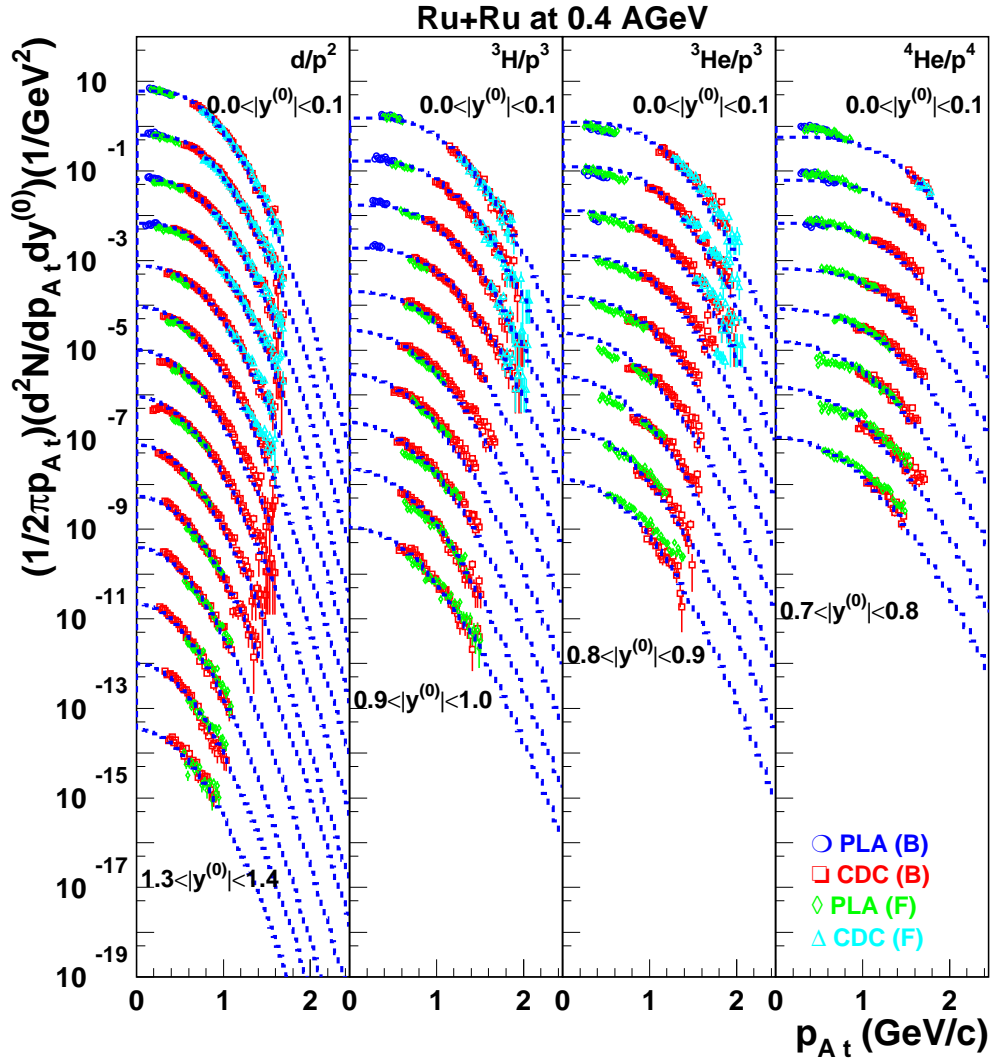


Figure 4.12: Invariant spectra of the light fragments with the powered invariant spectra of protons (dashed lines) calculated by equation 1.5 for the most central Ru+Ru collisions at 0.4 AGeV. The detail explanation is given in the text.



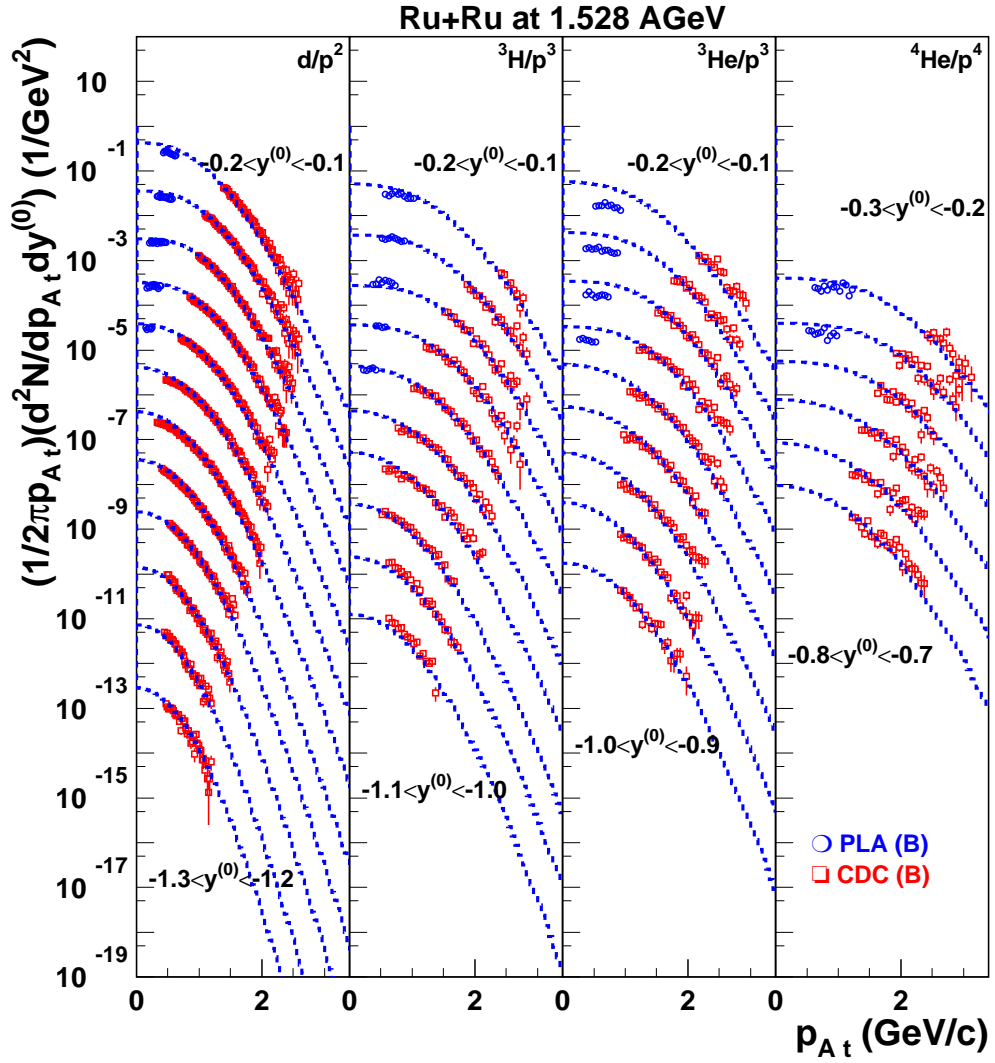


Figure 4.13: Invariant spectra of the light fragments with the powered invariant spectra of protons (dashed lines) calculated by equation 1.5 for the most central Ru+Ru collisions at 1.528 AGeV. The detail explanation is given in the text.



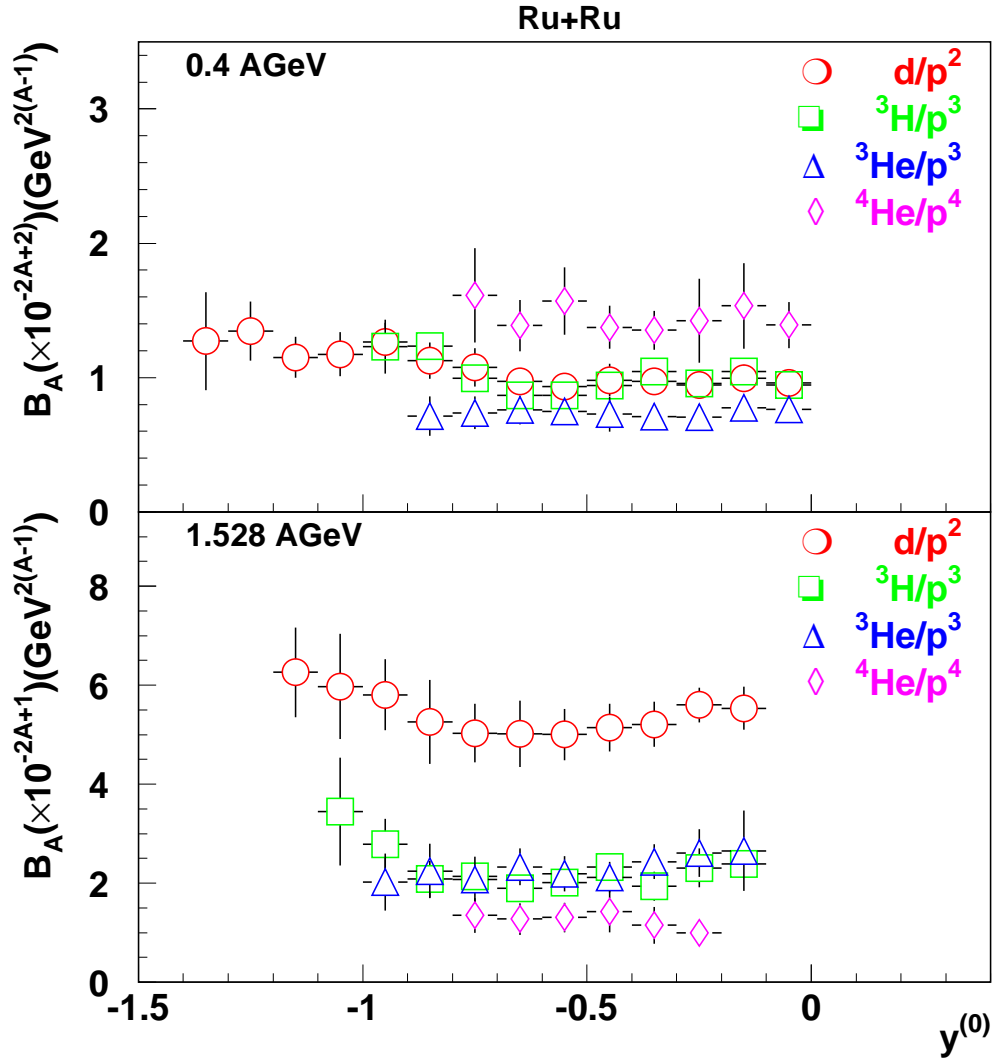


Figure 4.14: Coalescence parameter B_A estimated by the coalescence model for most central Ru+Ru collisions at 0.4 (top) and 1.528 (bottom) AGeV. The detail explanation is given in the text.



4.3.2 Scaled differential elliptic flow

In order to test the nucleon coalescence scenario, the scaled differential elliptic flows of the light fragments at mid-rapidity ($|y^{(0)}| \leq 0.5$ at 0.4 AGeV and $-0.5 \leq y^{(0)} \leq 0.0$ at 1.528 AGeV) have been obtained, and compared with those of protons. For the centralities given in table 3.2, the scaled differential elliptic flow, v_2/n , of the light fragments as function of the scaled transverse momentum, p_t/n , is presented with the proton data at 0.4 (top) and 1.528 (bottom) AGeV in figures 4.15, 4.16, and 4.17. For all investigated centralities, the scaled differential v_2/n distributions of the light fragments agree well with that of proton at 0.4 AGeV. This agreement is in accord with nucleon coalescence scenario in heavy-ion collisions. Unfortunately, for the peripheral collisions at 1.528 AGeV, we need to accumulate more statistics.



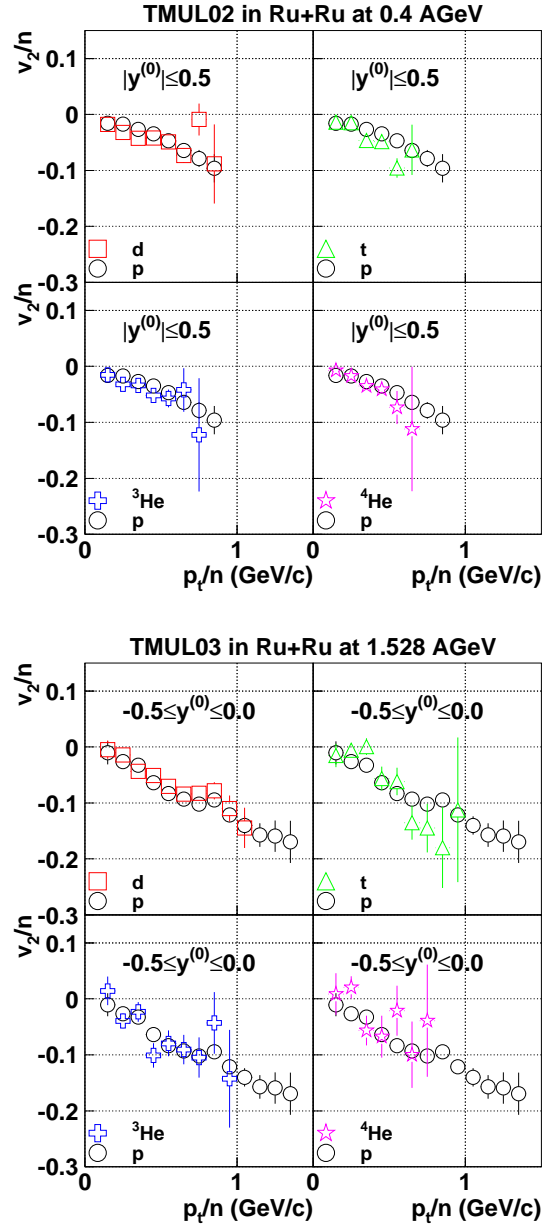


Figure 4.15: Scaled differential elliptic flow distribution, v_2/n , of the light fragments as a function of p_t/n compared with the proton data for central Ru+Ru collisions at 0.4 (top) and 1.528 (bottom) AGeV.



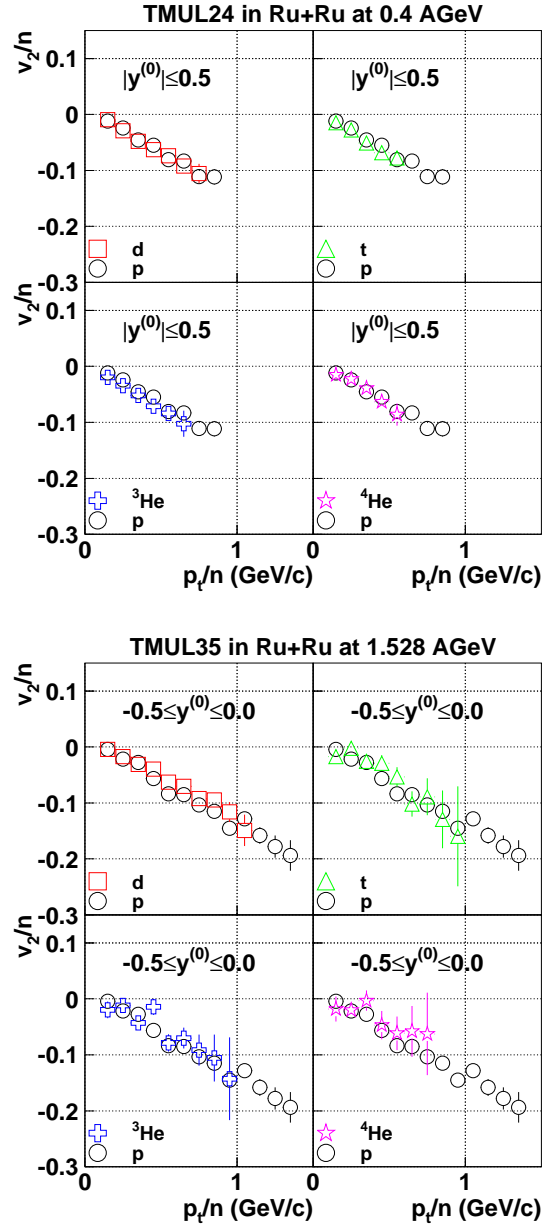


Figure 4.16: Scaled differential elliptic flow distribution, v_2/n , of the light fragments as a function of p_t/n compared with the proton data for semicentral Ru+Ru collisions at 0.4 (top) and 1.528 (bottom) AGeV.



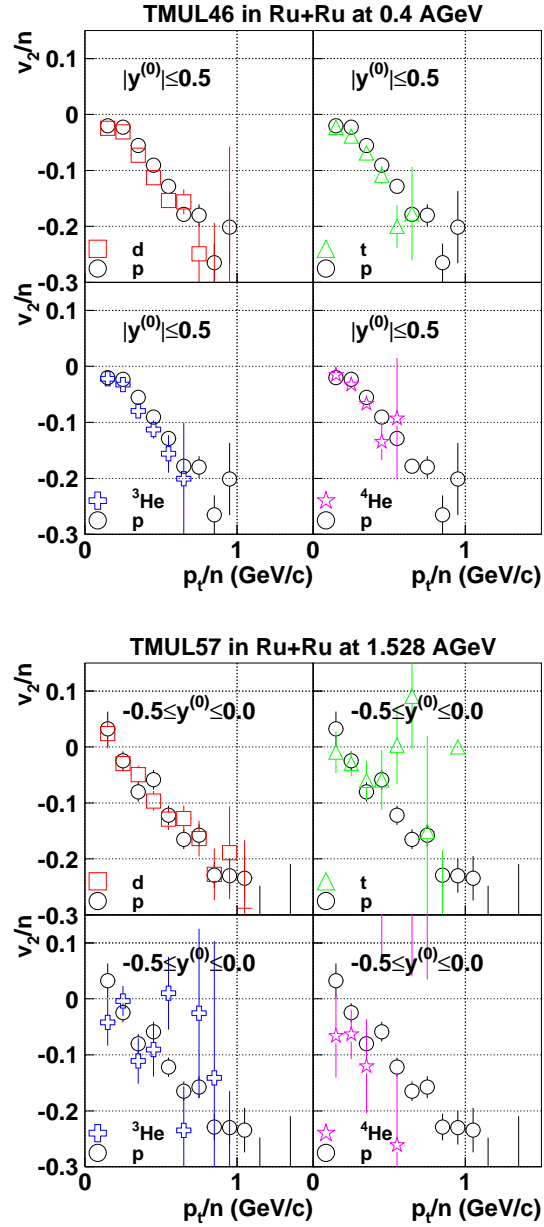


Figure 4.17: Scaled differential elliptic flow distribution, v_2/n , of the light fragments as a function of p_t/n compared with the proton data for peripheral Ru+Ru collisions at 0.4 (top) and 1.528 (bottom) AGeV.



Chapter 5

Part I : Conclusions

In order to understand the characteristics of hot and dense nuclear matter, we have studied the formation of the hydrogen (p , d , and ${}^3\text{H}$) and the helium isotopes (${}^3\text{He}$ and ${}^4\text{He}$) in ${}^{96}_{44}\text{Ru}+{}^{96}_{44}\text{Ru}$ collisions at 0.4 and 1.528 AGeV. First how much particles are produced at the chemical freeze-out point by using the rapidity distribution and total production yield, second the expansion velocity and temperature at mid-rapidity when the fireball reach the thermal freeze-out point, third how the particles move in the compressed fireball by investigating the collective elliptic flow, fourth whether the nucleon coalescence scenario is valid or not by obtaining the coalescence parameter and scaled elliptic flow.

For the most central collisions, We presented the phase-space distributions of the hydrogen and the helium isotopes, corrected for the matching between trackers and time-of-flight detectors and the tracking efficiencies. The rapidity distributions and the production yields of the proton and light fragments were estimated by fitting the invariant spectra by the simple thermal blast model formula. We have obtained the production results of the proton and deuteron being compatible with the reported results in the ref. [16]. And the new results has been presented about the production of ${}^3\text{H}$, ${}^3\text{He}$, and ${}^4\text{He}$. The radial flow velocity and the temperature at the midrapidity were extracted and well agree with the published results [15].



For the central, semicentral, and peripheral collisions, the differential elliptic flow, v_2 , as a function of the transverse momentum, p_t , of the proton and light fragments has been obtained. The magnitudes of the v_2 values of the particles increase linearly with p_t . Furthermore, the v_2 values for peripheral collisions increase faster than that for central collisions.

We have obtained that the invariant spectra of the light fragments, which were compared with the scaled and powered invariant spectra of protons, for the most central Ru+Ru collisions at 0.4 and 1.528 AGeV. The invariant spectra of d , ${}^3\text{H}$, and ${}^4\text{He}$ agree with the scaled and powered invariant spectra of protons. The agreement were very good except for ${}^3\text{He}$ at 1.528 AGeV. There are somewhat large discrepancies between the spectra of ${}^3\text{He}$ and the powered spectra of proton for the low p_t region for 1.528 AGeV. The coalescence parameter values decrease with the beam energy, but they are almost independent of the rapidity near the midrapidity.

The scaled differential elliptic flows, v_2/n , where n is the number of composite nucleons, of the light fragments as a function of the scaled transverse momentum, p_t/n , were analyzed and compared to that of protons. For all collision centralities, the scaled differential v_2/n distributions of the light fragments agree well with that of protons at 0.4 AGeV which is in accord with the nucleon coalescence scenario in heavy-ion collisions. For semicentral collisions at 1.528 AGeV, the scaled differential v_2/n distributions of the light fragments are well overlapped with that of proton. For central collisions, the v_2/n distributions of the light fragments were agreed with that of proton, but the data for ${}^3\text{H}$ and ${}^4\text{He}$ require more number of events particularly for $p_t/n > 0.5$ GeV/ c . For peripheral collisions, the v_2/n distribution of the deuterons agree with the proton data, but other data sets for heavier particles require more statistics. The observed scaling phenomenon of the elliptic flow for light fragments implies the nucleon coalescence scenario in heavy-ion collisions at SIS18 energies.





PART II

Multigap Resistive Plate Chamber





Chapter 6

Part II : Introduction

The resistive plate chamber (RPC) is utilized not only for nuclear and particle physics experiments for the precise time and position measurements of charge particles [51, 52] but also for various applications to the neutral particle detection and the imaging device [53, 54]. The most attractive features of the RPC are the high detection efficiency and good time resolution, fast response to incoming particles, and the low production cost due to the simple structure. These advantages are required features for the construction of large area detector system in high energy nuclear and particle physics experiments. Since 1981, when the RPC operated in streamer mode was developed by Santonico and Cardarelli [55], the RPC has been modified and improved when the experiments demand better performance [56].

The RPC can be classified into the timing and the trigger RPCs. The FOPI at SIS18/GSI has been completed the timing RPC system made of eight gas gaps by using the glass as electrode to increase the momentum reach of the charged kaons up to 1 GeV/c [51]. The schematic diagram of the upgraded FOPI detector is shown in figure 6.1.

The RPC comprises the gas volume which has a consistent gap thickness between two resistive plates as shown in figure 6.2. The popular material of resistive plate is bakelite or glass, depending on the experimental requirements. The variation of the bulk resistivity of the glass plates is less sensitive



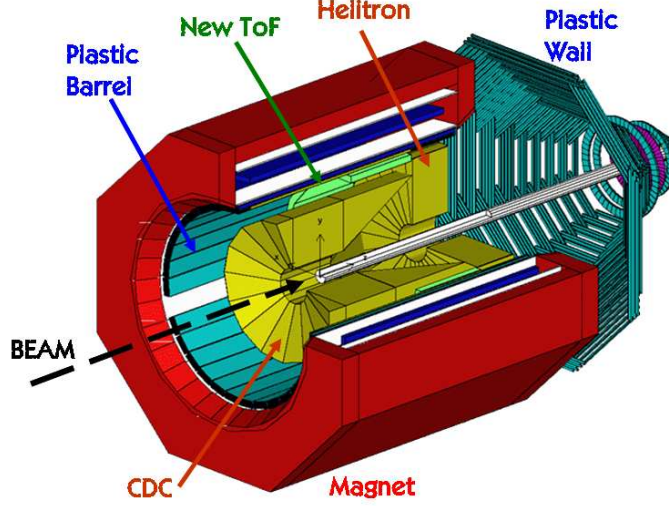


Figure 6.1: Schematic diagram of the upgraded FOPI detector with new time-of-flight system.

to the humidity than the bakelite which is very popular material for the trigger RPC [57, 58]. When the charged particles pass through the gas gap, which is filled with the mixed gas, the pair of electrons and positive ions are produced. Usually, the combination of $C_2F_4H_2$, $i-C_4H_{10}$, and SF_6 are used for the mixed gas. Then, the size of the electron clouds continuously increase by means of the avalanche multiplication process, while they are drifting along electric field lines to the anode plate due to applied high voltage. The created electron cluster induces the signal on the read-out panel.

The simulation model for the RPC operation has been improved by Riegler, Lippmann, and Veenhof [59, 60, 61] to solve the discrepancies between the experimental data and the simulation results. The recent simulation model shows that the average total avalanche charge is given by

$$Q \approx \frac{e_0 n_{av} \alpha}{\lambda(\alpha - \eta)^2} e^{(\alpha - \eta)d}, \quad (6.1)$$

where e_0 is the electron charge, n_{av} is the average number of electrons in a cluster, α is the Townsend coefficient, η is the attachment coefficient, λ is the



average distance between clusters, and d is the thickness of the gas gap. The average induced charge is given by

$$Q_{ind} \approx \frac{E_W}{V_W} \frac{e_0 n_{av}}{\lambda(\alpha - \eta)^2} e^{(\alpha - \eta)d}, \quad (6.2)$$

where E_W is the weighted electric field in the gas gap when the electrical potential (V_W) is applied. The RPC efficiency is, approximately, given by

$$\varepsilon = 1 - e^{-(1 - \frac{\eta}{\alpha}) \frac{d}{\lambda}} \left[1 + \frac{E_W}{V_W} \frac{\alpha - \eta}{e_0} Q_t \right]^{\frac{1}{\alpha\lambda}}, \quad (6.3)$$

where Q_t is the threshold value in the unit of Coulomb. The RPC time resolution is, approximately, given by

$$\sigma_t = \frac{1.28}{(\alpha - \eta)v}. \quad (6.4)$$

where v is the drift velocity.

The RPC can be operated in either the avalanche or streamer mode, depending on the strength of the electric field. The gains of the avalanche and streamer modes are around 10^6 and 10^8 , respectively. The pulse size of the streamer mode using local discharges is larger than that of the avalanche mode being created by a factor of a few tens. It means that the avalanche mode needs fast signal processing and high gain preamplifier contrary to the streamer mode which does not need any complicated electronics.

For the avalanche mode operation, the discharge appearing in the gap can be reduced in a gap being wider the gap thickness, which results in a relatively bad timing performance. To keep the rate capability and timing performance simultaneously [58, 62, 63], the multigap RPC was developed. The sum of the generated individual clusters in each sub-gap of the multigap RPC induces the pickup signal on the read-out panel. The time resolution of the RPC is determined by the time jitter of the induced signal, occurred by the variation of the position of the primary ionization cluster. The time walk in the multi-narrow-gap structure can be reduced by a shorter drift distance than a single-wide-gap. The time walk can be corrected by using the relation between the time and charge distributions as shown in figure 6.4.



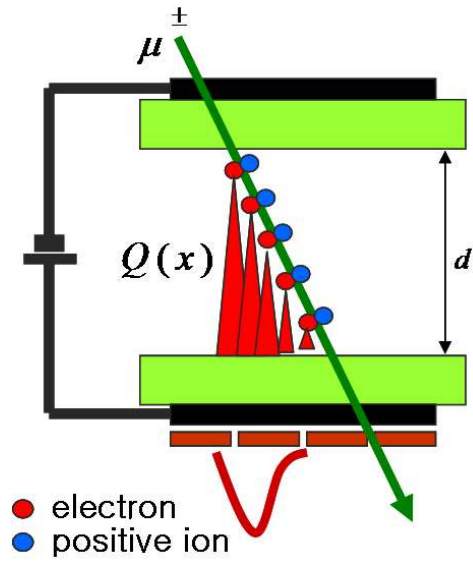


Figure 6.2: Operational principle of the single gap RPC.

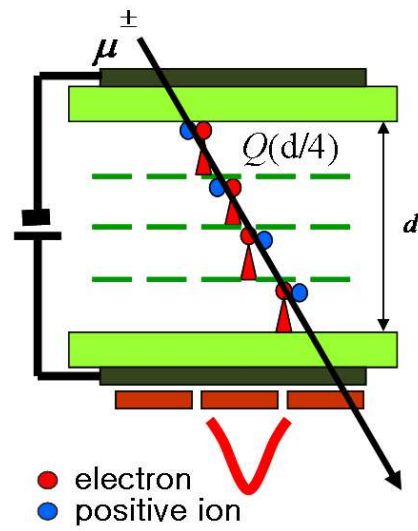


Figure 6.3: Operational process of the multigap RPC.



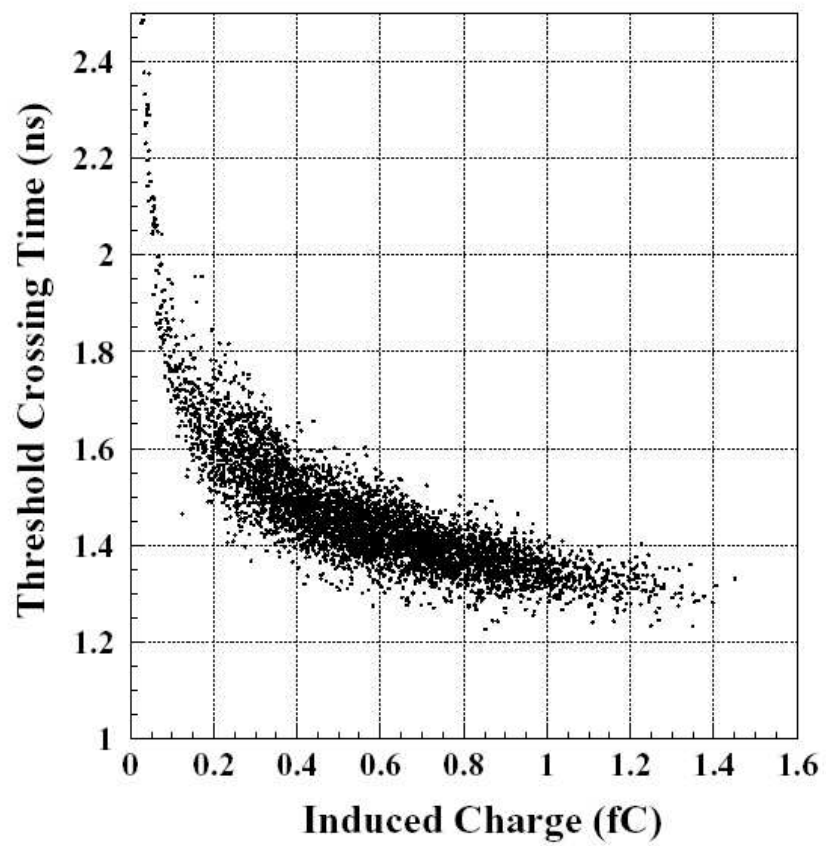


Figure 6.4: Correlation between the time and the charge of the induced signals [59].



Chapter 7

Part II : Detector Configuration

In this chapter, two prototype multigap RPCs with thin normal glass plates and readout strips will be described. In addition, the front-end-electronics (FEE) developed by the FOPI collaboration at GSI will be introduced.

7.1 Design and construction

The thickness of the resistive glass plates was $700 \mu\text{m}$. The normal glass plates have a very uniform thickness in $0.01 \mu\text{m}$ tolerance. The bulk resistivity of the glass plates was $1.5 \times 10^{13} \Omega \cdot \text{cm}$.

The schematic plane and side views are shown in figures 7.1 and 7.2, respectively. Each RPC consisted of four gas gaps keeping the thickness by fishing line whose diameter is $260 \mu\text{m}$. The dimension of the active area for each multigap RPC was $15 \times 17 \text{ cm}^2$, which was defined by the area of electrodes coated by the graphite ink. The silk screen technique was used to coat a thin graphite electrode layer on the outer surface of the glass plate for the high voltage and ground connections. The surface resistivity of the electrodes for the present RPCs was maintained at about $100 \text{ k}\Omega/\square$. Before the graphite coating, the small copper tapes were attached to the glass plates



for the connection of high voltage and ground cables. The soldered high voltage cables on these copper tapes were sealed with high-dielectric hot-melt glue in order to prevent sparks.

For the readout strip planes, an epoxy-glass-plated board, also known as G10, with copper layer attached was used. The copper layer was etched by using FeCl_3 solution after having been masked out the strip whose width was 20 mm with the 2 mm spacing between neighboring strips.

The readout plane was located between two subchambers. Each subchamber consists of two gas gaps in the gas vessel as shown in figures 7.1 and 7.2. For the flow of the mixed gas, the gas-gap thickness ($260 \mu\text{m}$) was not enough for a direct connection of inlet and outlet connectors ($\phi = 2 \text{ mm}$). Therefore, we built a gas vessel made of the acryl boards for the enclosure of the mixed gas and protecting the fragile glass plates from the physical impact.

7.2 Front-end-electronics (FEE)

The FEE has been developed by the FOPI collaboration at GSI in order to upgrade the time-of-flight (TOF) system of the FOPI detector [64]. Figure 7.3 is the picture of the FEE card shown with the characteristic description. This FEE card is characterized by a 1-GHz bandwidth, good time resolution and adjustable gain. One test input receives the logic pulse then creates the analog and logic pulses through all output channels. Four input channels have the analog and logical output channels each. The power of the FEE card for +12 V (0.35 A), +6 V (0.06 A), and -6 V (0.25 A) is applied by the Agilent low voltage power supply, N6700 and 6743B. The current values in the parenthesis above are the loaded ones on the FEE. The analog output signals were amplified once more (as much as a fraction of two, but adjustable) for the time output signals.

For the present RPC test, we set at 100 for the gain of the FEE. The test input pulse (left) from the pulse generator and the amplified output pulse (right) via the preamplifier on the FEE card are shown in figure 7.4 in the avalanche mode operation. In figure 7.5, the raw (Ch2) and the amplified



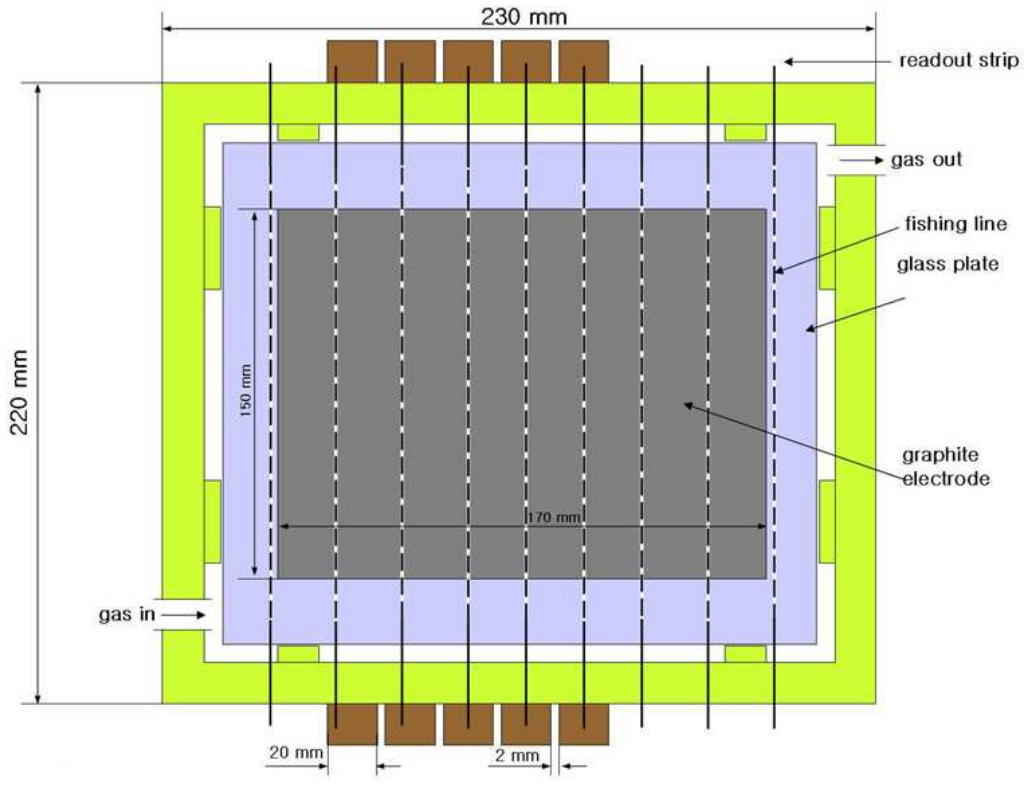


Figure 7.1: Schematic plane view of a multigap RPC with its dimensions.

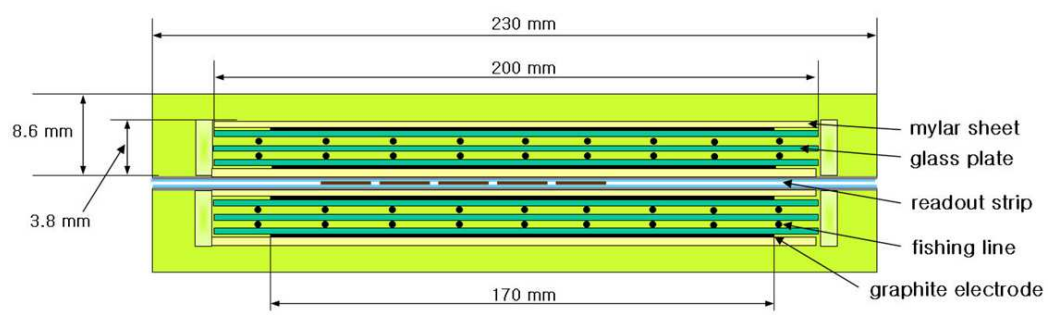


Figure 7.2: Schematic side view of a multigap RPC with its dimensions.



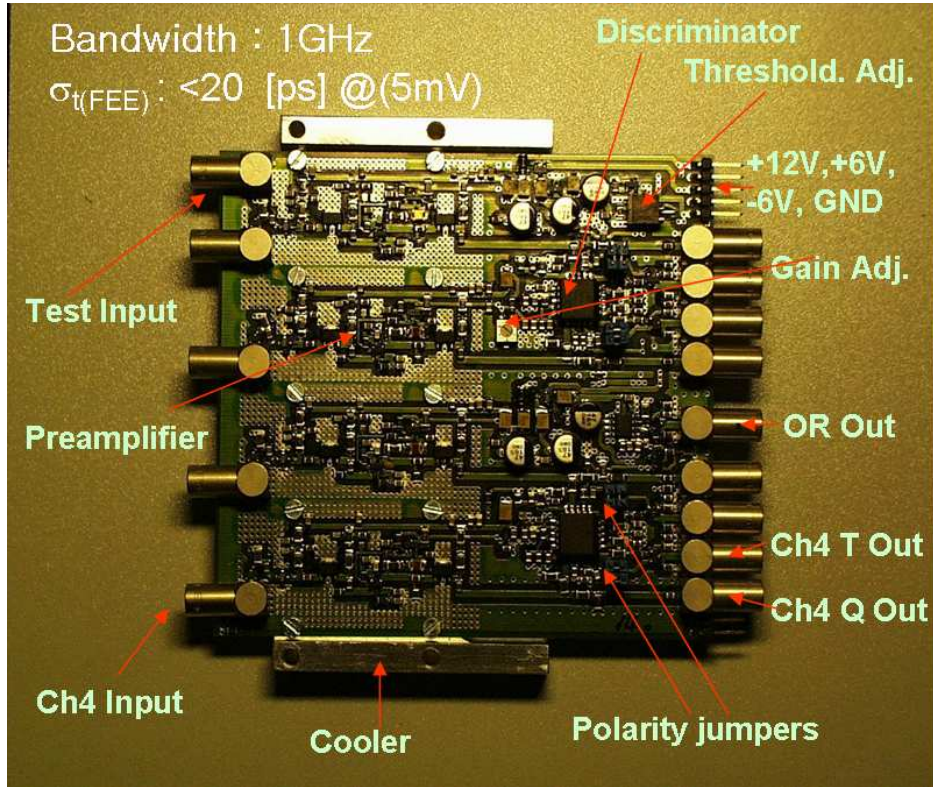


Figure 7.3: Picture of the FEE.

(Ch1) signals from the multigap RPC at the atmospheric pressure at 5.2 kV with 90% $\text{C}_2\text{F}_4\text{H}_2$, 5% $i\text{-C}_4\text{H}_{10}$, and 5% SF_6 are shown. Channel 3 is the coincidence signal from four scintillation detectors.



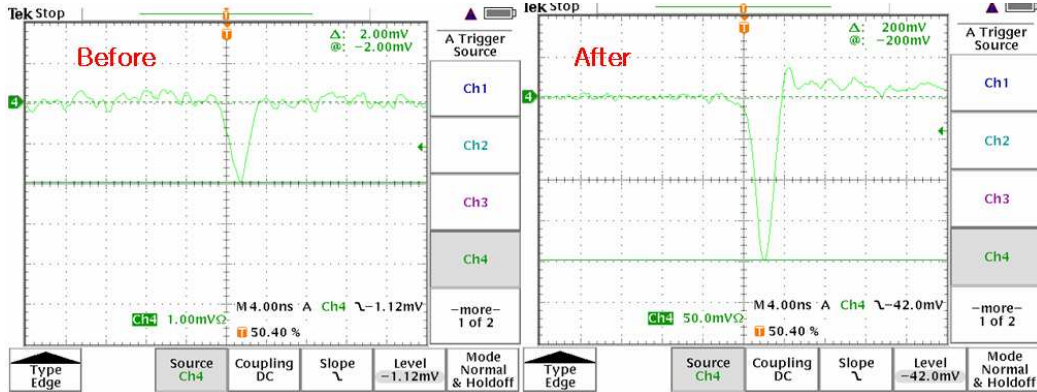


Figure 7.4: Test input pulse (left) and the amplified pulse (right) from the FEE. For the present test, we set at 100 for the gain of the FEE.

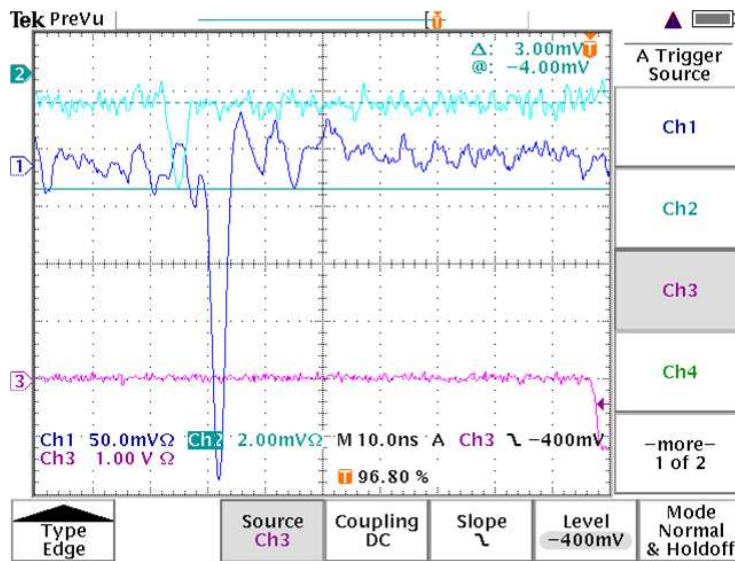


Figure 7.5: Raw signal (Ch2) from the multigap RPC with 90% $C_2F_4H_2$, 5% $i-C_4H_{10}$, and 5% SF_6 at the atmospheric pressure and the amplified signal (Ch1) with the gain of 100 via the FEE. Channel 3 is the coincidence signal from four scintillation detectors.



Chapter 8

Part II : Experimental setup

Because of the limited number of the electronics channels, we have measured the efficiency and the time resolution of the multigap RPCs with different setups. We operated the chambers in the avalanche mode.

8.1 Efficiency measurement

The trigger signals were the coincident signals from four scintillating counters. Two counters were placed below and the other two were placed above the multigap RPC, as shown in figure 8.1. Due to the limited number of the electronics channels, we read out only four strips from each RPC. One end of each strip was connected to the 50Ω coaxial cable and the other end was connected to 50Ω resistor.

Figure 8.2 shows the data acquisition (DAQ) setup for the efficiency measurement. When the charged particles hit the scintillating counters, light pulses entered photomultiplier tubes (PMTs) (Hamamatsu R2083) [36], which could be characterized by very fast responses with rise and electron transit times of 0.7 and 16 ns, respectively. The output signals from the PMTs were fed into the discriminator (CAEN N417), whose threshold voltage and the width of the output pulse were set at -30 mV and 40 ns, respectively. Then,



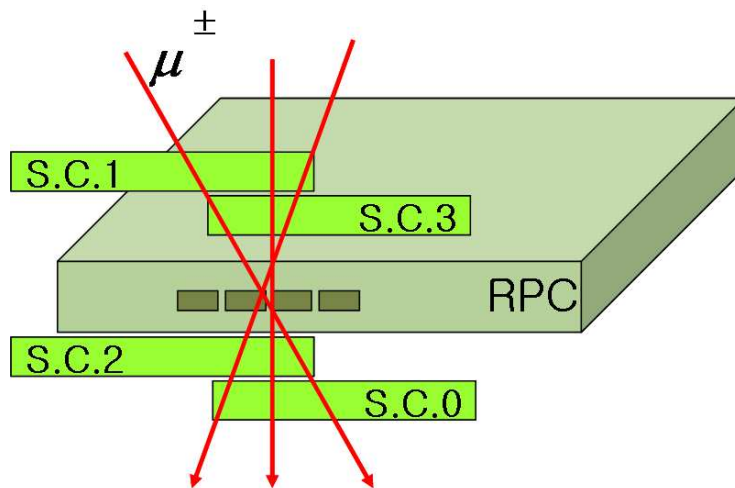


Figure 8.1: Schematic diagram of the experimental setup for the efficiency measurement.

the output logic pulses were fed into the 4-fold logic unit (LeCroy 365AL) to provide the coincidence signal, which was fed into a common START of the time-to-digital converter (TDC) (LeCroy TDC 2228A). One bin of the TDC was set at 50 ps, which is consistent with 100 ns full maximum ranges in a 10 bit data structure.

On the RPC side, the discriminator (LeCroy 623B) was used to exclude the noise and convert the analog outputs (Q_{out}) of the FEE to large-width logic signals, because the TDC only recognizes logic pulses with widths larger than 5 ns. The threshold of the discriminator was set with -40 mV, which is consistent with -80 mV for the FEE card. The output signals of the discriminator were fed into the STOPs of the TDC.

8.2 Time resolution measurement

Figures 8.3 and 8.4 show the schematic diagrams of the experimental



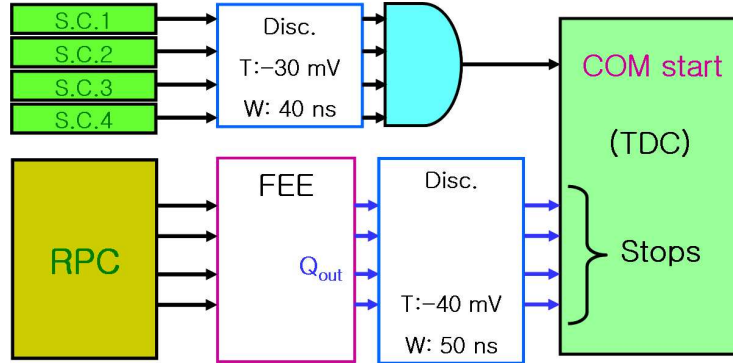


Figure 8.2: Schematic diagram of the DAQ system for the efficiency measurement.

setup and DAQ for the time resolution measurement. For the time resolution measurement, we used only one strip for the each RPC due to the limited number of channels for the FEE. The logical OR of the FEE was used for the time reference, which is the common START of the TDC, because the intrinsic time resolution of the multigap RPCs would be better than that of the scintillating counters. The coincidence signals from the four scintillating counters was served as trigger signals. In addition, the large-width 30 ns logical OR converted by a discriminator was used as the gate signal for the analog-to-digital converter (ADC) (LeCroy ADC 2249A).

The time outputs (T_{out}) of the FEE from both ends of a strip for each RPC were fed into the STOPS of the TDC. For the analysis, we took an average of two time signals for each RPC. The analog outputs (Q_{out}) of the FEE were transferred to the Charge signals of the ADC. One bin of the ADC was fixed at 0.25 pC. Later the average of two analog signals was used for the slewing correction.

The measured time resolution includes the contribution from the RPCs and electronics. By testing with the pulse generator, we determined the time resolution of the electronics (σ_{elec}) to be 15 ps, which will be subtracted from the measured time resolution.



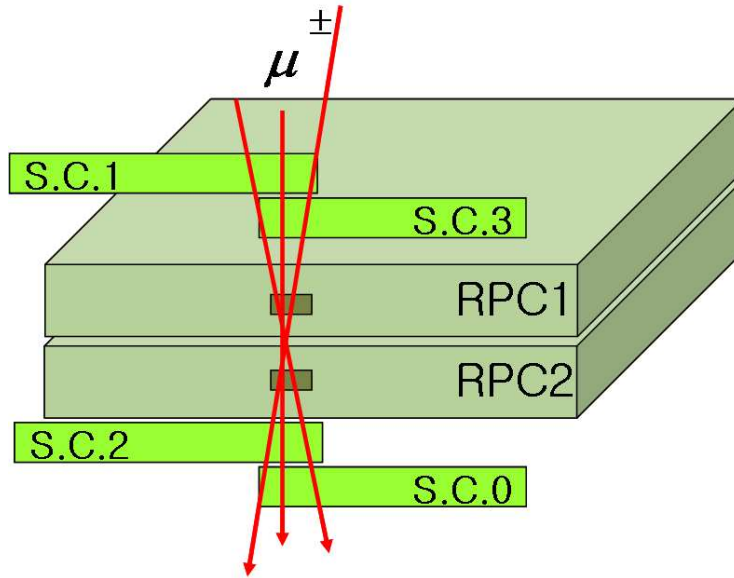


Figure 8.3: Schematic diagram of the experimental setup for the time resolution measurement.

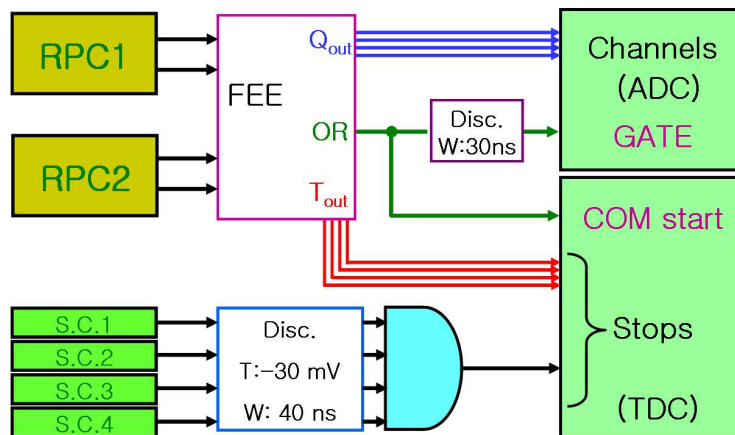


Figure 8.4: Schematic diagram of the DAQ system for the time resolution measurement.



Chapter 9

Part II : Experimental Results

In this chapter, the results of the efficiency and time resolution measurements will be presented. Two kinds of gas mixtures at atmospheric pressure were used: 85% $C_2F_4H_2$, 5% $i-C_4H_{10}$, and 10% SF_6 (gas mixture 1) and 90% $C_2F_4H_2$, 5% $i-C_4H_{10}$, and 5% SF_6 (gas mixture 2). The efficiencies were measured at both gas mixtures and the time resolutions were measured with gas mixture 1. These RPCs were tested previously with cosmic ray muons in the streamer mode operation with 93% $C_2F_4H_2$, 5.5% $i-C_4H_{10}$, and 1.5% SF_6 at the atmospheric pressure [65].

9.1 Efficiency

The efficiencies of the multigap RPC as a function of the applied high voltage has been measured with cosmic ray muons. The results are shown in figure 9.1, where the filled and open symbols represent the results for the gas mixture 1 and 2, respectively. Because of a larger SF_6 fraction in the gas mixture, the efficiency curves for the gas mixture 1 are shifted towards higher applied voltages. The RPC1 and RPC2 show a typical plateau behavior of the RPC and reach 90% at around 6.2 kV. The operational high-voltage plateau



range of the multigap RPCs is at least 400 V.

The error of the efficiency is calculated from the binomial distribution function [36]. The probability of success $P(r)$ is given by

$$P(r) = \frac{N!}{r!(N-r)!} p^r (1-p)^{N-r}, \quad (9.1)$$

where p is the probability of success in a single trial. If we try N times with efficiency ϵ , the mean μ , the variance σ , and the efficiency ϵ with the error δ are given by

$$\mu = Np, \quad (9.2)$$

$$\sigma = \sqrt{Np(1-p)}, \quad (9.3)$$

$$\epsilon \pm \delta = \left(\frac{\mu \pm \sigma}{N} \right) \times 100(\%) = \left(p \pm \sqrt{\frac{p(1-p)}{N}} \right) \times 100(\%). \quad (9.4)$$

Originally, two multigap RPCs were constructed in exactly same design and production procedure. But the efficiency curves show that the induced charge distribution between RPC1 and RPC2 could be different at the same applied high voltage as shown in figure 9.2. The RPC2 shows bigger streamer fraction than RPC1 at $q > 40$ pC. We can also anticipate that the total thickness of the gas gaps between RPC1 and RPC2 can be slightly different.

9.2 Time resolution without correction

We measured the time resolution of the present multigap RPCs at the operational plateau region. In figure 9.3, the raw time distributions at both ends of strips are shown at 6.4 kV. Similar distributions are also shown at 6.2 and 6.6 kV. One side of strip for each RPC is labeled as R and the other as L. Time difference spectra at 6.4 kV is given in figure 9.4 and the spectra at other high voltages in the operational plateau looked alike. Here, the time



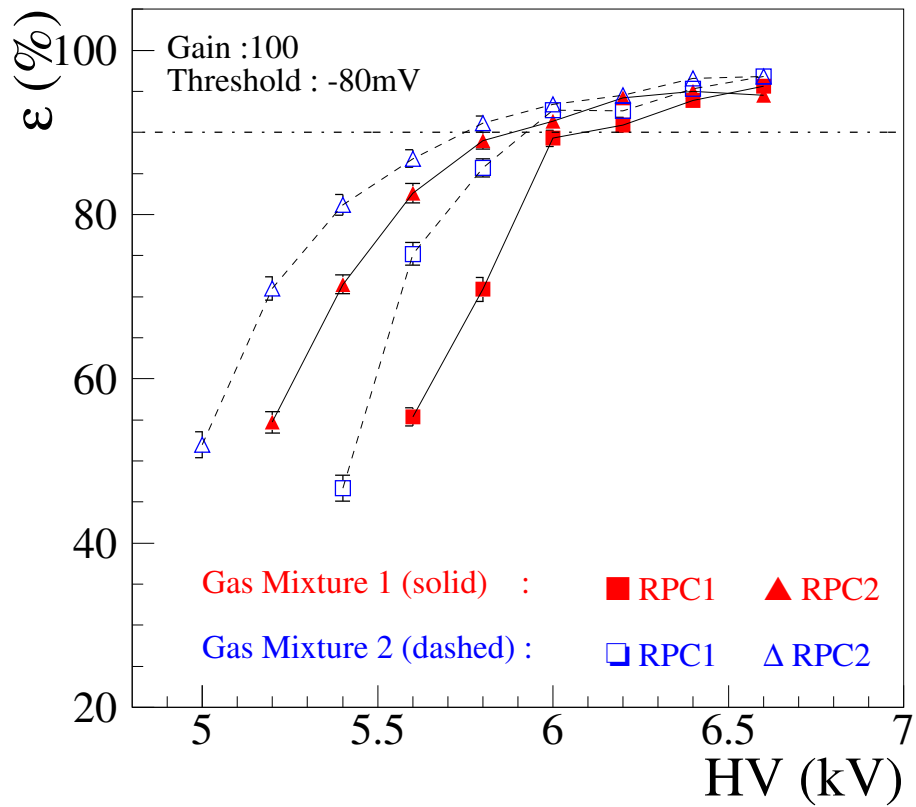


Figure 9.1: Efficiency of two multigap RPCs measured with cosmic ray muons as a function of the applied high voltage. The filled symbols are for gas mixture 1 with a larger fraction of the SF₆ component. The dash-dotted line indicates 90% efficiency.



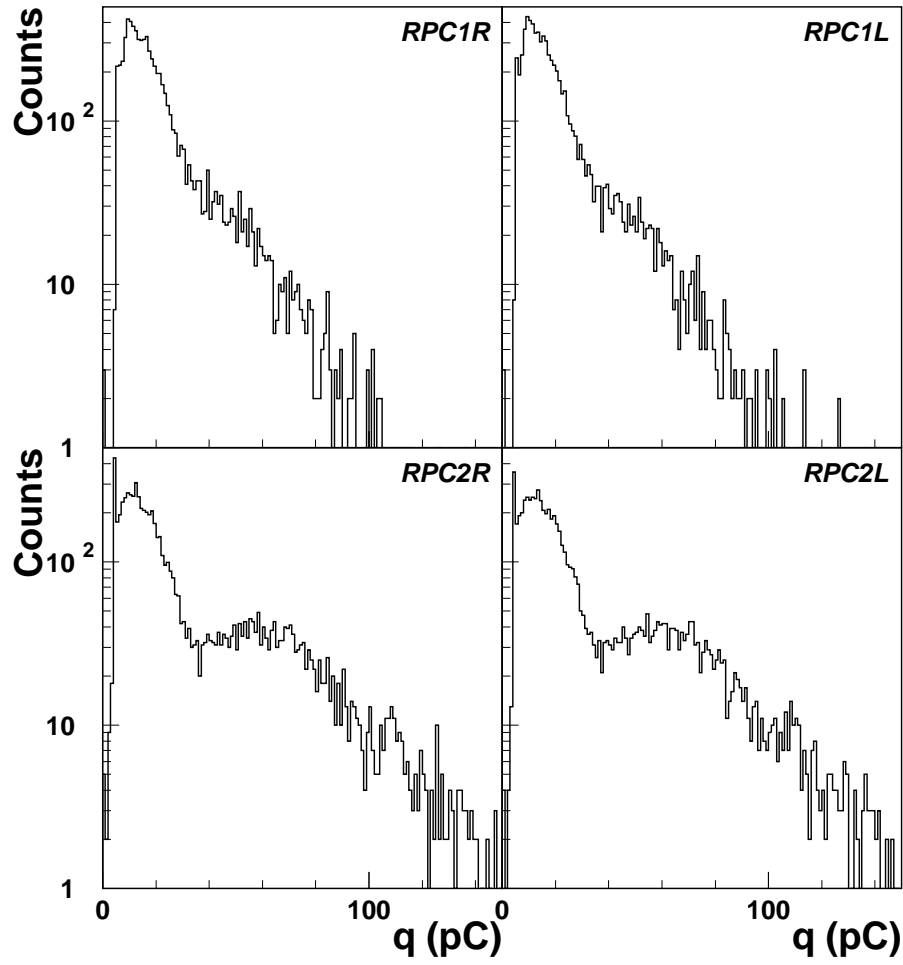


Figure 9.2: Raw charge distributions at both ends of strips of the RPC1 (top) and RPC2 (bottom) at 6.4 kV. One side of strip for each RPC is labeled as R, and the other as L. The pedestal values of the ADC are $q_{RPC1RP}=1.56$ pC, $q_{RPC1LP}=1.56$ pC, $q_{RPC2RP}=1.25$ pC, and $q_{RPC2LP}=1.31$ pC, respectively.



difference between RPC1 and RPC2 is defined as

$$\Delta t = \langle t_{RPC1} \rangle - \langle t_{RPC2} \rangle = \left(\frac{t_{RPC1R} + t_{RPC1L}}{2} \right) - \left(\frac{t_{RPC2R} + t_{RPC2L}}{2} \right) \quad (9.5)$$

The solid line in figure 9.4 represents the Gaussian fit function to the peak of the Δt distribution. The width, σ , of the fit function is 153 ps, which reflects the time uncertainties due to both RPCs. Assuming the time characteristics of two RPCs are identical, the time resolution of each RPC is obtained about 108 ps by dividing σ by $\sqrt{2}$.

Since 108 ps reflects the time resolution contributed not only by the RPC itself but also by the electronics, we can subtract the contribution by the electronics by using $\sqrt{(\sigma_{RPC})^2 - (\sigma_{elec})^2}$. If we substitute 15 ps for σ_{elec} (see section 8.2), the time resolution that contains only the RPC effect becomes about 107 ps, and we find that the effect of the electronics is about 1%.

The non-Gaussian tail component of the time difference distribution is one of the characteristics for the gaseous time-of-flight detectors [43]. The tail fraction (f_{tail}) is defined by the ratio of the integrated yield (S_{Gaus}) outside the Gaussian fit function to the total integration (S_{tot}) of the time difference spectrum:

$$f_{tail} = \frac{S_{tot} - S_{Gaus}}{S_{tot}}. \quad (9.6)$$

The tail fraction for $\pm 5\sigma$ is about 2.3% before the slewing correction. Usually the gaseous time-of-flight detectors require f_{tail} less than 3% [66].

9.3 Time resolution with slewing correction

In order to improve the time resolution of the RPCs, we estimated and corrected the slewing (or walk) effect due to the variation of the pulse size. The raw charge distributions at both ends of the strip for the multigap RPCs at 6.4 kV are shown in figure 9.2. The correlations between the average time, $\langle t_{RPC} \rangle$, from the TDC and the average charge, $\langle q_{RPC} \rangle$, from the ADC



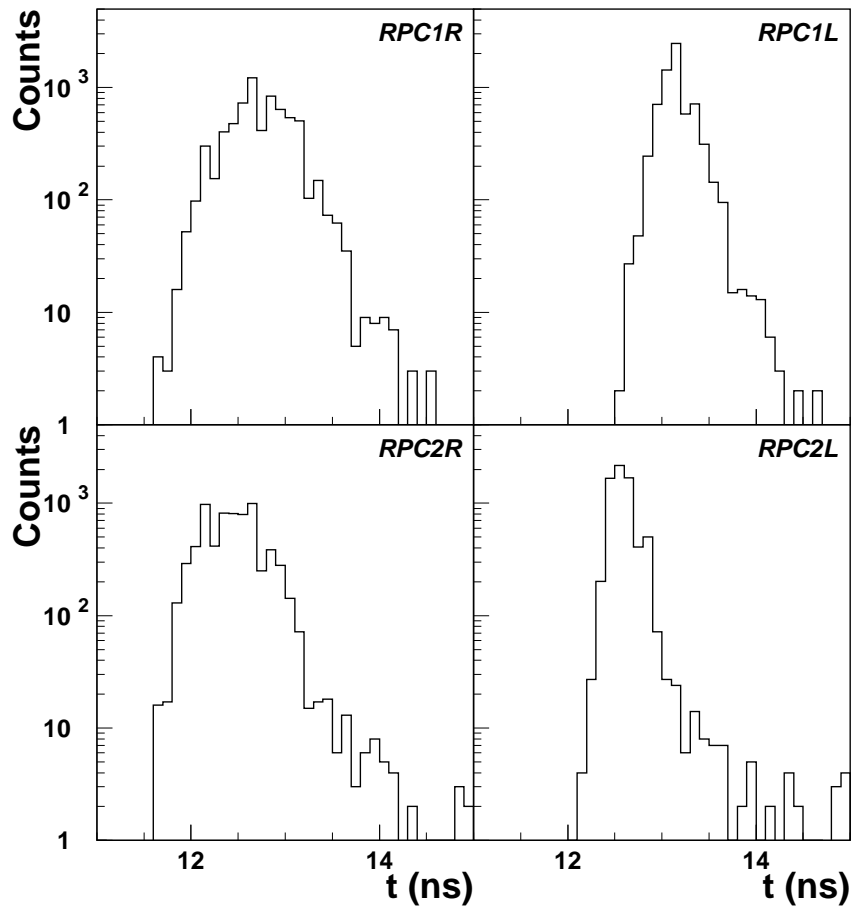


Figure 9.3: Raw time distributions at both ends of strips of the RPC1 (top) and RPC2 (bottom) at 6.4 kV. One side of strip for each RPC is labeled as R and the other side as L.



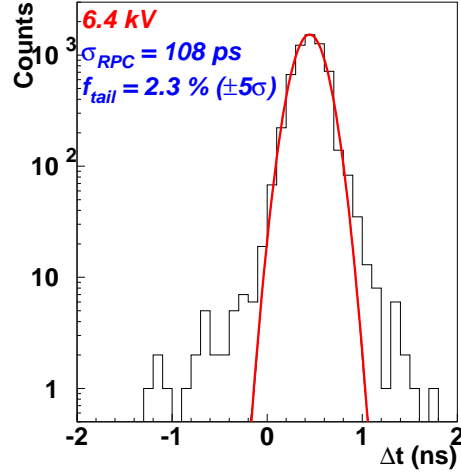


Figure 9.4: Raw spectra for the time difference between two multigap RPCs at 6.4 kV. The solid line is the Gaussian fit function to the peak.

are shown in figure 9.5 for the RPC1 (left) and RPC2 (right) before (top) and after (bottom) the slewing correction. Both RPCs do not show strong correlation between $\langle t_{RPC} \rangle$ and $\langle q_{RPC} \rangle$ at above $\langle q_{RPC} \rangle \geq 25$ pC. For the slewing correction of RPC2, we take only $\langle q_{RPC} \rangle$ for RPC1 larger than 25 pC and vice versa. The cross symbols show the mean values of the profile distributions of $\langle t_{RPC} \rangle$ vs. $\langle q_{RPC} \rangle$. The raw profile distributions in the top panel are fitted by using the following function (thick solid line):

$$\langle t_{RPC} \rangle = A \cdot \exp\left(\frac{B}{\langle q_{RPC} \rangle}\right) - C. \quad (9.7)$$

The fitted parameters A , B , and C for each RPC are summarized in table 9.1. The bottom panels of figure 9.5 shows the correlation between $\langle t_{RPC} \rangle$ and $\langle q_{RPC} \rangle$ after the slewing correction for each RPC. Finally, we see that the average time becomes insensitive to the size of the pulse.

After we perform the slewing correction for each RPC, the time difference spectrum at 6.4 kV is displayed in figure 9.6. The solid line is the Gaussian fit function to the peak. Assuming that the time characteristics of



Detector	H.V. (kV)	A (ns)	B ($\text{pC}^{1/2}$)	C (ns)
RPC1	6.2	12.9	0.037	0.11
	6.4	12.9	0.027	0.08
	6.6	12.9	0.032	0.11
RPC2	6.2	12.7	0.032	0.29
	6.4	12.7	0.032	0.31
	6.6	12.8	0.015	0.24

Table 9.1: Fit parameters of equation 9.7 for the slewing correction.

two RPCs are identical, we determined the intrinsic time resolution of one RPC as 89 ps by dividing σ by $\sqrt{2}$. The tail fraction for the $\pm 5\sigma$ cut is about 2.2% which is increased after the slewing correction but still satisfy the usual limit of the performance for the gaseous time-of-flight detectors.

Figure 9.7 summarizes the time resolution (top) and the tail fraction (bottom) of the multigap RPC as function of the high voltage in the operational plateau region. The σ_{RPC}^{NOCOR} without the slewing correction is about 110 ps and the σ_{RPC}^{COR} with the slewing correction is reached around 90 ps. The χ^2/dof of all time resolution is $3 \sim 6$ and the slewing correction improved the results by about 10%. In addition, the tail fraction of the time spectra for the $\pm 5\sigma$ cut is about 2%, which is the satisfying performance of the time-of-flight measurement, and the slewing correction worsened it only by 0.5%.



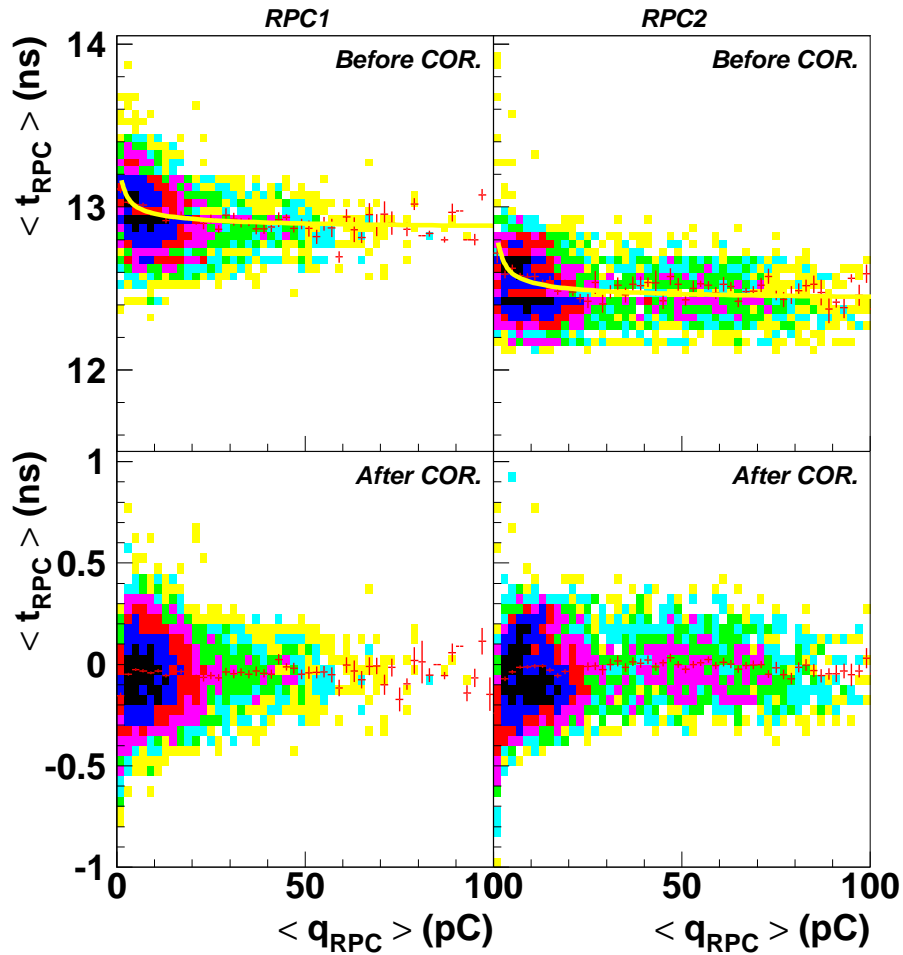


Figure 9.5: Correlation between the average time from the TDC, $\langle t_{RPC} \rangle$, and the charge from the ADC, $\langle q_{RPC} \rangle$, for the RPC1 (left) and RPC2 (right) before (top) and after (bottom) the slewing correction. The cross symbols show the mean values of the profile distributions of $\langle t_{RPC} \rangle$ vs. $\langle q_{RPC} \rangle$. The thick solid lines in the top panel are the fit function to the raw profile distributions. For the slewing correction of RPC2, we take $\langle q_{RPC} \rangle$ for RPC1 larger than 25 pC and vice versa.



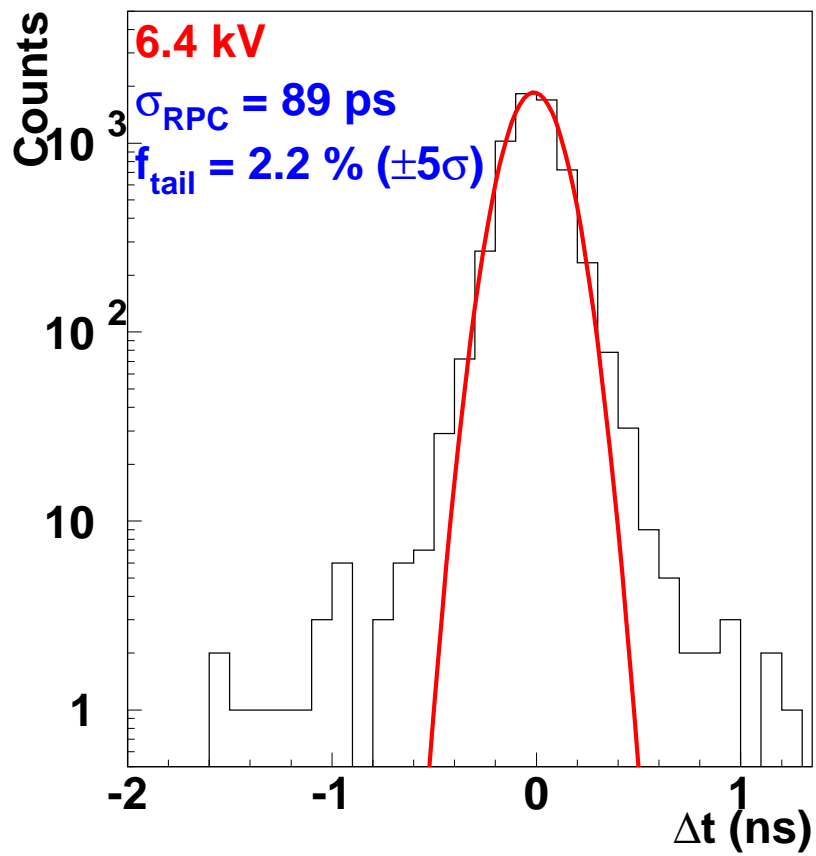


Figure 9.6: Time difference spectrum between two RPCs at 6.4 kV after the slewing correction. The solid line is the Gaussian fit function to the peak.



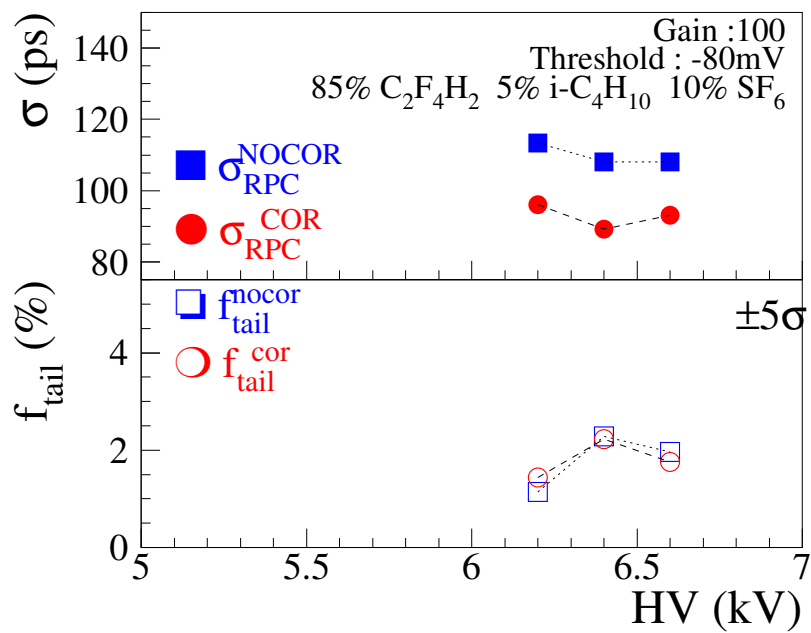


Figure 9.7: Time resolution and tail fraction of the multigap RPC measured with cosmic ray muons. Closed squares and circles are the time resolutions before and after the slewing correction, respectively. Open squares and circles are the tail fractions for the $\pm 5\sigma$ cut before and after the slewing correction, respectively.



Chapter 10

Part II : Conclusions

We have designed and built two prototype multigap RPCs made of normal glass plates with read-out strip. The characteristics of the RPCs have been investigated in the avalanche mode with two kinds of gas mixtures by using the cosmic-ray muons. The results obtained with the streamer mode have been published previously [65], and this thesis presents the experimental results for the avalanche mode operation.

The efficiency of the RPCs as a function of the high voltage showed a typical plateau behavior with a maximum efficiency larger than 90%. we measured that the operational plateau region extends at least 400 V.

For the analysis of the time resolution, the most important improvement came from the slewing correction which remove the dependence of the size of pulse on the timing performance. In the operational plateau region, the slewing correction reduces the time resolution by about 10 %, which makes the intrinsic time resolution of the RPC about 90 ps. Compared to the time resolution of the same RPCs in the streamer mode, which is 340 ps [65], avalanche mode operation provides a time resolution improved by about a factor of four. In the meantime, the non-Gaussian tail fraction, which is about 2%, of the time spectrum are not affected by the slewing correction.

Through the present measurement, the excellent performance of the multigap RPCs has been demonstrated by means of the efficiency, the time



resolution, and the tail fraction. And, finally, the present design of the multi-gap RPCs can be used in collision experiments for the charge particle identification.



Bibliography

- [1] J. Stachel and G. R. Young, *Annu. Rev. Nucl. Part. Sci.* **42**, 537 (1992).
- [2] H. Stöcker and W. Greiner, *Phys. Rep.* **137**, 277 (1986).
- [3] A. Andronic, P. Braun-Munzinger, and J. Stachel, *Nucl. Phys. A* **772**, 167 (2006).
- [4] W. Reisdorf and H. G. Ritter, *Annu. Rev. Nucl. Part. Sci.* **47**, 663 (1997).
- [5] N. Herrmann, J. P. Wessels, and T. Wienold, *Annu. Rev. Nucl. Part. Sci.* **49**, 581 (1999).
- [6] R. Averbeck, arXiv/9803001 [nucl-ex].
- [7] J. W. Harris and B. Muller, *Annu. Rev. Nucl. Part. Sci.* **46**, 71 (1996).
- [8] M. Harrison, S. Peggs, and T. Roser, *Annu. Rev. Nucl. Part. Sci.* **52**, 425 (2002).
- [9] J. M. Jowett, *J. Phys. G* **35**, 104028 (2008).
- [10] F. Halzen and A. D. Martin, *Quarks and Leptons*, Jone Wiley & Sons Ltd., New York, USA(1984).
- [11] J. Ritman, *Nucl. Phys. (Proc. Suppl.) B* **44**, 708 (1995).
- [12] D. Best *et al.*, *Nucl. Phys. A* **625**, 307 (1997).
- [13] X. Lopez *et al.*, *Phys. Rev. C* **75**, 011901 (2007).



- [14] M. Merschmeyer *et al.*, Phys. Rev. **C 76**, 024906 (2007).
- [15] B. Hong *et al.*, Phys. Rev. **C 57**, 244 (1998).
- [16] B. Hong *et al.*, Phys. Rev. **C 66**, 034901 (2002).
- [17] W. Reisdorf *et al.*, Phys. Rev. Lett. **92**, 232301 (2004).
- [18] N. Bastid *et al.*, Nucl. Phys. **A 622** , 573 (1997).
- [19] F. Rami *et al.*, Nucl. Phys. **A 646**, 367 (1999).
- [20] P. Crochet *et al.*, Phys. Lett. **B 486**, 6 (2000).
- [21] A. Andronic *et al.*, Nucl. Phys. **A 679**, 765 (2001).
- [22] J. Aichelin, Phys. Rep. **202**, 233 (1991).
- [23] Ch. Hartnack *et al.*, Eur. Phys. J. **A 1** , 151 (1998).
- [24] J. J. Molitoris and H. Stöcker, Phys. Rev. **C 32**, 346 (1985).
- [25] P. Danielewicz and G. Odyniec, Phys. Lett. **B 157**, 146 (1985).
- [26] J.Y. Ollitrault, Nucl. Phys. **A 638**, 195 (1998).
- [27] S. A. Voloshin *et al.*, Nucl. Phys. **A 715**, 379 (2003).
- [28] S. T. Butler and C. A. Pearson, Phys. Rev. Lett. **7**, 69 (1961).
- [29] S. T. Butler and C. A. Pearson, Phys. Rev. **129**, 836 (1963).
- [30] S. Das Gupta and A. Z. Mejkian, Phys. Rep. **72**, 131 (1981).
- [31] A. Schwartzschild and C. Zupancic, Phys. Rev. **129**, 854 (1963).
- [32] J. Gosset *et al.*, Phys. Rev. **C 16**, 629 (1977).
- [33] R. Scheibl and U. Heinz, Phys. Rev. **C 59**, 1585 (1999).
- [34] L. P. Csernai and J. I. Kapusta, Phys. Rep. **131**, 223 (1986).
- [35] FOPI Collaboration, Technical Proposal. GSI Report, 88-03, (1988).



- [36] W. R. Leo, Techniques for Nuclear and Particle Physics Experiments, Springer-Verlag, Berlin Heidelberg, Germany (1987).
- [37] Y. J. Kim, Ph. D. thesis, Korea University, Korea (2004).
- [38] T. Kress, Ph. D. thesis, Technische Universität Darmstadt, Germany (2002).
- [39] Particle Data Group, Phys. Lett. **B 667**, 267 (2008).
- [40] U. Fano, Ann. Rev. Nucl. Sci. **13**, 1 (1963).
- [41] GEANT User's Guide, CERN Program Library, CERN.
- [42] J. Ritman *et al.*, Z. Phys. **A 352**, 355 (1995).
- [43] A. Devismes, Ph. D. thesis, Technische Universität Darmstadt, Germany (2001).
- [44] S. Mohren, Ph. D. thesis, Ruprecht-Karls-Universität Heidelberg, Germany (1996).
- [45] K. Wiśniewski, Ph. D. thesis, Warsaw University, Poland (2001).
- [46] A. Gobbi *et al.*, Nucl. Instrum. Methods. **A 324**, 156 (1993).
- [47] W. Reisdorf *et al.*, FOPI Collaboration, Nucl. Phys. **A 612**, 493 (1997).
- [48] P. J. Siemens and J. O. Rasmussen, Phys. Rev. Lett. **42**, 880 (1979).
- [49] G. Poggi *et al.*, Nucl. Phys. **A 586**, 755 (1995).
- [50] M.A. Lisa *et al.*, Phys. Rev. Lett. **75**, 2662 (1995).
- [51] A. Schüttauf, Nucl. Instrum. Methods. **A 533**, 65 (2004).
- [52] P. Fonte, A. Smirnitski, and M.C.S Williams, Nucl. Instrum. Methods. **A 443**, 201 (2000).
- [53] B. Hong *et al.*, J. Korean Phys. Soc. **47**, 782 (2005).
- [54] K. S. Lee *et al.*, J. Korean Phys. Soc. **48**, 846 (2006).



- [55] R. Santonico and R. Cardarelli, Nucl. Instrum. Methods. **A 187**, 377 (1981).
- [56] B. Hong, S. J. Hong, K. S. Lee, S. Park, and K. S. Sim, J. Korean Phys. Soc. **48**, 515 (2006).
- [57] S. H. Ahn *et al.*, Nucl. Instrum. Methods. **A 451**, 582 (2000).
- [58] I. Crotty *et al.*, Nucl. Instrum. Methods. **A 360**, 512 (1995).
- [59] W. Riegler, C. Lippmann, and R. Veenhof, Nucl. Instrum. Methods. **A 500**, 144 (2003).
- [60] C. Lippmann and W. Riegler, Nucl. Instrum. Methods. **A 517**, 54 (2004).
- [61] W. Riegler and C. Lippmann, Nucl. Instrum. Methods. **A 518**, 86 (2004).
- [62] E. C. Zeballos *et al.*, Nucl. Instrum. Methods. **A 373**, 35 (1996).
- [63] E. C. Zeballos *et al.*, Nucl. Instrum. Methods. **A 374**, 132 (1996).
- [64] K. Koch *et al.*, IEEE Trans. Nucl. Sci. **52**, 745 (2005).
- [65] M. S. Ryu, B. Hong, K. S. Lee, S. Park, and K. S. Sim, J. Korean Phys. Soc. **47**, 905 (2005).
- [66] M. Petrovici *et al.*, Nucl. Instrum. Methods. **487**, 337 (2002); *ibid.* **A 508**, 75 (2003).





Acknowledgements

It was a pleasure for me to study and work with the excellent colleagues who encouraged me to keep enjoying this research by the perceptive advice and thoughtful consideration. Here I would like to appreciate their kindness, help, and cooperation and I will always remember the time with them.

First of all, I am deeply grateful to my supervisor, Prof. Dr. Byungsik Hong, for his countless advice, support, and encouragement. His perpetual energy, enthusiasm, and patience for physics have been motivating and encouraging me not only to accomplish my Ph. D. thesis but also to be able to grow up intellectually and mentally.

I esteem Prof. Dr. Kwang Souk Sim for his continuous guidance and encouragement which always make me keep the passion during my graduate course.

I am also appreciative of the committee members of Ph. D. thesis, Prof. Dr. Kyong Sei Lee and Prof. Dr. Eunil Won at Korea University, Seonho Choi at Seoul National University and Prof. Dr. Inkyu Park at University of Seoul.

I would like to express great thanks to Prof. Dr. Sung Keun Park at Korea University and Prof. Dr. Seong Jong Hong at Cachon University of Medicine and Science for their advice and enthusiasm. And I am thankful for all professors' teaching in the physics department of Korea University. Also I really appreciate all professors who had introduced a pleasure and a basic idea about physics at Han Seo University.

I would like to express my gratitude to the Neutron Science Group for allowing me to work at Korea Atomic Energy Research Institute.

This thesis would not have been possible without their interest, advice, and help of the FOPI collaboration. Prof. Dr. Norbert Herrmann at Heidelberg University gave me huge support and acute advice to keep doing my research. Dr. Andreas Schüttauf gave me his interest and heartfelt advice not only my analysis but also life at Germany. Dr. Willibrord Reisdorf and Dr. Yvonne Leifels gave me a lot of constructive comments for my analysis. Dr.



Anton Andronic and Dr. Ralf Averbeck gave me not only help and support but also friendship. Dr. Mladen Kis and Prof. Dr. Xavier Lopez gave me detailed advice and shared not only an office but also friendship. I would be greatly indebted to other members Dr. Mircea Iuliu Ciobanu, Dr. M. Lotfi Benabderrahmane, Ingo Deppner, Pjotr Gasik, Dr. Klaus D. Hildenbrand, Dr. Pjotr Koczon, Dr. Markus Mershmeyer, Dr. Krzysztof Piasecki, Dr. Andreas Reischl, Dr. Ken Suzuki, Prof. Dr. Zhi Gang Xiao, Igor Yushmanov, Dr. Xueing Zhang, Yapeng Zhang, and Dr. Alexander Zhilin, for a lot of advice and support. Also, I appreciate other collaboration members whom I don't mention their names here. In addition, I thank Ms. Sandra Schecker, the secretary of KP I, for remarkable support.

I am obliged to Dr. Seong Yeub Shim who always welcome and encouraged me at GSI.

I thank to all former and present members of Nuclear Physics Group at Korea University. Specially, Dr. Young Jin Kim advised and encouraged me about my analysis. And Drs. Donghee Kang and Donghwa Kang gave me kind advice and welcomed me with warm atmosphere during my graduate study. Also, Dr. Woo Jin Park and MinJung Kweon showed me a lot of passion for physics and gave me nice atmosphere. I am appreciative of other former members, Jintae Yang, Sang Won Seo, Kyungmin Baik, Wooyoung Jang, Junyoung Park, Junyoung Suk, Chan Bo Shim, Eunjin Choi, and Dongho Kang for their advice and care. The present members who have passion and talent in this field, Hyun Ha Shim, Dong Ho Moon, Hyunchul Kim, Byungil Kim, Kwangbok Lee, Ji Hyun Kim, Mikiko Ito, Han-Bum Rhee, Bong Sun Moon, Chong Kim, Mihee Jo, Hoyoung Shon, and Eunah Joo, always refreshed me and showed a lot of interest about my research. I would like to express special thanks to Tae Im Kang for great help and advice.

In the Particle Physics Group at Korea University, I would like to thank Dr. Sung Hwan Ahn gave me encouragement and a lot of detector concept. And I appreciate the other members, Jung Gu Lim, Sung Woong Cho, Hyun Seung Lee, Seung Su Shin, Eunsung Seo, and Min Su Jung.

Also, I want to mention Dr. Dong Hyuk Park who always encourage me and shows sincerity and passion for physics. In addition, I thank many people at Korea University for sharing nice experiences during my graduate course.



Specially, I want to express great thanks to Shin-Woo-meeting, composed of my best friends at I-cheon, for the continuous interest and encouragement for my study and life. Also I thank all my friends, who had studied together at Han Seo University, encourage me during my graduate course.

Especially, I would like to deeply thank the doctors at Asan Medical Center for their cordial treatment and warm reception to my father.

I consecrate this thesis to my grandparents, who are in Heaven. I have been always missing them and thinking of their devotion and love. I deeply thank all my uncles, aunts, and cousins for their encouragement.

Finally, I have been always appreciating of my parents for their eternal love, support, and patience whenever, wherever, and whatever they can do. I would like to give a special and endless appreciation to my brother, sister-in-law, and three nieces who are Shiyeon, Shiwoo, and Shijoon. I hope that this small achievement can make my family happy as long as possible.

